Synthesis, high-pressure study and dielectric characterization of two lead-free perovskite materials : SrTi1-xZrxO3 and KNb1-xTaxO3

Elizabeth Carolina Di Geronimo Camacho

THÈSE

Pour obtenir le grade de

Docteur

Délivré par l'Université de Montpellier

Préparée au sein de l'école doctorale
Sciences Chimiques Balard

Et de l'unité de recherche
Chimie et Crystallograhie des Matériaux (C2M)
Institut Charles Gerhardt – UMR 5253

Spécialité : Chimie des Matériaux

Présentée par Elizabeth Carolina Di Geronimo Camacho

Synthesis, High-pressure Study and Dielectric Characterization of Two Lead-free Perovskite Materials: $SrTi_{1-x}Zr_xO_3$ and $KNb_{1-x}Ta_xO_3$

Soutenue le 15 décembre de 2016 devant le jury composé de

M. Laurent LEBRUN, Professeur, (INSA) Lyon	Rapporteur
M. Pascal MARCHET, Maître de Conférence, Université de Limoges	Rapporteur
M. Paulus WERNER, Professeur, Université de Montpellier	Président du Jury
M. Philippe BARANEK, Ingénieur de Recherche, EDF	Examinateur
M. Philippe PAPET, Professeur, Université de Montpellier	Directeur de thèse
Mme. Véronique BORNAND, Chargé de Recherche, Université de Montpellier	Co-encadrante de thèse

THÈSE

Pour obtenir le grade de

Docteur

Délivré par l'Université de Montpellier

Préparée au sein de l'école doctorale
Sciences Chimiques Balard

Et de l'unité de recherche
Chimie et Crystallograhie des Matériaux (C2M)
Institut Charles Gerhardt – UMR 5253

Spécialité : Chimie des Matériaux

Présentée par Elizabeth Carolina Di Geronimo Camacho

Synthesis, High-pressure Study and Dielectric Characterization of Two Lead-free Perovskite Materials: $SrTi_{1-x}Zr_xO_3$ and $KNb_{1-x}Ta_xO_3$

Soutenue le 15 décembre de 2016 devant le jury composé de

M. Laurent LEBRUN, Professeur, (INSA) Lyon	Rapporteur
M. Pascal MARCHET, Maître de Conférence, Université de Limoges	Rapporteur
M. Paulus WERNER, Professeur, Université de Montpellier	Président du Jury
M. Philippe BARANEK, Ingénieur de Recherche, EDF	Examinateur
M. Philippe PAPET, Professeur, Université de Montpellier	Directeur de thèse
Mme. Véronique BORNAND, Chargé de Recherche, Université de Montpellier	Co-encadrante de thèse

“Other things may change us, but we start and end with family”

Anthony Brandt

ACKNOWLEDGEMENTS

This dissertation was conducted at the Chimie et Cristallochimie des matériaux (C2M) team of the Institut Charles Gerhardt de Montpellier (ICGM).

Like science, life is a long process of learning and discovering, but it is thank to the people that we happen to meet that help us to improve and become a better version of ourselves. I would like to express my appreciation for all individuals that participated in the completion of this dissertation.

I must first thank to my advisor Prof. Philippe Papet for giving me the opportunity of doing my PhD under his guidance. I truly appreciate all the comments, suggestions, support and scientific discussions, which helped me to grow professionally and personally.

I also express my gratitude to Dr. Veronique Bornand for her supervision, and help in the elaboration of this dissertation.

I acknowledge the mentorship from Dr. Julien Haines on the high-pressure experiments. I would like to thank to Dr. Philippe Baranek for the theoretical calculations that helped me answer fundamental question, to Dr. Monica Ceretti for her help and suggestions on how to treat the diffraction data and general kindness, to Dr. Nicole Frety for giving me the opportunity to teach along her side, to Dr. Pascale Armand for always be willing to help since the beginning of my internship, and to Prof. Werner Paulus who gave me the opportunity to be part of the MaMaself master, and it was one of the final steps towards this bigger goal.

I would also express my gratitude to Mr. Laurent Lebrun, professor at INSA-Lyon and Mr. Pascale Marchet, Assistant Professor at the Université de Limoges both rapporteurs of this thesis who agreed to evaluate this work.

I am grateful to the research team and administration staff of the Chimie et Cristallochimie des Matériaux for all the help and kindness during my time there.

I would like to acknowledge the contribution of the staff members of the different laboratories, Léa Daenens, Bernard Fraisse, Dominique Granier, Arie Van Der Lee, Fabrice Barou, Frédéric Fernandez, Samira El Ghazi. Thank you for helping me to perform the different experiments needed for this research, for your kindness and motivation.

I was very lucky to be able to work and meet great people in Bat.15, Avishek, Rocio, Wahid, Padmini, Basma, Fatima, Aliou, Adrien, Renjith, Mai, Serena, Daiane, Mahmoud, Bartosz and Damian. Thank you for making me feel like I have a big international family. Special thanks to the two interns that I had, Anqi Lee and Erwan Carlini whose results help me to complete my work but also for the experience and knowledge that I gained by working with both of them.

Without the encouragement and support of my mother, brother, aunt, friends from back home and the ones that I have made along the road the purposes of this research would not have been realized. Thank you!

RÉSUMÉ

Les matériaux de structure pérovskite de formule générale ABO_3 sont les ferroélectriques les plus étudiés pour leurs propriétés intéressantes dans de nombreuses applications technologiques. Cependant leurs propriétés sont directement reliées à la structure et sont fortement conditionnées par les transitions de phases qui dépendent de la température, de la composition chimique et de la pression. Dans le manuscrit de thèse, le comportement sous haute pression de deux matériaux pérovskite $SrTi_{1-x}Zr_xO_3$ (STZ) et $KNb_{1-X}Ta_XO_3$ (KNT) est étudié et différentes techniques de frittage pour améliorer la densité des céramiques et optimiser les propriétés ferroélectriques des céramiques $K(Nb_{0.40}Ta_{0.60})O_3$ et $(K_xNa_{1-x})Nb_{0.6}Ta_{0.4}O_3$ sont examinées.

Des analyses sous hautes pressions par spectroscopie Raman et diffraction des rayons X des poudres de $SrTi_{1-x}Zr_xO_3$ (x= 0.3, 0.4, 0.5, 0.6, 0.7) et $KNb_{1-X}Ta_XO_3$ (x=0.4, 0.5, 0.6, 0.9) en enclume diamant ont été réalisées. Les spectres Raman montrent une augmentation des modes Raman avec la pression pour les poudres de STZ indiquant que la pression induit des transitions de phases vers des symétries plus basses de la maille dans ces composés.

De plus, les expériences de spectroscopie Raman ont fait apparaître une décroissance des modes Raman lorsque la pression est augmentée, montrant bien que la pression induit des transitions de phases vers des structure plus symétriques. L'évolution du mode Raman principal pour les phases orthorhombique et quadratique a été suivi jusqu'à ce que la phase cubique apparaîsse, ce qui nous a permis de proposer un diagramme de phase pression-composition pour les composés KNT.

Trois différentes techniques de frittage, utilisation d'additifs, frittage en deux paliers et SPS ont été étudiées pour les céramiques de $K(Nb_{0.4}Ta_{0.6})O_3$ et $(K_xNa_{1-x})Nb_{0.6}Ta_{0.4}O_3$. La constante diélectrique et les pertes en fonction de la température des céramiques ont été améliorées par l'utilisation du KF comme additif de frittage et par le frittage en deux paliers. Les échantillons densifiés par SPS présentent une microstructure fine et possèdent les plus fortes densités. Ils ont les meilleurs propriétés ferroélectriques. Aucun changement significatif de la température de Curie ne semble être induit par le taux de Na, et on observe cependant une augmentation de la constante diélectrique et des propriétés ferroélectriques suivant le taux de Na.

ABSTRACT

Perovskite materials whose general chemical formula is ABO_3 are one of the most study ferroelectrics due to the interesting properties that they have for technological applications. However, their properties are directly related to structural phase transitions that could depend on temperature, composition and pressure. In the studies presented here, we first examined the high-pressure behavior of two perovskite materials $SrTi_{1-x}Zr_xO_3$ (STZ) and $KNb_{1-X}Ta_XO_3$ (KNT), and we later continued to investigate different sintering techniques in order to improve the densification, dielectric and ferroelectric properties of $K(Nb_{0.40}Ta_{0.60})O_3$ and $(K_xNa_{1-x})Nb_{0.6}Ta_{0.4}O_3$ ceramics.

High-pressure Raman scattering and X-ray diffraction investigations of $SrTi_{1-x}Zr_xO_3$ (x= 0.3, 0.4, 0.5, 0.6, 0.7) and $KNb_{1-X}Ta_XO_3$ (x=0.4, 0.5, 0.6, 0.9) powders were conducted in diamond anvil cells. Raman scattering experiments showed and increased of Raman modes with pressure for the STZ samples, which indicates that pressure induced phase transitions towards lower symmetry for these compounds.

Moreover, high pressure Raman spectroscopy experiments showed a decrease of the Raman modes as the pressure was increased for the KNT samples, showing that pressure induced phase transitions towards higher symmetries. The evolution of the main Raman modes for the orthorhombic and tetragonal phases were followed until the cubic phase was reach, and allowed us to propose a pressure-composition phase diagram for the KNT compounds.

Three different sintering techniques, sintered aids, two step sintering and spark plasma sintering, were used on $K(Nb_{0.4}Ta_{0.6})O_3$ and $(K_xNa_{1-x})Nb_{0.6}Ta_{0.4}O_3$ ceramics. The use of KF as sintered aid and the two step sintering method showed an improvement of the dielectric constant and dielectric losses of these samples. SPS samples presented a fine microstructure with the highest density and the best ferroelectric behavior. We did not detect any changes on the Curie temperature due the amount of Na but and increase of the dielectric constant and the ferroelectric properties was observed due to the amount of Na.

CONTENTS

LIST OF FIGURES

LIST OF TABLES

INTRODUCTION

Energy issues have grown considerably in our consumerism society and two major problems will need to be addressed for the upcoming: finding alternative energy resources for the future world standard of living, and considering the environmental impact of energy production and consumption. Furthermore, energy storage and/or power supply have also faced many problems for its production, and the current pathway of research efforts is dedicated to electric storage for mobile applications, electrochemical batteries, fuel cell, and the production of capacitors and/or supercapacitors for electrostatic and hybrid or electrochemical applications.

A capacitor is a component use to store energy in the form of electric charges. It is composed of at least two electrical conductors materials, electrodes, which are separated by a thin layer of a dielectric material, usually made of ceramic, glass or a plastic film. The energy is stored in dielectrics as a result of static charge accumulation on the electrodes when an electric potential difference is applied. The properties of the capacitor should essentially depend on the dielectric material, and more precisely on its relative permittivity. The magnitude of the stored energy density is related to the relative permittivity of the dielectric material and to the geometric parameters of the capacitor, thickness of the dielectric between the electrodes, and the surface in contact with the electrodes. The discharge power on this type of system is higher than the conventional electrical power generation; the charging time is significantly faster and less damaging than in the case of electrochemical systems, and they are appropriate for storing small quantities of electrical energy. However, this electrostatic storage system have limited capacity, relatively low energy density, and therefore, it is still considered as a complement technology to other systems.

There are three types of ceramic capacitors and only types II and III are considered for electric energy storage. Type II ceramic capacitors uses dielectric materials that are ferroelectrics and exhibit a high relative permittivity (up to 15000); however, they present a significant dependence on temperature, electric field or frequency. The relative permittivity of this class of materials can be improved by shifting the Curie temperature near the ambient one; this can be achieved by partial element substitution, and also by developing specific ceramic microstructures. On the other hand,

type III capacitors are essentially composed of type II grains, which are designed to be semiconductive, embedded by insulated layers located at the grain boundaries. The surface and thickness of the grain boundaries become the capacitor and they have a very large permittivity (up to 100,000) but a relatively low voltage application (around 25 V), therefore they can be used only for specific functions.

Ferroelectrics are part of a type of materials that exhibit spontaneous electric polarization that can be switched by applying external electric fields. The strong polarization is directly related to structural phase transitions as function of temperature, composition or pressure. Structurally speaking, there are four types of ferroelectric ceramics: (1) perovskites, (2) the tungsten-bronze group, (3) pyrochlores and (4) the bismuth layer-structure group. The perovskite materials (ABO_3) are by far the most studied materials of the ferroelectrics due to the interesting properties that allow them to be used on a variety of different technological applications. Among all ferroelectric materials, the perovskite ceramics containing lead are widely used. However, there has been an increase of environmental and health awareness that have triggered the development of more environmental friendly materials that could replace the currently lead-based ceramics. Therefore, the research into novel lead-free materials has expanded over the past 20 years and materials like $K(Nb,Ta)O_3$, $(K,Na)NbO_3$, $BaTiO_3$, $(Bi,Na)TiO_3$-based ferroelectric have been developed. Many compositions within these solid solutions exhibit good ferroelectric properties, some of them showed for instance relatively large piezoelectric properties; however, various drawbacks of these systems are related to the difficulty in processing and densification of the samples, and also because none of them can fully replace the lead-based materials in all the current applications in which they are used.

At the same time, an essential part on today's research is to understand how the properties of lead-free ferroelectrics change at the nano-scale from the bulk one. Indeed, these materials could sustain a high level of constrains when they are inserted in miniaturized technological components, more specifically in the form of thin films or nanomaterials, and high-pressure (HP) experiments can help in understanding the behavior of these materials. However, studies on HP-induced transformations of these lead-free perovskites are surprisingly sparse.

This investigation addresses some of the above-mentioned issues. The first part of this work is dedicated to the synthesis and study under pressure of two lead-free perovskite materials, strontium titanium zirconate (STZ) and potassium niobium titanate (KNT) solid solutions. Indeed, theoretical calculations by DFT have shown that these solid solutions exhibit a series of phase transitions at relatively low pressure. Moreover, the second part deals with the use of different sintering techniques to improve the densification of $KN_{0.4}T_{0.6}O_3$ ceramics and to study their dielectric and ferroelectric properties. In addition, it is investigated the influence of Na-doping in the A-site of the perovskite structure on the morphological and physical characteristics of $KN_{0.6}T_{0.4}O_3$ ceramics.

A brief overview of the individual chapters of this dissertation is given:

- **Chapter one** gives an introduction to ferroelectric materials as well as some general basis for understanding the physical phenomena that are described in this work.
- **Chapter two** provides a general overview of the state of the art of the two-perovskite materials that are used during investigation, strontium titanium zirconate and potassium niobium tantalate.
- **Chapter three** describes the synthesis process that was used to obtain well crystalline compounds, as well as the different sintering methods used to densify the ceramic pellets. Finally, it explains the several experimental techniques used to characterize the polycrystalline powder and the ceramics.
- **Chapter four** outlines and discusses the experimental results obtained in function of the hydrostatic pressure and composition for strontium titanium zirconate and potassium niobium tantalate polycrystalline samples. It shows the different phase transitions induce by pressures, which were studied by high pressure Raman spectroscopy and X-ray diffraction.
- **Chapter five** discusses the influence of three different sintering techniques on the morphology, density and dielectric properties of $KNb_{0.4}Ta_{0.6}O_3$ and $(K_xNa_{1-x})Nb_{0.6}Ta_{0.4}O_3$ (x=1.0, 0.9, 0.8, 0.7, 0.6, 0.5) ceramics.
- Some general concluding words are given at the end of this dissertation.

CHAPTER I
INTRODUCTION TO FERROELECTRICITY

1.1. – Basics of Ferroelectrics

The aim of this chapter is to give brief background information of the basics of ferroelectric materials. Most of the information giving here comes from books by L. Pardo and J. Ricote [1], B. Jaffe, W. R. Cook, and H. Jaffe [2] and A. J. Moulson and J. M. Herbert [3], which can be consulted for a better inside of the described information.

1.1.1. - Dielectric behavior

Any material that is electrically insulating, supports charge without conducting it to an important level, is called dielectric. This type of material presents electric dipoles, which are two opposite charges separated by a certain distance, on a molecular or atomic level. On every electric dipole there is a separation between a positive and a negative electric charge that gives rise to a dipole moment. Once an electric field is applied, a force will be exerted on an electric dipole that will try to align it with the applied field. This process of dipole orientation is called polarization and can occur by several mechanism of limited charge rearrangement. Electronic polarization is caused by a displacement of the electron cloud in one direction and the nucleus moves on the other direction originating a dipole moment since the center of the electron cloud does not longer coincide with the nucleus. Another mechanism is ionic polarization, where there is going to be an off centering of the cations with respect to the anions and vice versa in the presence of an electric field. Finally, they could be a dipole and space charge polarizations when an electric field is applied, that will cause a rotation of the permanent dipoles in the direction of the applied field and charges will accumulate at interfaces in the material.

1.1.2. - Capacitor

A capacitor is a device composed of two conducting plates that are separated by a non-conductive material, or dielectric, and it is used to store energy. When a voltage is applied through a capacitor, the plates will have opposite charges, and an electric field

will be present between them. Each capacitor has a capacitance, C, which is related to the quantity of charge stored on both plate, and it is defined by the following expression:

$$C = \frac{Q}{V} \qquad \text{eq. 1.1}$$

Where Q is the charge on each plate and V is the voltage applied across the capacitor. The capacitance is affected by different factors, like the geometry of the capacitor and the dielectric material that is placed between the plates. The capacitance of a parallel plate capacitor with a vacuum between the electrodes, Fig 1.1 (a), can be calculated by:

$$C = \epsilon_0 \frac{A}{l} \qquad \text{eq. 1.2}$$

Where A is the area of the plates, l the distance between them, and ϵ_0 is the permittivity of a vacuum, which is a universal constant and has a value of 8.8510^{-12} F/m. However, if a dielectric material is inserted within the plates Fig 1.1 (b), now the capacitance will depend on the permittivity of the material, ϵ, and it will be computed by the following expression:

$$C = \epsilon \frac{A}{l} \qquad \text{eq. 2.3}$$

The following figure shows a parallel-plate capacitor when a vacuum or a dielectric material is between the plates.

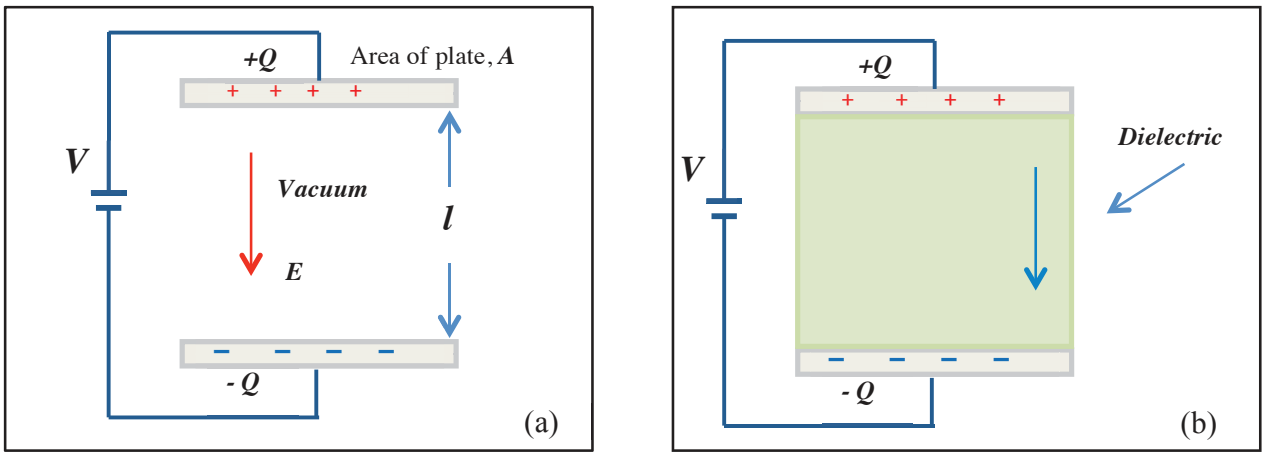

Figure 1.1. (a) Parallel-plate capacitor with a vacuum between plates. (b) Capacitor with a dielectric material, there is a polarization due to the applied electric field.

1.1.3. - Dielectric constant

The dielectric constant of a material is the ratio of the capacitance of a capacitor containing a dielectric material to an identical one but in vacuum. Another definition can be one related to the permittivity, since the effect of a material under the influence of an electric field is described by the permittivity of it, and it can be defined as the ability of a material to be polarized in response to an applied field.

The dielectric constant also called the relative permittivity is equal to the ratio of the permittivity of the dielectric material to the permittivity of a vacuum (ec 1.4) and it represents the increase of capacity in charge storing, so the more a material is polarized by an applied field then the greater the dielectric constant will be.

$$\epsilon_r = \frac{\epsilon}{\epsilon_0} \qquad \text{eq. 1.4}$$

Where ϵ_r is the relative permittivity, ϵ is the permittivity of the dielectric medium, and ϵ_0 is the permittivity of a vacuum.

1.1.4. – Stored electric charge

The total charge per unit area of a capacitor plate, D_0, is proportional to the applied electric field, E, being the constant of proportionally ϵ_0.

$$D_0 = \frac{Q}{A} = \epsilon_0 E \qquad \text{eq. 1.5}$$

If a dielectric material is now placed between two parallel plates, the following expression is obtained:

$$D = \epsilon E \qquad \text{eq. 1.6}$$

The dielectric displacement or surface charge density, D, represents the total charge that is stored due to the presence of a dielectric material. In addition, the dielectric displacement of a capacitor in the presence of a dielectric can be represented as well by the following expression:

$$\boldsymbol{D = \epsilon_0 E + P} \qquad \text{eq. 1.7}$$

Where $\boldsymbol{P}$ is the polarization and is the total dipole moment per unit volume of the dielectric material. The polarization is proportional to the applied electric field by:

$$\boldsymbol{P = \epsilon_0(\epsilon_r - 1)E = \epsilon_0 \chi E} \qquad \text{eq. 1.8}$$

In where $\boldsymbol{\chi}$ is the electric susceptibility and is a dimensionless constant that shows the degree of polarization of a dielectric material when an electric field is applied to it. It is always frequency-dependent and only constant at a given frequency for linear dielectrics. It can be written as:

$$\boldsymbol{\chi = \epsilon_r - 1} \qquad \text{eq. 1.9}$$

Now, by substituting eq. 1.8 into 1.7 it is obtained:

$$\boldsymbol{D = \epsilon_0(1 + \chi)E} \qquad \text{eq. 1.10}$$

For dielectrics that polarize easily, the susceptibility will increase, and as result a large quantity of charge can be stored.

As it was described before, the capacitance increases when a dielectric material is inserted between the electrodes. Due to influence of an external electric field, the dielectric material will be polarized and charge redistribution on the surfaces that are in contact with the capacitor plates will occur. The surface, which is nearest to the positive capacitor plate, is negatively charge and vice versa. As a result, electric field lines within the dielectric material are created. This will cause a partial neutralization of the electric field between the plates and will lead to a reduction on the field strength; this can be seen by a fall in the voltage. Since the voltage in the capacitor has been reduce without any changes to the charge on the plates, it is possible to observe that by inserting a dielectric within the two capacitor plates there will be an increase in charge density, and this is illustrated in figure 1.2.

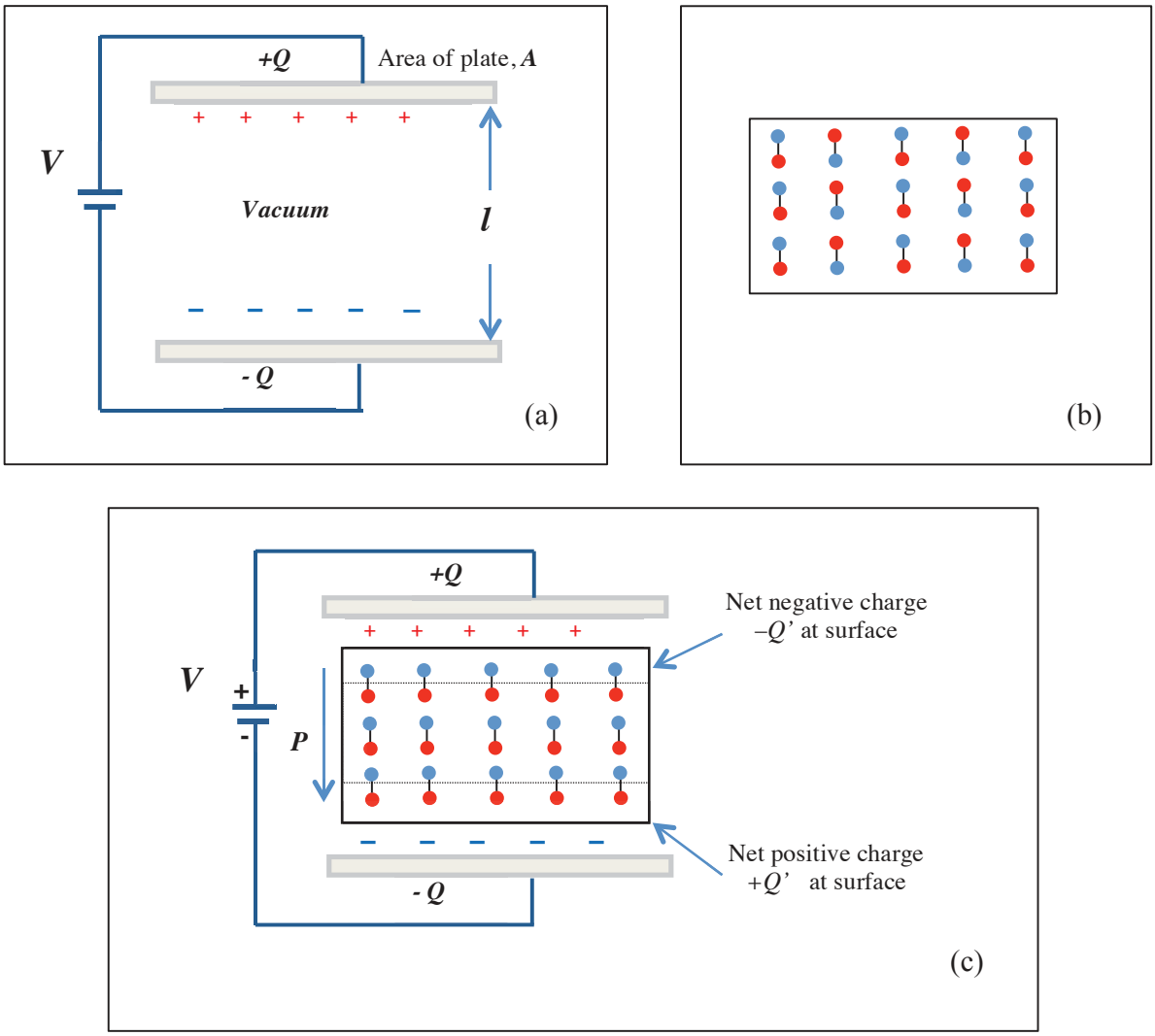

Figure 1.2. Schematic representation of (a) charge stored on a capacitor plates for a vacuum, (b) dipole arrangement in an unpolarized dielectric, in where the positive charges are denoted in red and negative in blue, (c) the increased charge storing capacity resulting from the polarization of a dielectric material.

1.1.5. - Frequency dependence of the dielectric constant

As it was mentioned before, a dielectric material becomes polarized in an electric field; however, when the applied voltage is alternating, the electric field changes its direction with time and the direction of the polarization will also reorient in order to be aligned with the new direction of applied electric field. Nevertheless, this process cannot happen spontaneously, some time is required for the rotation of the dipoles, and this time

that the average dipole orientation takes to adjust is called relaxation time. On the other hand, if the electric field alternates at very high frequencies there is going to be a point in where the dipoles cannot keep shifting of orientation, and it is unable to stay aligned with the electric field. As a result, the polarization mechanism ceases to contribute to the polarization of the dielectric, and this can be seen as a drop in the value of the dielectric constant.

1.1.6. –Dielectric losses

A dielectric material that is efficient can support the shifting of dipole moments with the minimal dissipation of energy in the form of heat .The origin of this heat is due to the ability of the electric field to polarize the charges in the material and the inability of this polarization to follow in a fast way reversals of the electric field, resulting in the dissipation of power within the dielectric material. In addition a dielectric can be heated through direct conduction effects due to charge particles redistribution under the influence of external applied electric field, which will form conducting path, particularly in mixture of heterogeneous materials [4].

A special case can be the interfacial or Maxwell-Wagner polarization, which is very important to take into account in heterogeneous dielectric materials. This is related to the build-up of charge particles at the interfaces and influences the total polarization for frequencies less than $5x10^7$ Hz. The dielectric behavior related with non-uniform distribution of free electronic charges across the interface between heterogeneous dielectric materials could be understood by considering the system under dc equilibrium conditions. In this case there must be an electrical current continuity across the boundary between the materials. Each material has its own free charge carriers concentration and associated charge carriers mobility, and in order to have current continuity across the materials there will be a charge carrier concentration discontinuity across the interface. This interfacial charge build up or polarization, as function of the frequency is what it gives rise to the dielectric dispersion exhibited by heterogeneous systems, due to change in conductivity that occurs at the boundaries, imperfections such as cracks and porosity [4,5].

1.2. – Ferroelectricity

1.2.1. - Symmetry of materials

According to crystal symmetry, crystals can be divided into 32 point groups (crystal classes). Eleven of these classes have center of symmetry and as a consequence they do not possess any polar properties even when an electric field is applied. Among the other 21 non-centrosymmetric groups, 20 groups can exhibit polarity when a stress is applied. These 20 groups are piezoelectric and between these 20 groups, 10 point groups (1, 2, m, mm2, 4, 4mm, 3, 3m, 6, and 6mm) have a unique polar axis and they display spontaneous polarization [6]. These are the pyroelectric (polar) classes and in some of them the spontaneous polarization can be switched when an electric field is applied, and therefore they will have ferroelectric properties.

1.2.2. - Structural transitions

A common definition of ferroelectrics material is a non-centrosymmetric polar crystal that possesses two or more orientations of the spontaneous polarization vector in the absence of an external electric field, and in which the spontaneous polarization vector can be shifted between orientations by an electric field. These orientation states are identical in crystal structure and differ only in electric polarization vector at zero electric field. The magnitude of the net spontaneous polarization possessed by a ferroelectric material starts to decrease by increasing temperature or pressure. Above a critical temperature T_C (and a critical pressure P_C), called the Curie temperature, the spontaneous polarization disappears when a phase transition from polar ferroelectric state to non-polar paraelectric state takes place. This transition can be defined from a structural point of view as a phase transition from a non-centrosymmetric to a centrosymmetric structure [7]. For most ferroelectrics, the paraelectric state is the highest symmetry phase compatible with the ferroelectric structure or the simply prototype phase. The structural phase transition from paraelectric to ferroelectric phase is due to the displacement of both cations occupying the A and B sites in the perovskite. This transition usually leads to strong anomalies in the dielectric, elastic, thermal and other properties of the material [7] and is complemented with changes in the dimensions of the crystal unit cell.

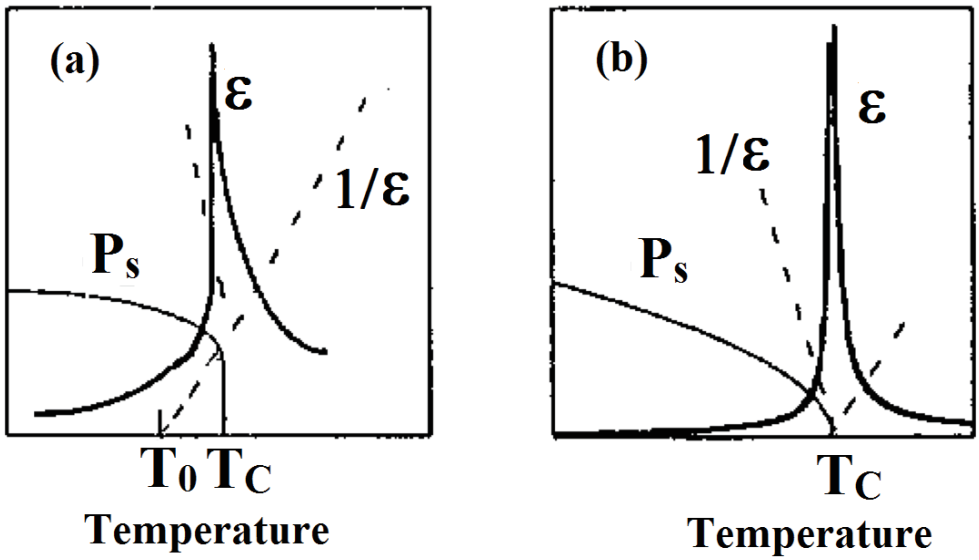

Figure 1.3. Temperature dependence of the dielectric permittivity (ε) and spontaneous polarization (P_S) for (a) first-order and (b) second-order ferroelectric phase transition [8].

Ferroelectric transitions are classified into first-order (displacive type) and second-order (order-disorder type) phase transitions. The spontaneous polarization (see figure 1.3(a)) and crystal structure of first-order ferroelectric are characterized by discontinuous changes at the phase transition temperature where a metastable phase appears while the second-order phase transition is characterized by continuous changes in the spontaneous polarization (see figure 1.3(b)) and crystal structure at the phase transition temperature [8].

For ferroelectrics ceramic, the change in the lattice structure will be associated with a sharp peak in the dielectric constant at T_C. In the paraelectric phase above T_C, the dielectric permittivity (ε) decreases with temperature according to the Curie law:

$$\varepsilon = \frac{C}{T - T_0} \qquad \text{eq. 1.11}$$

In this formula C is the Curie constant and T_0 is the Curie temperature, and for a second order phase transition $T_0 = T_C$ while for first order phase transition $T_0 < T_C$ (figure 1.3).

1.2.3. - Hysteretic behavior

When a ferroelectric material is exposed to a strong electric field, **E**, it shows a hysteretic loop behavior. The effect of polarization switching by an external electric field can be seen in the Figure 1.4, which illustrates the polarization electric field hysteresis loop of a typical poly-domain ferroelectric material.

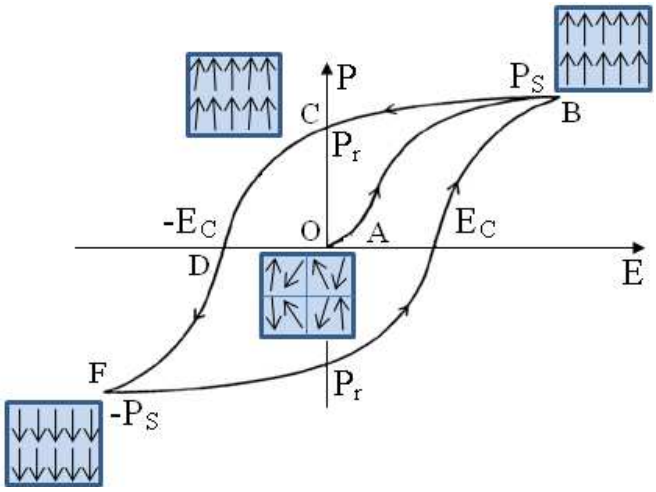

Figure 1.4. Representation of a hysterics loop for a ferroelectric. The polarization goes from 0 till P_S, once the electric field is removed it goes to P_r, and then when E_c is applied it goes back to zero. The arrows in the squares indicate the direction of polarization of the material.

The net polarization of an unpolarized ferroelectric is almost zero. When an AC electric field is applied, the polarization starts to increase linearly with the applied field according to equation 1.8 ($P = \varepsilon_0 \chi E$) where χ is the dielectric susceptibility of the material. The segment OA in figure 1.4 shows a linear region where no polarization switching of unfavorable domains takes place due to small amplitude of the applied field. By increasing the applied field, it will start the polarization switching of the unfavorable domains (domains with the direction of the spontaneous polarization opposite to the applied field) till all the domains are aligned with the field. The relation of the polarization and the electric field is nonlinear in this region (segment AB in Figure 1.4). At this point, if the field is still increased, the polarization will have again a linear behavior. When the electric field returns to zero, some domains will switch back but the

polarization will not go to zero (point C). The amount of the switchable polarization at zero electric field is called the remnant polarization, $\boldsymbol{P_r}$. To cancel the remnant polarization, the applied field should be reversed (point D). The strength of the electric field that brings the polarization back to zero is known as coercive field, $\boldsymbol{E_C}$. If the electric field is still increased in the reversed direction, opposite alignment of the domains will take place (point F). To complete the cycle, the field will be reduced back to zero and then reversed again. The value of the maximum remnant polarization $\boldsymbol{(P_R)_{max}}$ depends on the number of domain states, for a ferroelectric with 180° domain walls only, the maximum remnant polarization $\boldsymbol{(P_R)_{max}}$ is just 0.25 P_S, a tetragonal phase with six six poling directions, $\boldsymbol{(P_R)_{max}}$ = 0.83 P_S, a rhombohedral phase with eight ones, $\boldsymbol{(P_R)_{max}}$ = 0.87 $\boldsymbol{P_S}$, and finally for a orthorhombic phase with twelve poling directions, $(P_R)_{max}$ = 0.91 P_S [9, 10]. These are the values corresponding to the reorientation of all the available domains.

1.3. – Perovskite structure

There are many types of crystals that show the ferroelectric properties but the most known ferroelectric structure since more than 60 years is the perovskite structure [11-14]. In addition to ferroelectricity, a lot of important physical properties can be seen among perovskites such as ferroelasticity [15], superconductivity [16-18], magnetoresistance [19], dielectric properties [20], ferro/antiferro-magnetism [21], and multiferroic properties [22, 23].

The general chemical formula for a perovskite structure is ABO_3 in where A and B are the cations. Its ideal (aristotype) structure is cubic, with space group symmetry $Pm\bar{3}m$, and it is considered as probably the simplest example of a structure containing two different cations [24]. The ideal cubic perovskite structure is shown in Figure 1.5 where the A (monovalent or divalent metal) atoms are at the corners of the cube, the B (tetravalent or pentavalent metal) atoms are at the center of the cube and the oxygen at the face centers. The traditional view of the perovskite lattice consists of small B cations within oxygen octahedra, and larger A cations which are 12 fold coordinated by oxygen.

In many perovskite materials, the A site and/or the B site are occupied by more than one cation. This leads to another type of structure known as complex or double

perovskite structure in addition to the simple structure. Complex perovskite structures have a general formula of AA'BB'O_3 and show many new physical properties that do not appear in simple perovskites, mainly the relaxor effect in ferroelectrics [25].

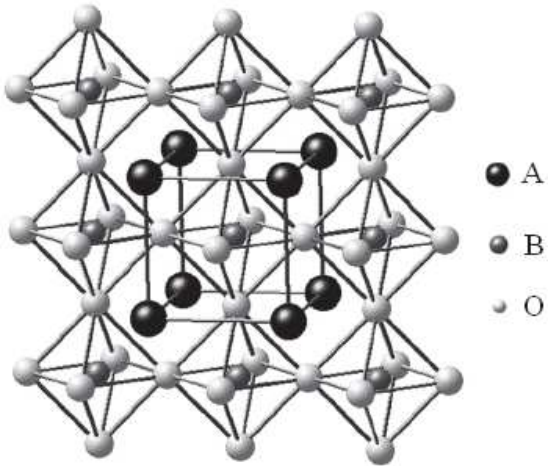

Figure 1.5. Simple cubic perovskite unit cell of type ABO_3.

1.3.1- Distortions in perovskites

Due to the relative sizes of the A and B cations, different types of distortions occur in the simple cubic perovskite structure, like leading to a symmetry reduction for most of the perovskites. The three distortions identified by Megaw [24] are:

i- Distortions of the octahedral units (Jahn-Teller distortion).

ii- B-cation displacements within the octahedral, leading to either a ferroelectric (if all the B atoms move in the same direction) or antiferroelectric (if the B atoms move in opposite directions) structure.

iii-The relative tilting of one octahedral to another. This is the most common distortion that takes place in perovskites (Figure 1.6). The tilting takes place if the A atom is too small for the large 12-fold site, thus adjacent octahedral tilt in opposite senses about one or more of their symmetry axes, maintaining both regularity of the octahedral (approximately) and their corner connectivity (strictly) [26]. Such tilting increases the size of the unit cell and reduces the size of the A-site while leaving the environment of the B-cation essentially unchanged [26].

Each of these distortions can occur separately or in combination, leading to a great variety of different structural modifications depending on the sizes, the bonding character and the ordering of these different cations occupying the A or B sites.

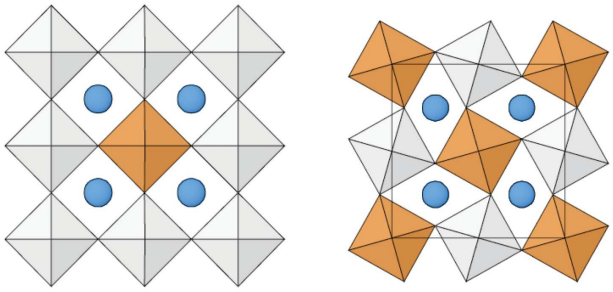

Figure 1.6. (a) The cubic perovskite in its high symmetry form with no octahedral tilting. (b) Perovskite structure in its low symmetry form with octahedral tilting. The spheres represent the A cations [27].

1.3.2. - Stability of perovskite structure

The octahedral tilting distortion was first examined by Goldschmidt in 1926 [28] who, in order to determine the stability of perovskite phases, defined the tolerance factor *t* as follows:

$$\boldsymbol{t} = \frac{\mathbf{R_A + R_X}}{\sqrt{\mathbf{2}}(\mathbf{R_B + R_X})} \qquad \text{eq. 1.12}$$

In this formula R_A, R_B and R_X are the ionic radii of the A-site and B-site cations and the X-site anion respectively in an ABX_3 perovskite. In the case of complex perovskite, the average ionic radius of the ions occupying each site is considered. The deviation of $\boldsymbol{t}$ from the unity measures the degree of distortion of a perovskite from the ideal cubic structure. The ideal cubic perovskite for $SrTiO_3$ has $\boldsymbol{t}$ = 1.00, R_A = 1.44 Å, R_B = 0.605 Å, and R_O = 1.40 Å. The relation between the value of the tolerance factor $\boldsymbol{t}$ and the symmetry has been determined through experiments. Hexagonal symmetry will be exhibited with $1.00 < \boldsymbol{t} < 1.13$. Cubic structure occurs if $0.89 < \boldsymbol{t} < 1$ [29, 30] and orthorhombic if $0.75 < \boldsymbol{t} < 0.89$. The tilting also depends on the tolerance factor, Reaney

et al. [31] showed that at room temperature perovskites with $0.985 < \boldsymbol{t} < 1.06$ do not present tilted structures. In addition, perovskites with $0.964 < \boldsymbol{t} < 0.985$ are usually tilted in antiphase and perovskites with $\boldsymbol{t} < 0.964$ are expected to show in phase and antiphase tilting.

1.3.3. - The prototype phase $BaTiO_3$

Barium Titanate ($BaTiO_3$) is the model of ferroelectric materials. Figure 1.7 shows various crystalline phases of $BaTiO_3$ at different temperatures. At high temperature, it is paraelectric (no net spontaneous polarization) with a cubic phase, however, as the temperature decreases different phase transitions will occur. A tetragonal and [100] polarized below its Curie temperature (T_C = 120°C), orthorhombic and [110] polarized below 5°C, and rhombohedral and [111] polarized below -90°C. Figure 1.7 shows only the cubic and tetragonal crystal structures of $BaTiO_3$. As shown in the figure, when $BaTiO_3$ is cooled down through the Curie temperature, both the Ba and Ti atoms shift upward from their lattices relatively to the negatively charged oxygen, generating a spontaneous polarization (net dipole moment per unit volume). This shift breaks the cubic symmetry into a tetragonal phase and results six symmetry-related and crystallographic equivalent polar axes.

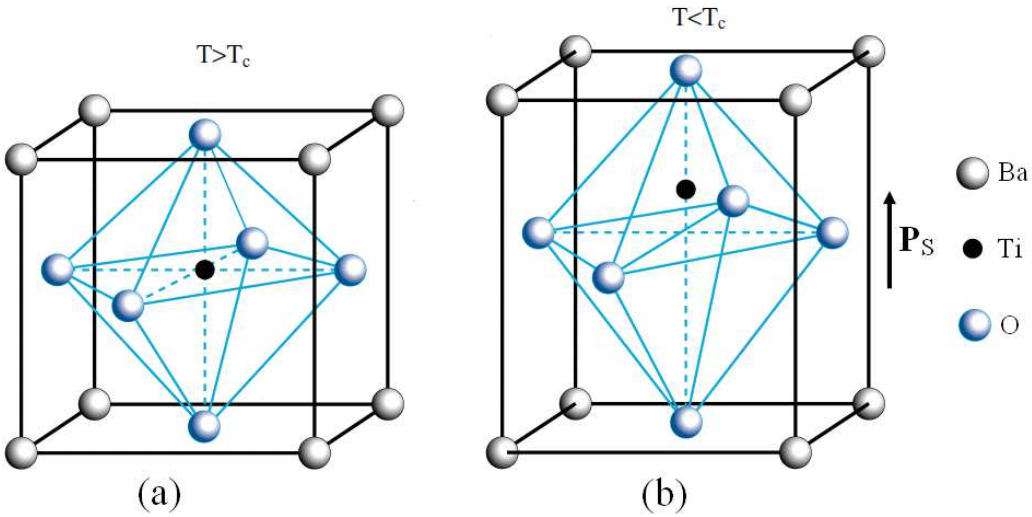

Figure 1.7. Schematic diagram for (a) the cubic phase of $BaTiO_3$ above T_C and (b) the tetragonal phase of $BaTiO_3$ below T_C. The arrow represents the induced spontaneous polarization as the titanium ion shifts from its central position.

Bibliography

[1] L. Pardo, J. Ricote, Multifunctional Polycrystalline Ferroelectric Ceramics, Spring, 2011.

[2] B. Jaffe, W. R. Cook, H. Jaffe, Piezoelectric Ceramics, Academic Press, London, 1971.

[3] A. J. Moulson, J. M. Herbert, Electroceramics, second ed., Wiley & Sons Ltd., Chichester, 2003.

[4] A.C Metaxas, R.J. Meredith, Industrial Microwave Heating, Peter Peregrinus Ltd., London, 1993.

[5] M. Iwamoto, Maxwell–Wagner Effect, in: B. Bharat (Ed.), Encyclopedia of Nanotechnology, Springer, Netherlands, 2012, 1276-1285.

[6] Y. Xu, Ferroelectric Materials and Their Applications, North-Holland, Amsterdam, 1991.

[7] M. E. Lines, A. M. Glass, Principles and Applications of Ferroelectrics and Related Materials, Clarendon, Oxford, 1977.

[8] D. Damjanovic, Ferroelectric, dielectric and piezoelectric properties of ferroelectric thin films and ceramics, Rep. Prog. Phys. 61 (1998) 1267-1324.

[9] L. E. Cross, Ferroelectric ceramics: tailoring properties for specific applications, in: N. Setter, E.L Colla (Eds.) Ferroelectric Ceramics, Birkhäuser, Basel, 1993, 1-8.

[10] R. W. Whatmore, Pyroelectric devices and material, Rep. Prog. Phys. 49 (1986) 1335-1386.

[11] H. Thurnaurer, J. Deaderick, Insulating Material, U. S. Patent No. 2,429,588, Oct. 21, 1947, filed (1941).

[12] B. Wul, J. M. Goldman, C. R. Acad. Sci URSS. 46 (1945) 139.

[13] H. D. Megaw, Crystal Structure of Barium Titanate, Nature, 155 (1945) 484.

[14] S. Miyake, R. Ueda, On polymorphic change of $BaTiO_3$, J. Phys. Soc. Jap. 1 (1946) 32-33.

[15] N. Orlovskaya, N. Browning, A. Nicholls, Ferroelasticity in mixed conducting $LaCoO_3$ based perovskites: a ferroelastic phase transition Acta Mater. 51 (2003) 5063-5071.

[16] R. J. Cava, A. Santoro, D. W. Johnson, W.W. Rhodes, Crystal structure of the high-

temperature superconductor $La_{1.85}Sr_{0.15}CuO_4$ above and below *Tc*, Phys. Rev. B 35 (1987) 6716.

[17] J. M. Tarascon, L. H. Greene, W. R. Mckinnon, G. W. Hull, T. H. Geballe, Superconductivity at 40 K in the oxygen-defect perovskites La2-xSrxCuO4-y, Science, 235 (1987) 1373.

[18] C. W. Chu, P. H. Hor, R. L. Meng, L. Gao, Z. J. Huang, Superconductivity at 52.5 K in the lanthanum-barium-copper-oxide system, Science, 235 (1987) 567.

[19] R. V. Helmolt, J. Wecker, B. Holzapfel, L. Schultz, K. Samwer, Giant negative magnetoresistance in perovskitelike $La_{2/3}Ba_{1/3}MnO_x$ ferromagnetic films, Phys. Rev. Lett. 71 (1993) 2331.

[20] J. Barrett, Dielectric constant in Perovskite Type Crystals, Phys. Rev. 86 (1952) 118.

[21] E. O. Wollan, W. C. Koehler, Neutron Diffraction Study of the Magnetic Properties of the Series of Perovskite-Type Compounds $[(1-x)La, xCa]MnO_3$, Phys. Rev. 100 (1955) 545.

[22] N. Hur, S. Park, P. A. Sharma, J. S. Ahn, S. Guha, S-W. Cheong, Electric polarization reversal and memory in a multiferroic material induced by magnetic fields, Nature, 429, (2004) 392-395.

[23] N. Ikeda, H. Ohsumi, K. Ohwada, K. Ishii, T. Inami, K. Kakurai, Y. Murakami, K. Yoshii, S. Mori, Y. Horibe, and H. Kitô, Ferroelectricity from iron valence ordering in the charge-frustrated system $LuFe2O_4$, Nature, 436 (2005) 1136-1138.

[24] H. D. Megaw, Crystal Structures, W. B. Saunders, London, (1973) 216-282.

[25] G. A. Samara, The relaxational properties of compositionally disordered ABO_3 perovskites J.Phys.:Condens.Matter 15 (2003) R367-R411.

[26] C. J. Howard, H. T. Stokes, Group-Theoretical Analysis of Octahedral Tilting in Perovskites, Acta Cryst. B54, 782-789 (1998).

[27] G. Fraysse, Doctoral thesis: ”Influence de la température et de la pression hydrostatique sur l’instabilité ferroélectrique et l’instabilité rotationnelle de la structure pérovskite dans les solutions solides Pb(Zr1−xTix)O3”, Université de Montpellier II, 2009.

[28] V. M. Goldschmidt, Geochemische Verteilungsgesetze der Elemente, Skrifter Norske Videnskaps-Akad, Oslo, I. Mat. Nat. Kl. (1926) 8

[29] A. F. Wells, Structural Inorganic Chemistry, Oxford Science publications, 1995.
[30] U. Müller, Inorganic Structural Chemistry, Wiley and Sons Ltd, 1993.
[31] I. M. Reaney, E. L. Colla, N. Setter, Dielectric and structural characteristics of Ba- and Sr-based complex perovskites as a function of tolerance factor, Jpn. J. Appl. Phys. 33 (1994) 3984.

CHAPTER II
STATE OF THE ART IN STRONTIUM TITANIUM ZIRCONATE AND POTASSIUM NIOBIUM TANTALATE MATERIALS

In the last recent years, it has been witnessed significant progress in materials that could substitute the ones that contain lead [1,2]. In this state of the art we aim to give an overview of two groups of lead-free perovskite materials, being the first group the strontium titanium zirconate family and the second one the alkali potassium niobium tantalate.

2.1. – Structure and phase transitions of strontium titanate and strontium zirconate

At room temperature strontium titanate ($SrTiO_3$) has an ideal perovskite structure (*Pm-3m*) and its dielectric constant is around 250 at room temperature and increases as the temperature is reduce. Moreover, $SrTiO_3$ undergoes a phase transition at about 110 K into a tetragonal structure that does not loss its center of symmetry (*I4/mcm*), and non-ferroelectric properties are observed [3]. On the other hand, strontium zirconate ($SrZrO_3$) exhibits an orthorhombic structure (*Pnma*) at room temperature and undergoes the following phase transitions: orthorhombic (*Pnma)* ↔ orthorhombic (*Imma*) ↔ tetragonal (*I4/mcm*) ↔ cubic (*Pm-3m*) at 1023 K, 1113 K and 1343 K, respectively [4]. Neither $SrTiO_3$ nor $SrZrO_3$ is ferroelectric but ferroelectricity has been observed in artificial $SrZrO_3$ and $SrTiO_3$ superlattice elaborated by molecular beam epitaxy [5]. Furthermore, it was shown by first principal calculation that ferroelectricity can be induced in the perovskite oxide ($SrZrO_3$- $SrTiO_3$) superlattice due to a large atom relative displacement between the Zr and O atoms and that the largest contribution to the polarization likely comes from $SrZrO_3$ [6].

2.1.1. - $SrTiO_3$-$SrZO_3$ solid solution

Perovskite materials can present composition dependent transitions at constant temperature and/or pressure. These transitions can take place when there is a substitution of a different cation on the A and/or B-site. It has been reported that $SrTi_xZ_{1-x}O_3$ solid solutions have a sequence of structural transitions at room temperature depending on the substitution of Ti by Zr. There have been performed two studies on the different phase

transitions observed for $Sr(Zr,Ti)O_3$ [7, 8]. However, there is a discrepancy between them.

Wong et al. reported the structural characterization by X-ray and neutron powder diffraction methods for $SrTi_xZr_{1-x}O_3$. They found three phase transitions at room temperature depending on the composition, and no other second orthorhombic phase or ordering of the Zr and Ti cations was reported. In addition, phase transition from tetragonal to cubic structures involves tilts of the BO_6 octahedral and this angle tilting decreases as the amount of Ti increases [7]. The following figure shows the phase diagram stated by Wong et al as function of composition.

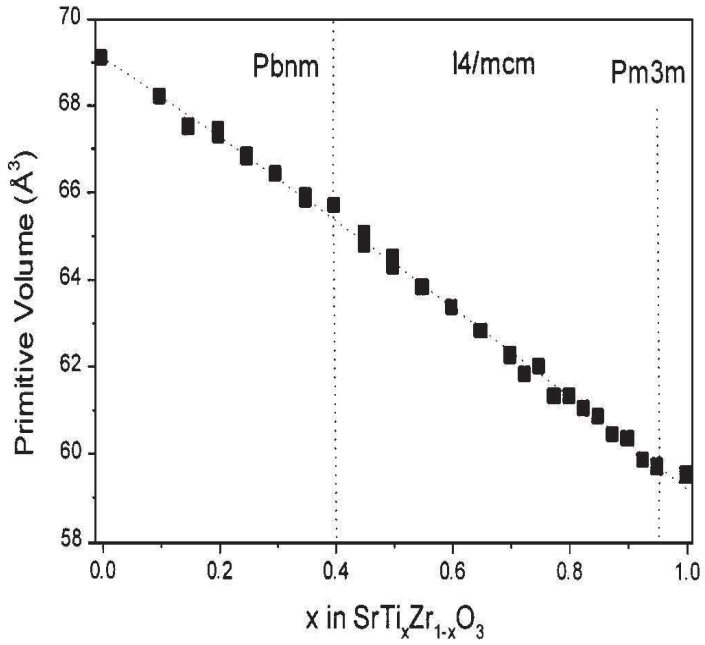

Figure 2.1. Phase composition-dependent diagram variation in the volume per formula unit for $SrTi_xZ_{1-x}O_3$. Orthorhombic (*Pbmn*) → tetragonal (*I4/mcm*) → cubic (*Pm-3m)* at x=0, 0.4 0.95 respectively [7].

On the other hand, McKnight et al. investigated by resonant ultrasound spectroscopy at high and low temperature using ceramic samples of $Sr(Zr,Ti)O_3$ the different phase transitions due to octahedral tilting. They found four different phase transitions in where the elastic behavior associated with phase transitions as a function of composition in $SrTi_xZr_{1-x}O_3$ at room temperature is suggested to be equivalent to $SrZrO_3$ as function of temperature. The phase transitions that they reported are the following:

Orthorhombic (*Pnma*) ↔ orthorhombic (*Imma*) at $SrTi_{0.43}Zr_{0.57}O_3$, orthorhombic (*Imma*) ↔ tetragonal (*I4/mcm*) at $SrTi_{0.65}Zr_{0.35}O_3$, and tetragonal (*I4/mcm*) ↔ cubic (*Pm-3m*) at $SrTi_{0.95}Zr_{0.05}O_3$ [8]. The temperature- composition phase diagram that they presented is shown in the following figure.

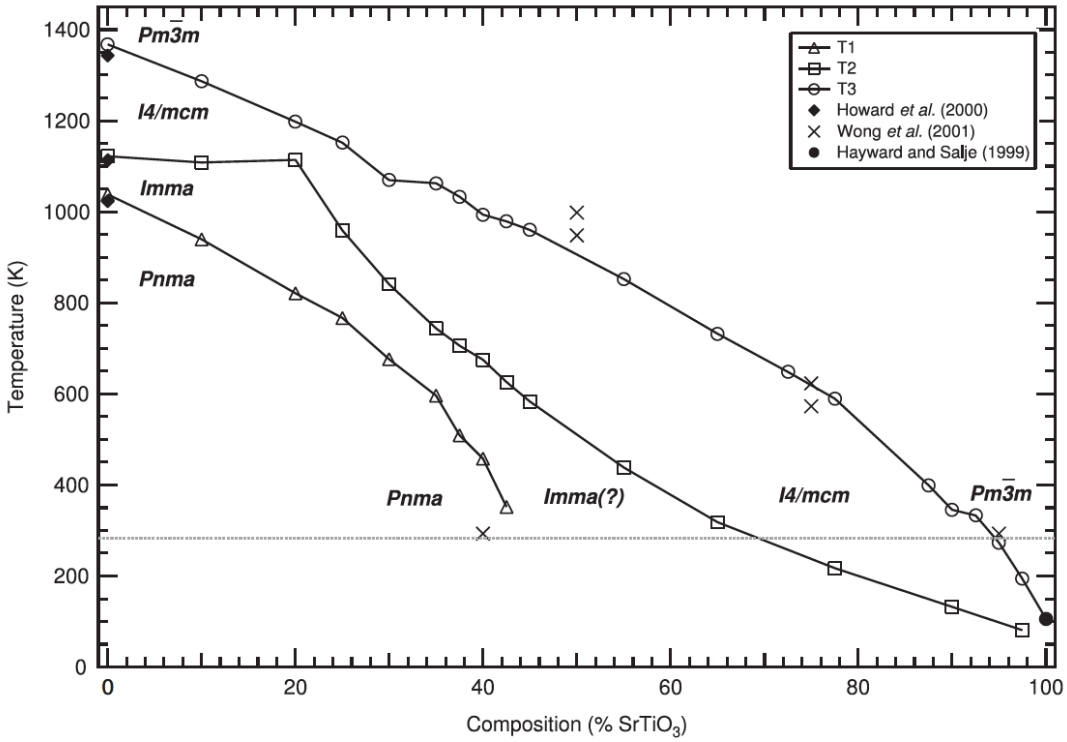

Figure 2.2. Temperature-composition phase diagram for $SrTi_xZr_{1-x}O_3$. Open circles, squares and triangles shows the transitions temperatures estimated from the data obtained by McKnight et al [8]. The closed diamonds represent the $SrZrO_3$ transitions temperatures by Howard et al [4]. Crosses mark the room temperature transitions determine by Wong et al [7]. The closed circle represents the $SrTiO_3$ phase transition reported by Hayward and Salje [9].

Wong et al presumed that because some reflections disappeared, which it is an indication of an orthorhombic symmetry, then the phase transition was from the orthorhombic (*Pnma*) to the tetragonal (I4/mcm) structure [7]. However, McKnight et al. stated that the pattern of evolution for $SrZrO_3$-rich compositions is very similar to the patterns for pure $SrZrO_3$ and therefore, the range of stability of the orthorhombic structure (*Imma*) within the phase diagram extends significantly.

2.1.2. - $SrTiO_3$ and $SrZO_3$ high-pressure phase transitions

High pressure studies on ideal perovskite materials is of great interest because some of their most important properties like ferroelectricity and piezoelectricity are related to small modifications of their ideal structure, and high pressure can induce those changes.

$SrTiO_3$ undergoes a phase transition at ambient temperature around 9.5 GPa, in where the structure changes from cubic to tetragonal [10-13]. In addition, no other transitions at room temperature to an orthorhombic or lower symmetric up to 54 GPa has been observed [12]. The phase transition from *Pm-3m* to *I4/mcm* is associated to two factors: i) the tilting of the BO_6 octahedral and ii) the simultaneous deformation of the octahedral. The tilt reduces the unit cell volume while the deformation increases it, which generates a small change of the volume of the unit cell during the phase transition, and only a small reduction of the unit cell volume in the tetragonal phase [14].

Moreover, the evolution of the distortion with increasing pressure of $SrZrO_3$ by using EXAFS showed that there is a phase transition from orthorhombic to cubic structure at 25 GPa [15]. However, a high-pressure Raman study from 0.1 to 40 GPa did not show any evidence of structural changes for pure $SrZrO_3$ ceramics [16].

2.2. – Structure and phase transitions of potassium tantalate and potassium niobate

Potassium tantalate ($KTaO_3$) has a cubic structure at room temperature, and it is an incipient ferroelectric material like $SrTiO_3$ in which quantum fluctuations at very low temperatures prevent a displacive ferroelectric transition to take place. As the temperature decreases the dielectric constant increases up to 5000 below 10 K while it still preserves the cubic perovskite symmetry [17, 18]. However, external conditions or forces (dopants, electric field or strain) can influence the ferroelectric ordering and quantum effects and a ferroelectric phase transition can occur [19, 20].

Potassium niobate ($KNbO_3$) exhibits three structural transitions with decreasing temperature at ambient pressure which are the following: cubic (*Pm3m*) ↔ tetragonal (*P4mm*) at 691 k, then tetragonal ↔ orthorhombic (*Amm2*) at 489 k, and finally from orthorhombic ↔ rhombohedral (*R3m*) at 263 k. The highest temperature cubic phase is

paraelectric and all the other three are ferroelectric [21], and the dielectric constant for a pure single crystal of $KNbO_3$ at the ferroelectric to paraelectric phase transition is around 4000 [22]. At the temperature at which both materials are cubic, the lattice parameter of $KNbO_3$ is 4.00226 Å and $KTaO_3$ is 4.0026 Å. This produce the attention of researchers to study solid solutions of these materials since it could generate a lattice in which there will be minimal structural perturbations, and it might produce improvements on the dielectric properties [22].

2.2.1. - $KNbO_3$- $KTaO_3$ solid solution

The $K(Ta_{1-x}Nb_x)O_3$ (KNT or KTN) system is a ferroelectric material for $x \geq 0.05$ and have the same three phase transitions as $KNbO_3$ (tetragonal ↔ orthorhombic ↔ rhombohedral). The solid solution of this system was first study by Barrett and Reisman using thermal and X-ray diffraction methods [23,24]. Figure 2.3 shows the temperature-composition phase diagram for $K(Ta_{1-x}Nb_x)O_3$ reported by Rytz [25].

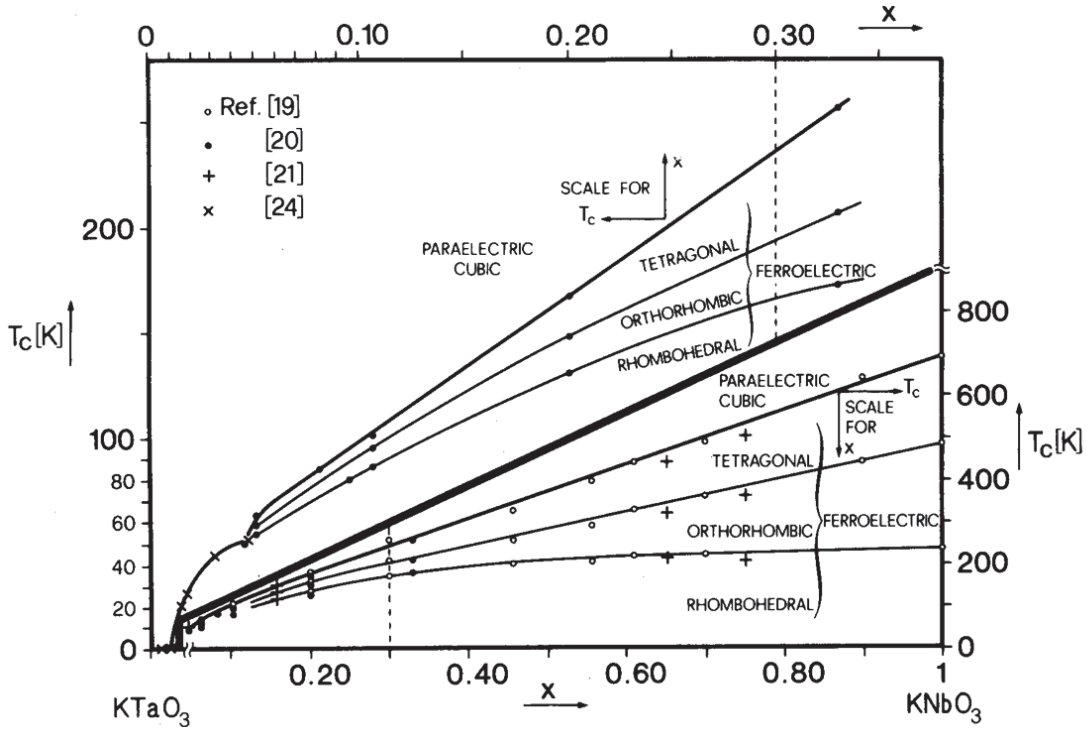

Figure 2.3. Concentration dependence phase transitions for KTN. Two different scales are shown for $0 \leq x \leq 0.30$ and $0.05 \leq x \leq 1.00$ [25].

Moreover, Triebwasser studied the dielectric constant of solid solutions of single crystals of $KNbO_3$-$KTaO_3$ and it was found that: i) the Curie temperature moves to lower temperatures as the concentration of $KTaO_3$ increases and ii) the peak of the dielectric constant increases with increasing $KTaO_3$ concentrations [22]. This is shown in the following picture.

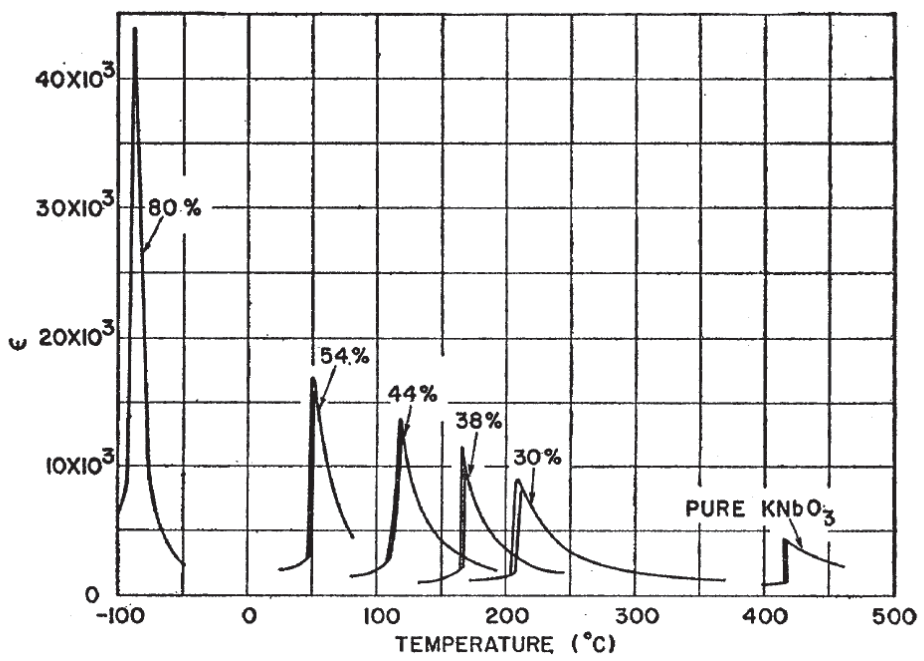

Figure 2.4. Dielectric constant versus temperature for solid solution of KTaO3-KNbO3 single crystals.

Alkali niobates systems have some drawbacks when it comes to their preparation due to the low melting temperature of some starting materials, stoichiometry problems that will affect the final properties, and complex densification. These require the optimization of the processing conditions for these types of materials [26]. By introducing and excess of alkaline elements is possible to reduce the volatilization of the elements and keep the stoichiometry of the compounds [27,28]. In addition, by creating an atmospheric powder in sealed crucibles during the calcination and sintering process, the mass loss is reduced and it is possible to improve the densification of samples [29]. The phase diagram used during this investigation to calcine and sinter the different

$K(Ta_{1-x})Nb_xO_3$ composition is the one reported by Reisman [24] and it is shown in the following figure.

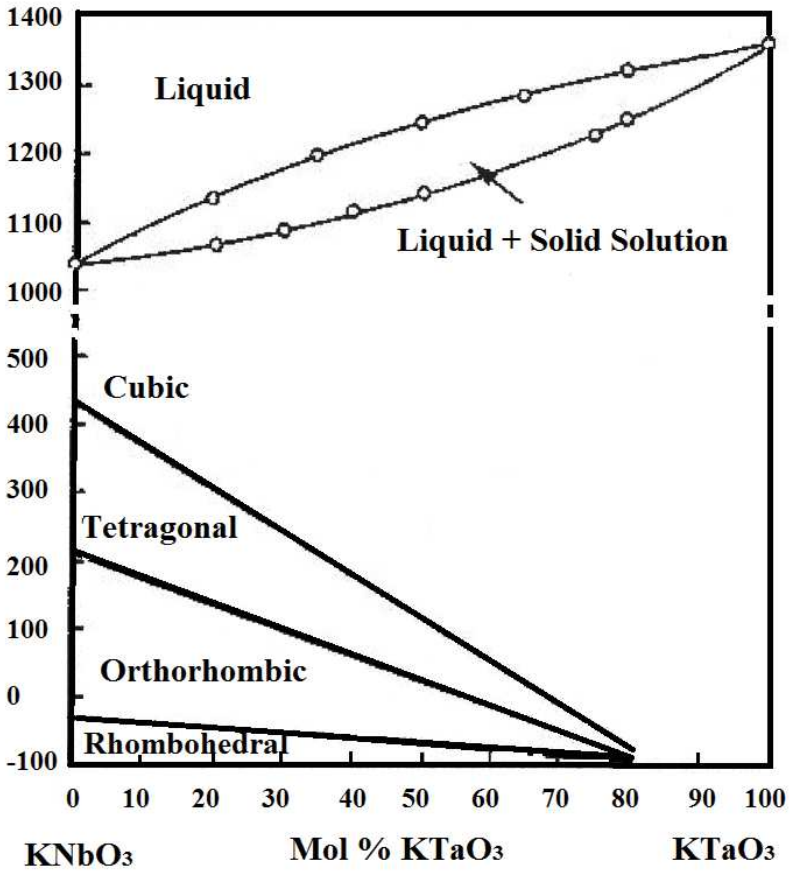

Figure 2.5. Phase diagram for $KNbO_3$-$KTaO_3$ [24]

2.2.2. - $KNbO_3$- $KTaO_3$ high-pressure phase transitions

The behavior under high pressure at room temperature for $KNbO_3$ has been highly studied and provides an example for studies related to paraelectric to ferroelectric transitions. Two high-pressure Raman scattering experiments have been reported for $KNbO_3$. The first one was to investigate the orthorhombic stability at room temperature, and it was detected that around 9 to 10 GPa there is a phase transition to a cubic structure [30]. Moreover, by using single crystal up to 20 GPa it was found three different phases that take place at around 2, 6 and 9 GPa until there is an amorphous phase near 15 GPa without finding a cubic phase during the experiment. [31]. Later, an energy-dispersive x-

ray diffraction study was used to explore the phase diagram of $KNbO_3$ up to 19 GPa. It was reported an orthorhombic to tetragonal transition in the 4-5 GPa range, followed by a tetragonal to cubic phase transition at 9 GPa [32]. Kobayashi et al, carried out an angle-dispersive powder diffraction study using synchrotron radiation at room temperature up to 69 GPa and they found at 10.5 GPa a phase transition from orthorhombic to cubic phase [33]. Finally, a theoretically study of the crystallography phase transition in $KNbO_3$ was done by Li et al., and they found two-phase transitions induced by pressure. The first one is from orthorhombic to cubic at 13.2 GPa and the second from cubic to orthorhombic at 39.7 GPa [34]. Even though, the behavior under pressure of $KNbO_3$ has been extremely study during the last years, it has not being reported any experiments on high-pressure for pure $KTaO_3$, this might be due to the stability of the cubic phase.

Mirza et al. performed a high pressure Raman study of $KNbO_3$- $KTaO_3$ mixed crystal for Nb rich concentration, and they reported a phase diagram of the different phase transitions depending on pressure and composition [35].

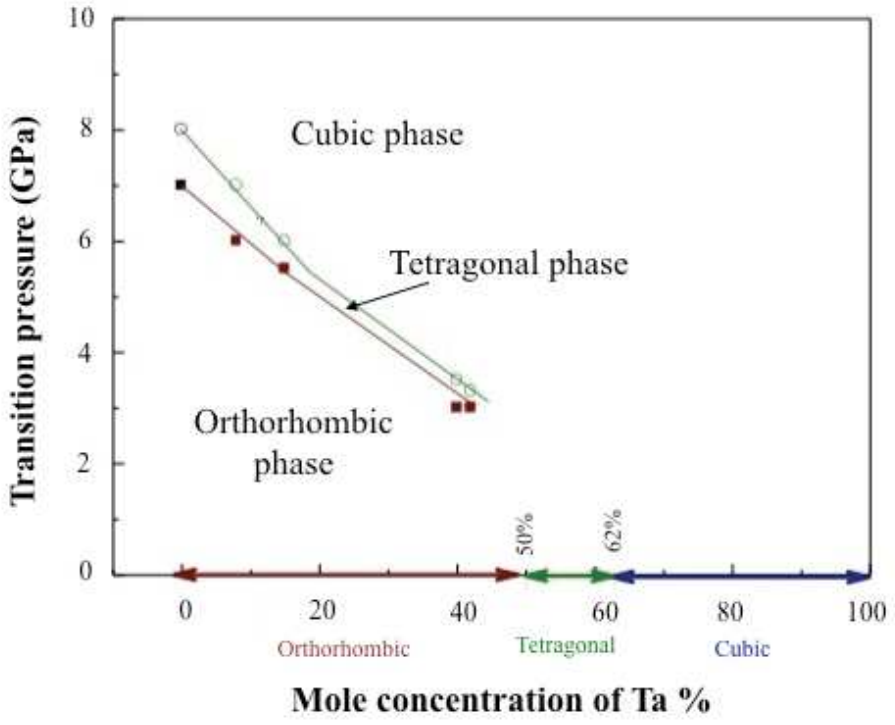

Figure 2.6. Pressure-composition phase diagram for the $KNbO_3$- $KTaO_3$ mixed crystals. The lines are to guide the reader [35].

In this phase diagram they showed the different values depending on pressure of the orthorhombic to tetragonal (O-T) and tetragonal to cubic (T-C) phase transitions for different percentages of mole concentration of Ta. However, for concentration of 40 and 42% of Ta they stated that it was difficult to accurately determine the pressure at which the O-T and T-C phase transition occurred, and this was due to the narrow pressure ranges at which the step-jump happened [35].

2.2.3. - Potassium Sodium Niobate

Potassium sodium niobate (KNN) is one of the most studied lead-free ferroelectric systems beside bismuth sodium titanate (BNT) and barium titanate (BT) due to the higher Curie temperature and excellent piezoelectric properties compared to PZT materials [36-37]. Diverse studies have been performed to optimize the densification of the ceramics and enhance the piezoelectric properties like: adding $BaTiO_3$, $SrTiO_3$ and $CaTiO_3$ [38-40] compounds to form solid solutions, using dopants from the copper family [41, 42], or processing conditions like hot pressing or spark plasma sintering [43, 44].

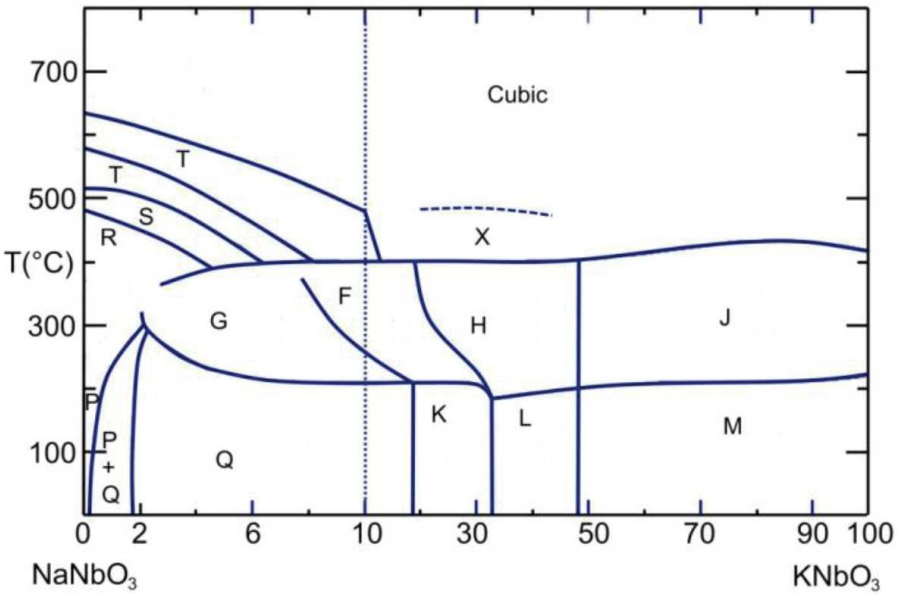

Figure 2.7. Phase diagram of $K_xNa_{1-x}NbO_3$ depending on temperature and composition. Regions labeled with Q, K, and L, R are monoclinic ferroelectric; M, G is orthorhombic ferroelectric; F, H and J are tetragonal ferroelectric, P is orthorhombic paraelectric, S and T are tetragonal, and X is cubic [45,46].

$K_xNa_{1-x}NbO_3$ has several phase transitions and morphotropic phase boundaries (MPBs) depending on temperature and composition [45,46] making it a complex system. The term morphotropic phase boundaries (MPBs) is used to mention a phase transition between two ferroelectric phases as a result of varying the composition or mechanical pressure [47]. At room temperature, the MPBs for KN are at 17.5 %, 32.5 % and 47.5 % Nb content. The phase diagram of KNN in function of the temperature and composition is shown in Figure 2.7.

Egerton et al. [48] reported an enhancing of the ferroelectric properties for KNN ceramics when the ratio of potassium and sodium was of 50/50. Later on, single crystals of the same composition were prepared and the values of these were compared to ceramics [49]. The dielectric constant values that they found at room temperature are given in the Table 2.1.

Table 2.1. Values of the temperatures of orthorhombic-tetragonal and tetragonal-cubic phase transitions, and the dielectric constant and dielectric losses at room temperature at a frequency of 100KHz [49].

	T_{O-T}	T_{T-C}	**Dielectric constant**	**Dielectric loss (%)**
$K_{0.5}Na_{0.5}NbO_3$ (Single crystal [1-31])	192	410	1015	1
$K_{0.5}Na_{0.5}NbO_3$ (Single crystal [-3-2-3])	193	409	650	1
$K_{0.5}Na_{0.5}NbO_3$ (Ceramic)	193	411	750	1

2.3. – Perspectives

To the best of our knowledge, it has not been reported any high-pressure experiments for $SrTi_xZr_{1-x}O_3$ solid solutions or for the rich Ta part in $K(Ta_{1-x}Nb_x)O_3$, which makes it very interesting to explore different compositions and to study the possible phase transitions induced by pressure in these systems.

In addition, it would be interesting to investigate the influence of different sintering methods on KNbO3-$KTaO_3$ ceramics and observe the possible improvements on their final ferroelectric properties. Moreover, we propose to study $(K_xNa_{1-x})Nb0.6Ta_{0.4}O_3$ ceramics to detect the influence of sodium as a dopant on the final ferroelectric properties of these materials.

Bibliography

[1] J. Wu, D. Xiao, J. Zhu, Potassium−Sodium Niobate Lead-Free Piezoelectric Materials: Past, Present, and Future of Phase Boundaries, Chem. Rev. 115 (2015) 2559−2595.

[2] J. Rödel, W. Jo, K. Seifert, E-M. Anton, T. Granzow, D. Damjanovic, Perspective on the Development of Lead-free Piezoceramics, J. Am. Ceram. Soc, 92 (2009) 1153-77.

[3] W. G. Nilsen, J.G Skinner, Raman Spectrum of Strontium Titanate, J. Chem. Phys 48 (1968) 2240-2248

[4] C. J. Howard, K.S. Knight, B.J. Kennedy. E.H. Kisi, The structural phase transitions in strontium zirconate revisited J. Phys.: Condens. Matter. 12 (2000) L677–83.

[5] T. Tsurumi, T. Harigai, D. Tanaka, S.M Nam, H. Kokemoto, S.Wada, K. Satio, Artificial ferroelectricity in perovskite superlattices, Appl. Phys. Lett 85 (2004) 5016.

[6] K. Yang, C.L Wang, J.C Li, M.L Zhao, X.Y Wang, Strain induce ferroelectricity in the $SrZrO_3/SrTiO_3$ superlattice: first principles study, Solid State Commun. 139 (2006) 144-147.

[7] T.K-Y. Wong, B.J. Kennedy, C.J. Howard, B.A. Hunter, T. Vogt, Crystal structure and phase transitions in the $SrTiO_3$-$SrZO_3$ solid solution, J. Solid State Chem. 156 (2001) 255-263.

[8] R.E.A Mcknight, B.J Kennedy, Q. Zhou, M.A Carpenter, Elastic anomalies associated with transformation sequences in perovskites: II. The strontium zirconate-titanate $Sr(Zr,Ti)O_3$ solid solutions series, J.Phys.:Condens. Matter 21 (2009) 015902.

[9] S.A. Hayward, E. K.H. Salje, Cubic-tetragonal phase transition in SrTiO3 revisited: Landau theory and transition mechanism, Phase Transit. 68 (1999) 501–22.

[10] G.A. Samara, T. Sakudo, K. Yoshimitsu, Important Generalization Concerning the Role of Competing Forces in Displacive Phase Transitions, Phys. Rev. Lett. 35 (1975) 1767.

[11] D. Lheureux, A. Polian, M. Fischer, M. Gauthier, J.-P. Itié, Ultrasonic and brillouin scattering measurements under pressure near the structural phase transition of strontium titanate, in 2000 IEEE Int Ultrason Symp Proc. (2000) 557–560.

[12] M. Guennou, P. Bouvier, J. Kreisel, Pressure-temperature phase diagram of $SrTiO_3$ up to 53 GPa, Phys. Rev. B, 81 (2010) 054115.

[13] S.-C. Weng, R. Xu , A. H. Said, B. M. Leu, Y. Ding , H. Hong , X. Fang, M.Y. Chou, A. Bosak, P. Abbamonte, S. L. Cooper, E. Fradkin, S.-L. Chang, T.-C. Chiang, Pressure-induced antiferrodistortive phase transition in SrTiO3: Common scaling of soft-mode with pressure and temperature, EPL. 107 (2014) 36006.

[14] E.K.H. Salje, M. Guennou, P. Bouvier, M.A. Carpenter, J. Kreisel, High pressure ferroelastic phase transition in $SrTiO_3$, J. Phys.: Condense.Matter 23 (2011) 275901.

[15] D. Andrault, J.P. Poirier, Evolution of the Distortion of Perovskites Under Pressure: An EXAFS Study of $BaZrO_3$, $SrZrO_3$ and $CaGeO_3$, Phys. Chem. Minerals. 18 (1991) 91-105.

[16] A. Slodczyk, M.-H. Limage, P. Colomban, O. Zaafrani, F. Grasset, J. Loricourt, B. Sala, Substitution and proton doping effect on $SrZrO_3$ behavior: high-pressure Raman study, J. Raman Spectrosc. 42 (2011) 2089-2099.

[17] B.T. Matthias, New Ferroelectric Crystals, Phys. Rev. 75 (1949) 1771

[18] Y. Ichikawa, M. Nagai, and K. Tanaka, Direct observation of the soft-mode dispersion in the incipient ferroelectric $KTaO_3$, Phys. Rev. B, 71 (2005) 092106.

[19] G. A. Samara, The relaxational properties of compositionally disordered ABO_3 perovskites, J. Phys. : Condens. Matter. 15 (2003) R367.

[20] J. H. Haeni, P. Irvin, W. Chang, R. Uecker, P. Reiche, Y. L. Li, S. Choudhury, W. Tian, M. E. Hawley, B. Craigo, et al., Room-temperature ferroelectricity in strained $SrTiO_3$, Nature, 430 (2004) 758-761.

[21] A.W. Hewat, Cubic-tetragonal-orthorhombic- rhombohedral ferroelectric transitions in perovskites potassium niobate: neutron powder profile refinement of the structures, J. Phys. C.: Solid State Phys. 6 (1973) 2559-2572.

[22] S. Triebwassar, Study of Ferroelectric Transitions of Solid-Solutions single Crystals of $KNbO_3$- $KTaO_3$, Phys. Rev. 114 (1959) 63-70.

[23] J. Barrett, Dielectric Constant in Perovskite Type crystals, Phys. Rev. 86 (1952) 118

[24] A. Reisman, S.TRiebwasser, F. Holtzberg, Phase Diagram of the System KNbO3-KTaO3 by the Methods of Differential Thermal and Resistance Analysis, J. Am. Chem. Soc. 77 (1955) 4228-4230.

[25] R. Rytz, Crystal Growth of the $K(Ta_{1-x})Nb_xO_3$ ($0 < x \leq 0.04$) Solid Solutions by a Slow-Cooling method, J. Cryst. Growth, 59 (1982) 468-484.

[26] M. matsubara T.Yamaguchi, W. sakamoto, K. Kikuta, T. yogo, S. Hirano, Processing and Piezoelectric Properties of Lead-Free (K,Na)(Nb,Ta)O_3 Ceramics, J. Am. Ceram. Soc. 88 (2005) 1160-1196.

[27] K. Yoshikawa, T. Asaka, M. Higuchi, Y. Azuma, K. Katayama, Effects of excess K_2O and processing conditions on the preparation of dense k($Ta_{1-x}Nb_x$)O_3 ceramics, Ceram. Int. 34 (2008) 609-613.

[28] A.K. Axelsson, Y. Pan, M. Valant, N.Alford, Synthesis, Sintering, and Microwave Dielectric Properties of $KTaO_3$ Ceramics, J. Am. Ceram. Soc. 92 (2009)1773–1778.

[29] Y. Wang, D. Damjanovic, N. Klein, N. Setter, High-Temperature Instability of Li- and Ta-Modified (K,Na)NbO3 Piezoceramics, J. Am. Ceram. Soc. 91 (2008) 1962-1970.

[30] D. Gourdain, E. Moya, J.C. Chervin, B. Canny, Ph. Pruzan, Ferroelectric-paraelectric phase transition in $KNbO_3$ at high pressure, Phys. Rev. B, 52 (1995) 3108.

[31] Z. X. Shen, Z. P. Hu, T. C. Chong, C. Y. Beh, S.H. Tang, M. H. Kuok, Pressure induced strong mode coupling and phase transitions in $KNbO_3$, Phys. Rev. B, 52 (1995) 3976.

[32] J.C. Chervin, J.P. Itié, D. Gourdain, Ph. Pruzan, Energy dispersive X-ray diffraction study of $KNbO_3$ up to 19 GPa at room temperature, Solid State Commun. 110 (1999) P247–51.

[33] Y. Kobayashi, S. Endo, T. Ashida, L.C. Ming, T. Kikegawa, High-pressure phase above 40 GPa in ferroelectric $KNbO_3$, Phys. Rev. B, 61 (2000) 5819.

[34] S. Li1, R. Ahuja, B. Johansson, Pressure-induced phase transitions of $KNbO_3$. J. Phys. Condens. Matter, 14 (2002) 10873–10877.

[35] M. M. Shamim, T. Ishidate, K. Ohi, High Pressure Raman Study of $KNbO_3$- $KTaO_3$ and $KNbO_3$- $NaNbO_3$ Mixed Crystals, J. Phys. Soc. Jpn. 72 (2003) 551-555.

[36] Y. Saito, H. Takao, T. Tani, T. Nanoyama, K. Takotori, T. Homma, T. Nayaga, M. Nakamura, Lead-free piezoceramics, Nature, 432 (2004) 84–87.

[37] S. Zhang, R. Xia, T.R. Shrout, Lead-free piezoelectric ceramics vs. PZT? J. Electroceram. 19 (2007) 251–257.

[38] Y. Guo, K. Kakimoto, H. Ohsato, Structure and electrical properties of lead-free ($Na_{0.5}K_{0.5}$)NbO_3-$BaTiO_3$, Jpn. J. Appl. Phys. 43 (2004) 6662-6666.

[39] J. Kroupa, J. Petzelt, B. Malic, and M. Kosec, Electro-optic properties of KNN-STO lead-free ceramics, J. Phys D, 38 (2005) 679-81.

[40] R.-C. Chang, S.-Y. Chu, Y.-F. Lin, C.-S. Hong, and Y.-P. Wong, An investigation of (Na0.5K0.5)NbO_3-$CaTiO_3$ based lead-free ceramics and surface acoustic wave devices, J. Eur. Ceram. Soc, 27 (2007) 4453-60.

[41] M. Matsubara, T. Yamaguchi, K. Kikuta, S. Hirano, Sinterability and piezoelectric properties of (K,Na)NbO_3 ceramics with novel sintering aid, Jpn. J. Appl. Phys. 43 (2004) 7159-63.

[42] S.-L.Yang, C.-C. Tsai, C.-S. Hong, S.-Y. Chu, Effects of sintering aid $CuTa_2O_6$ on piezoelectric and dielectric properties of sodium potassium niobate ceramics, Mater. Res. Bull. 47 (2012) 998-1003

[43] G.H. Haertling, Properties of hot-pressed ferroelectric alkali niobate ceramics, J. Am. Ceram. Soc. 50 (1967) 329.

[44] J. F. Li, K. Wang, B. P. Zhang, L. M. Zhang, Ferroelectric and piezoelectric properties of fine-grained $Na_{0.5}K_{0.5}NbO_3$ lead-free piezoelectric ceramics prepared by spark plasma sintering, J. Am. Ceram. Soc. 89 (2006) 706-9.

[45] M. Ahtee, A. M. Glazer, Lattice parameters and tilted octahedra in sodium-potassium niobate solid solutions, Acta Crystallogr. Sect. A: Found. Crystallog, 32 (1976) 434-45.

[46] M. Ahtee, A. W. Hewat, Structural phase-transitions in sodium-potassium niobate solid-solutions by neutron powder diffraction, Acta Crystallogr. Sect. A: Found. Crystallog, 34 (1978) 309-17.

[47] A.-B. M. A. Ibrahim, R. Murgan, M.K.A Rahman and J.Osman, Morphotropic Phase Boundary in Ferroelectric Materials, in: Mickaël Lallart (Ed.), Ferroelectrics - Physical Effects. Available from: http://www.intechopen.com/books/ferroelectrics-physical-effects/morphotropic-phase-boundary-in-ferroelectric-materials

[48] L. Egerton, D. M. Dillon, Piezoelectric and dielectric properties of ceramics in the system potassium sodium niobate, J. Am. Ceram. Soc. 42 (1959) 438-42.

[49] H. Urši, A. Benan, M. Škarabot, M. Godec, M. Kosec, Dielectric, ferroelectric, piezoelectric, and electrostrictive properties of $K_{0.5}Na_{0.5}NbO_3$ single crystals. J. Appl. Phys. 107 (2010) 033705.

CHAPTER III
SYNTHESIS, SINTERING PROCESS AND CHARACTERIZATION TECHNIQUES

The different activities that were carried out in order to study the synthesis, sintering process and characterization techniques on $SrTi_{1-x}Zr_xO_3$, $KNb_{1-x}Ta_xO_3$ and $K_xNa_{1-x}Nb_{0.6}Ta_{0.4}O_3$ powders and ceramics are presented in this chapter. The first part will describe the synthesis technique used to obtain crystalline compounds, and the second part will discuss the different sintering processes used in order to well-densified the $KNb_{1-x}Ta_xO_3$ and $K_xNa_{1-x}Ta_{0.4}Nb_{0.6}O_3$ sample. Finally, it will be described the characterization techniques used in this investigation.

3.1. - Synthesis of perovskites materials

The synthesis for both $SrTi_{1-x}Zr_xO_3$ and $KNb_{1-x}Ta_xO_3$ compositions was done through a solid-state reaction. Diverse calcination conditions were performed in order to obtain well-crystallized pure-phase powders without residual phases.

3.1.1. – Strontium titanium zirconate compounds

$SrTi_{1-x}Zr_xO_3$ powders were prepared by solid-state reaction of strontium carbonate ($SrCO_3$, 99.9%), titanium oxide (TiO_2, 99.9%) and zirconium oxide (ZrO_2, 99.9%) through a two-stage calcination process. The starting raw materials were first ball-milled separately in a polyethylene bottle using zirconia balls and ethanol as a grinding medium for 24h. After the powders were dried and sieved, they were mixed stoichiometrically in ethanol and ground by using an agate mortar and a pestle until a homogeneous dried mixture was obtained. The first calcination stage of the starting raw materials was performed in air at 1200 °C for 24 hours, followed by a second calcination cycle up to 1610 °C for 5 hours with an intermediate mixing and grinding in an agate mortar.

Highly crystallized materials could not be obtained by simple one-stage calcinations as shown by the enlarge diffraction profile in figure 3.1. The best crystallization was achieved with the above-described two-stage calcination

process.These results confirm the formation of a single-phase perovskite material without any parasitic or residual phases detectable by X-ray.

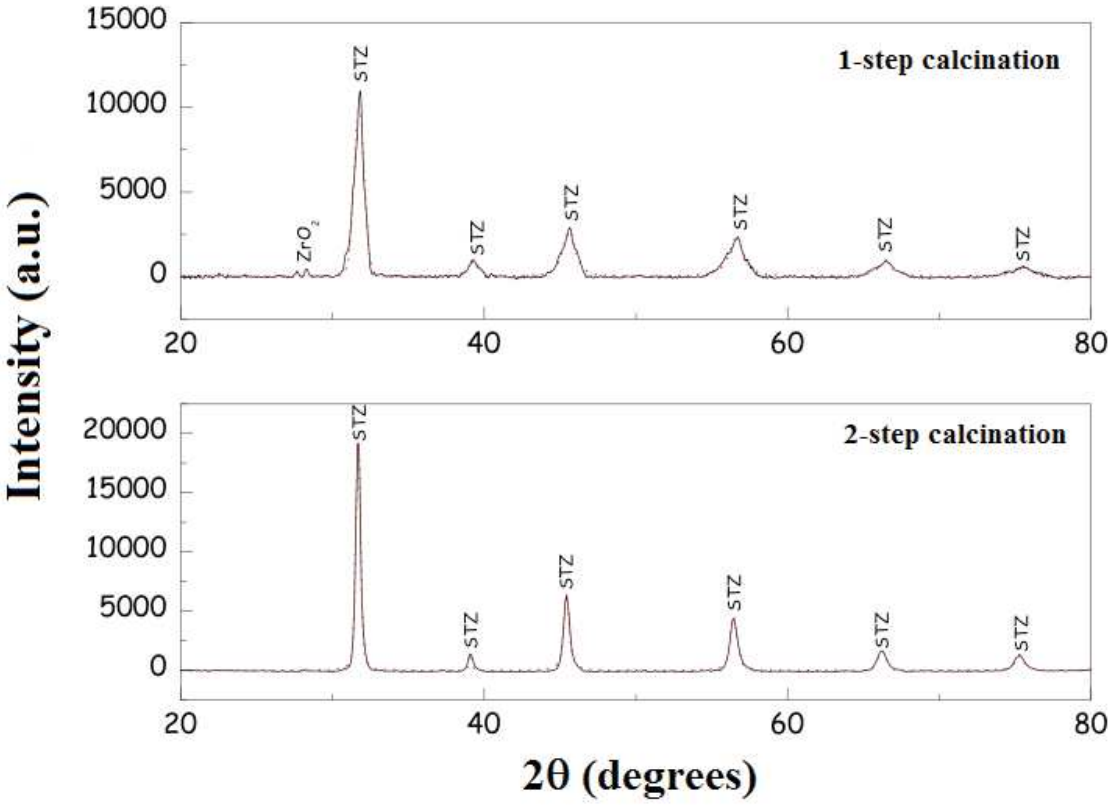

Figure 3.1. Experimental (…) and fitted (–) XRD profiles of $SrTi_{0.6}Zr_{0.4}O_3$ powders at room pressure and room temperature obtained through one-stage and two-stage calcinations at 1610°C.

A Williamson-Hall analysis was performed to study the peak broadening and to evaluate the average crystalline size (Γ) which is related to the size of a coherently diffraction domain, and the lattice strain (ε) that rise from crystal imperfections such as lattice dislocations and/or sinter stress. Figure 3.2 shows the linear fit of the data. The crystalline size (Γ) was estimated from the *y*-axis intercept and the strain (ε) from the slope of the fit. We can observe that by using the 2-step calcinations process Γ increases and ε reduces confirming a better crystalline powder.

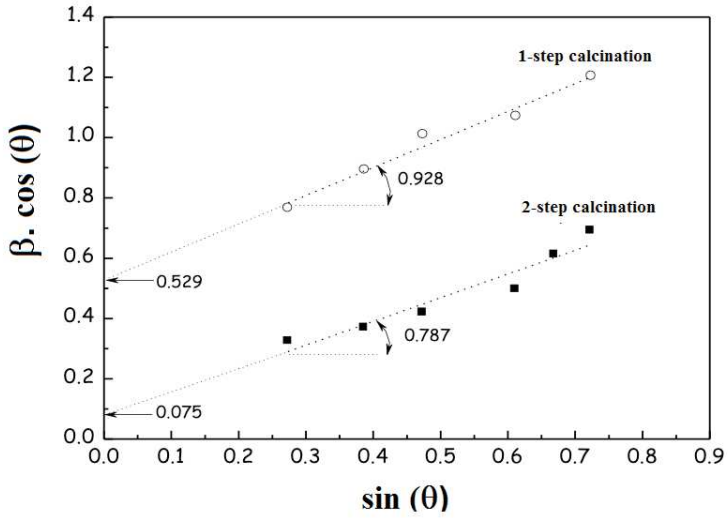

Figure 3.2. Plot of $\beta.\cos\theta$ versus $\sin\theta$ of $SrTi_{0.6}Zr_{0.4}O_3$ powders. Assuming that the particle size and strain contributions to line broadening are independent, the Williamson-Hall equation gives: $\beta.\cos\theta = K\lambda/\Gamma + C\varepsilon.\sin\theta$ (with β: full width at half maximum corrected from instrumental broadening (rad); K: shape factor (0.9); λ :wavelength of Cu K_{a1} radiation (0.154 nm); Γ: crystalline size (nm); C: constant; ε: lattice strain)

3.1.2. – Potassium niobium tantalate ($KNb_{1-x}Ta_xO_3$) and potassium sodium niobium tantalate ($K_xNa_{1-x}Ta_{0.4}Nb_{0.6}O_3$) compounds

$KNb_{1-x}Ta_xO_3$ (x= 0.9, 0.6, 0.5, 0.4) and $K_xNa_{1-x}Nb_{0.6}Ta_{0.4}O_3$ (x=0.9, 0.8, 0.7, 0.6, 0.5) samples were prepared by solid-state reaction of high purity K_2CO_3, Nb_2O_5, Ta_2O_5 and Na_2CO_3 powders through a one-stage calcination process. The starting raw materials were mixed stoichiometrically and it was added 5% of K_2CO_3 for all the composition in order to keep the desired composition after the sintering process. The starting materials were ground using an agate mortar and a pestle with ethanol until a homogeneous dried mixture was attained. In order to have a better reactivity, the mixed powders were first uniaxially pressed and calcined at different temperature in a range of 785 °C and 1150°C for 4h depending on the desired composition. The calcination temperatures used were the necessary to have well-crystallized powders without the presence of secondary phases. Applying lower temperatures with longer times or using double-calcination processes did not lead to obtain full reaction of the raw materials. After the calcination process, the samples were ground and mixed with alumina balls in an automatic planetary grinding

machine (Fritsch Pulverisette 6) for 30 minutes at 400 rpm. The ground powders were then sieved through a 100 μm mesh.

3.2. - Sintering of Perovskites materials

Solid state sintering is a technique of consolidating powders to produce density-controlled materials by use of thermal energy without melting all solid phases [1]. In this investigation, three main techniques were used to sinter the studied compounds. Figure 3.3 shows the schematic diagram of the sintering techniques used for the different synthesized powders.

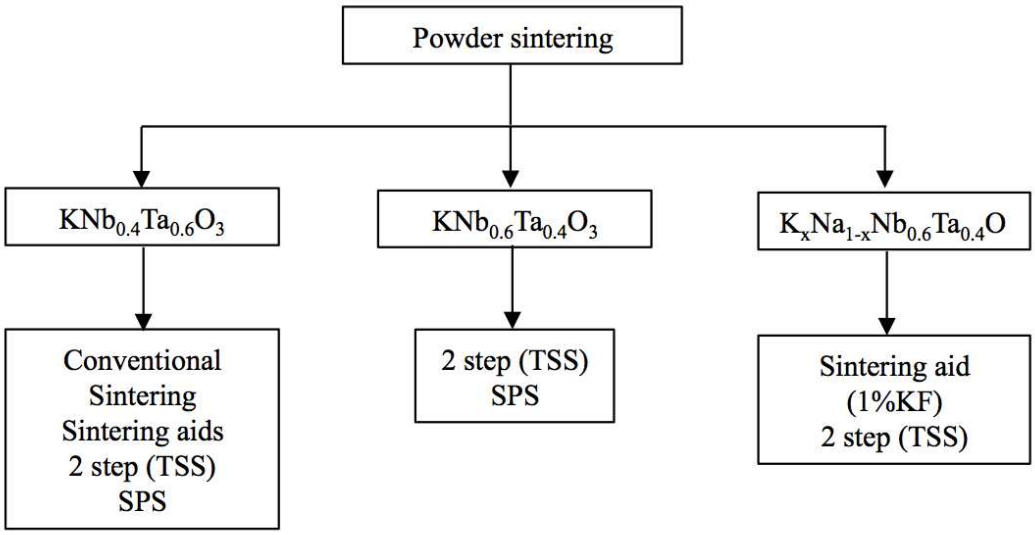

Figure 3.3. Flowchart of the sintering techniques used on this investigation for each compound.

It was first used the conventional sintering (CS) technique for $KNb_{0.4}Ta_{0.6}O_3$; however, this technique is known for having a limitation in achieving full density samples due to thermal sample stability which limit the sintering temperature, resulting in some porosity of the ceramics. In order to achieve higher density of the samples, a first strategy was used for $KNb_{0.4}Ta_{0.6}O_3$ where it was to keep the conventional sintering process and testing the reliability of different sintering aids. Further more, it was studied the sintering behavior of the ceramics with the use of two other sintering methods: 2 step sintering (TSS) and spark plasma sintering (SPS).

3.2.1. – Conventional sintering

Conventional sintering is one the most used technique to consolidate powder particles by heating a compacted pellet at a temperature lower than the melting temperature of the material. Resulting in a densification of the material by the effects of heat and this will produce an increase of the mechanical strength and generally a reduction of the porosity in the ceramics. Conventional solid state sintering involves the transport of material by diffusion. This diffusion is the movement of atoms or vacancies along the surface, grain boundary or through the material, figure 3.4 shows the different diffusion mechanism during the sintering process. In this process two types of changes occur: changes in the shape and size of pores, and changes in the shape and size of the grains. As the specific surface area increases, the pores will start to close and the volume will decrease leading to a densification and grain growth, which are temperature and time depending [1-2].

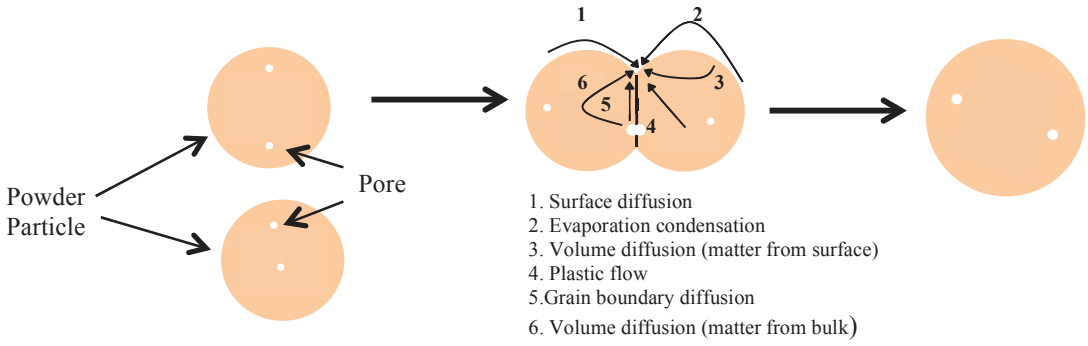

Figure 3.4. Diffusion mechanisms that occurs during a sintering process.

The calcined powders obtained were mixed with an APV (80%)/PEG (20%) binder aqueous solution before they were sieved and pressed again into pellets of 13 mm diameter. Finally, these green pellets were placed in an Al_2O_3 crucible and heat-treated in air at 600°C for 4h to remove the organic binder. Final firing was performed between 1200 and 1150°C for 6h depending on the composition. The green pellets were placed in an Al_2O_3 crucible and heat-treated in air at 600°C for 4h to remove the organic binder. Final firing was performed at 1150°C for 6h in sealed alumina crucibles, in where the pellets were surrounded with powder of the same composition to keep a saturated alkali-species atmosphere during the heat treatment and limiting the volatilization of alkali-

oxides. In order to achieve higher densities and improve dielectric properties of the material, a first strategy consisted in keeping this ordinary sintering process and testing the reliability of different sintering aids. A variety of oxides such as CuO, MnO_2, WO_3 have already been used to reach liquid phase sintering of $(K,Na)NbO_3$ but hardly experimented on $KNb_{1-x}Ta_xO_3$. While those oxides give interesting results in terms of morphology, electrical characteristics have still to be improved [3-7] and searching for better sintering aids has been always a focus of the field. Recently, a method named liquid phase screening has been proposed by K. Chen & al. to quickly screen potential sintering aids for $(K_{0.5}Na_{0.5})NbO_3$ ceramics and determine their wetting ability [6,8]. We applied this technique by using homemade $CuNb_2O_6$ and $CuTa_2O_6$ mixed oxides and KF, which has not been used before on KNT compounds. These additives appeared interesting as they contain host cations and represent a source of A-site or B-site ions, which might help to reduce some losses of these cations during the sintering process. Sintering aids (CuO, MnO_2, WO_3, $CuNb_2O_6$, $CuTa_2O_6$ and KF) were introduced by mixing 1wt% of these compounds with $KNb_{0.4}Ta_{0.6}O_3$ powders. This composition was studied because it presents a tetragonal structure at room temperature. The calcined powders were mixed along with the different sintering aids and the binder, and they were finally pressed. The binder was removed at 600°C for 4h and final firing was performed at 1150°C for 6h in sealed alumina crucibles. In addition, the conventional sintering was used for all $K_xNa_{1-x}Ta_{0.4}Nb_{0.6}O_3$ compounds using 1wt% of KF as sintering to improve the densification of ceramic. Table 3.1 shows the different conditions used during this process.

Table 3.1. Conventional sintering conditions used 1wt% of KF as sintering aid for $K_xNa_{1-x}Nb_{0.6}Ta_{0.4}O_3$ powders.

Composition	Temperature
$KNb_{0.6}Ta_{0.4}O_3$	1080°C/6h
$K_{0.9}Na_{0.1}Nb_{0.6}Ta_{0.4}O_3$	1080°C/6h
$K_{0.8}Na_{0.2}Nb_{0.6}Ta_{0.4}O_3$	1100°C/6h
$K_{0.7}Na_{0.3}Nb_{0.6}Ta_{0.4}O_3$	1170°C/6h
$K_{0.6}Na_{0.4}Nb_{0.6}Ta_{0.4}O_3$	1170°C/6h
$K_{0.5}Na_{0.5}Nb_{0.6}Ta_{0.4}O_3$	1170°C/6h

3.2.2. – Two step sintering

To further improve the sintering behavior of all compounds, we investigated the influence of the two-step sintering **(**TSS) technique, which it is an attractive and cost-effective sintering method that allows us to obtain well densified samples by adequate control procedures of the temperature and heating rate. In this process, the sample is first heated to a high temperature between the liquidus and the solidus lines in the phase diagram in order to have the presence of a liquid phase that will assist the sintering process, and it will help to reach an intermediate relative density (above 75%). After that step, the sample is rapidly cooled down and held at a lower temperature till full density is achieved. During the last stage of the sintering process, the grain growth takes place and this has an implication in the final properties of the ceramics, like mechanical resistance, density and others [9].

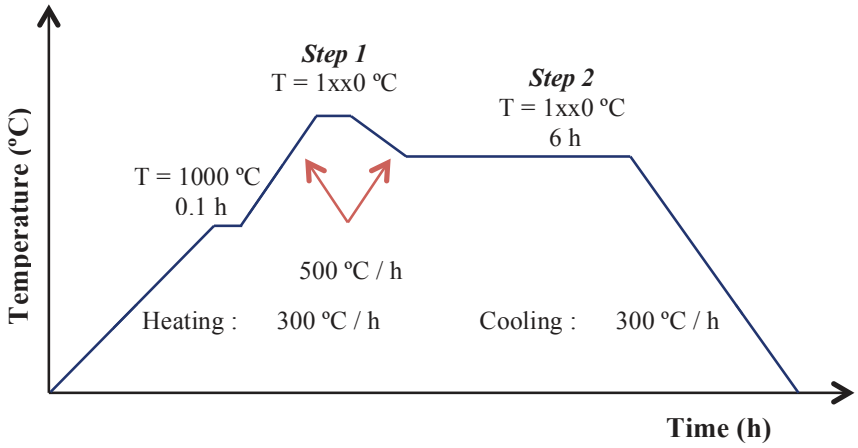

Figure 3.5. Two-step sintering cycle used in this investigation.

In a first step, approximately 0.8 g of the calcinated powders $KTa_{0.4}Nb_{0.6}O_3$, $KTa_{0.6}Nb_{0.4}O_3$ and $K_xNa_{1-x}Ta_{0.4}Nb_{0.6}O_3$ were mixed with a binder composed of 20% PEG and 80% APV in an agate mortar before being pressed into pellets of 13 mm diameter. The green samples were placed in an open Al_2O_3 crucible and heated in air at 600°C for 4h to remove the binder. Samples were covered with powder of the same composition. The pellets were first kept at 1000°C for 6 min in order to stabilize the temperature and then it was heated at a high rate of 500°C/h at a elevated temperature between 1150-1200 °C depending on the composition, near the liquidus line for a short

time (6 minutes) to reach a critical density via a liquid phase formation. Subsequently, the ceramics were rapidly cooled down (500°C/h) to a lower temperature 1100-1180°C and dwelled for 6h to ensure densification with limited grain growth. Figure 3.5 shows the two-step sintering cycle that was used.

Table 3.2. Details of the two-step sintering temperatures used for each composition

	$KNb_{1-x}Ta_xO_3$		$K_xNa_{1-x}Nb_{0.6}Ta_{0.4}O_3$				
X=	**0.6**	**0.4**	**0.5**	**0.6**	**0.7**	**0.8**	**0.9**
Step 1 Selected Temperature	1200°C/0.1h	1150°C/0.1h	1200°C/0.1h	1170°C/0.1h	1170°C/0.1h	1160°C/0.1h	1150°C/0.1h
Step 1 Real Temperature	1170°C/0.1h	1120°C/0.1h	1170°C/0.1h	1140°C/0.1h	1140°C/0.1h	1130°C/0.1h	1120°C/0.1h
Step 2	1150°C/6h	1100°C/6h	1180°C/6h	1150°C/6h	1150°C/6h	1100°C/6h	1100°C/6h

The sintering temperatures used for all the compositions are shown in the following table. These were the best conditions that we found during this investigation in order to have pure phases, limit the grain growth and obtaining dense pellets. It is important to note that on the first-step temperature there was a difference of 30 °C from the selected temperature to the one measured due to the inertia of the furnace.

3.2.3. – Spark plasma sintering

New techniques are used to rapid consolidate materials like spark plasma sintering (SPS), and it is a sintering technique that uses a uniaxial pressure and a pulsed (on-off) direct electrical current under low atmospheric pressure to perform high-speed consolidation of powder samples. The current passes through an electrically conductive die while the uniaxial pressure is delivered by two punches of the same composition of the die to compact the powder that has been place inside. This direct way of heating allows the application of very high heating and cooling rates, improving the densification over grain growth and allows keeping small grain size in the fully dense final products [10].

SPS experiments were performed on a Dr. Sinter 515S Syntex machine using a 13 mm diameter carbon die matrix and carbon punches. In order to limit the wear of the matrix and to easily remove the sintered pellets a Papyex® papers (0.2 mm in thickness) was used. It was added almost 1.5 g of powder for every sample that was prepared to insure that the pellets would be sufficiency thick to perform the later characterization of the same. Argon atmosphere was used in the sintering process and different temperatures were used depending on the composition, which are presented in Table 3.3. Once the samples were removed from the SPS machine, they were annealed at 700°C for 12h to suppress carbon traces.

Table 3.3. Conditions used to sinter different powder composition by SPS.

Composition	Temperature	Pressure (MPa)
$KNb_{0.4}Ta_{0.6}O_3$	1100°C/5min	100
$KNb_{0.6}Ta_{0.4}O_3$	1040°C/5min	100
$K_{0.9}Na_{0.1}Nb_{0.6}Ta_{0.4}O_3$	1000°C/1min	100
$K_{0.8}Na_{0.2}Nb_{0.6}Ta_{0.4}O_3$	1020°C/1min	100
$K_{0.5}Na_{0.5}Nb_{0.6}Ta_{0.4}O_3$	1050°C/1min	100

The following figure shows pellets of $KNb_{0.4}Ta_{0.6}O_3$ that were sintered through the three different methods that were described before.

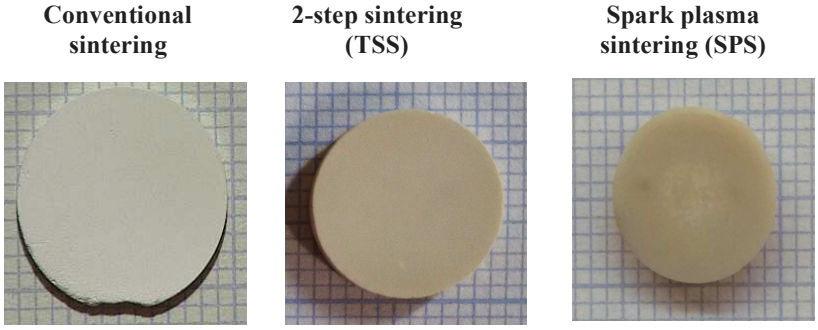

Figure 3.6. Optical observation of three different techniques used to sintering $KNb_{0.4}Ta_{0.6}O_3$ powders.

3.3. – Characterization techniques

Different methods of analysis were used in order to characterize the macro and microstructure of the studied compounds as well as their dielectric properties. A brief

description of the different techniques that were used during this investigation is listed below.

3.3.1. - X-Ray Diffraction

X-ray diffraction (XRD) is a non-destructive characterization technique used to identify crystalline phases present in a material. The physical phenomenon of XRD expresses the result of the fundamental interaction between an electromagnetic wave, X-rays, and the ordered matter [11].

The crystallographic profiles of the calcined powders and the ceramics were determined by using a PANAalytical X'pert Pro diffractometer with Cu-K radiation in where λ was 1.540598 and 1.544426 Å for $K\alpha_1$ and $K\alpha_2$ at 45 kV and 30mA. The data were obtained over 20° to 100° 2θ range with a 0.016 step size. After collecting the data, a profile matching on the starting powder was performed with the use of the FULLPROF software [12].

3.3.2. – Density

The apparent bulk densities of the sintered pellets were measured through the Archimedes method, based on the ASTM standard C20-00 [13]. After measuring the weigh of samples in air, they were placed in distilled water and drawn for about 5 min to remove air from the surface of the sample. By using an analysis scale, we were able to weigh the ceramics inside the water. The temperature of the water was recorded using an analogue thermometer. The relative density was calculated by dividing the experimental density by the theoretical one. The theoretical density of each composition is the average mass per unit cell divided by the unit cell volume; they were determined from the X-ray powder diffractions that were performed during this investigation.

3.3.3. - Scanning Electron Microscopy

Scanning electron microscope (SEM) is a technique used to obtain high-resolution images of the sample surface. This technique is based on detecting the backscattered (BSE) and secondary (SE) electrons that are produced at the top of the microscope by an electron gun, which impacts the surface of a target sample. The SE come from an inelastic interaction, and it will give information about the surface topography. Moreover,

the BSE is the result of quasi-elastic interactions between the incident electrons and provide qualitative information on the chemical contrast of the sample under study. In addition, some of the SEM machines are equipped with an energy dispersive X-Ray spectroscopy (EDS), which gives information about the element composition of the analyzed material [14].

The microstructure and composition of the samples were performed on the cross-sectional of the pellets by using a FEI Quanta 200 FEG scanning electron microscope, which is coupled with a silicon drift detector (SDD)-X-Max^N energy dispersive X-ray spectroscopy. The pellets were attached to a sample holder using a conducting carbon tape and the chemical composition was determined using the K edge with an accelerating voltage of 15 kV, and the acquisition time was of 60 seconds per element.

3.3.4. - Electron Backscattered Diffraction

Electron backscatter diffraction (EBSD) is a microstructural characterization technique that provides information about the crystallographic nature of most inorganic materials. This technique can be carried out by using a SEM equipped with an accessory system of the EBSD attached to it [15]. Therefore, it can determine the grain size, grain orientation and grain boundary, as well as texture and phase identification of the analyzed samples. The sample size might be studied from the millimeter till the nanograin size. The sample under study has to have a flat and mirror like surface.

The EBSD study was carried out using a SEM Camscan Crystal Probe X500FE equipped with an EBSD HKL NordlysNano detector and EDS X-Max^N 20mm^2 detector was used for the analysis.

3.3.5. - Dielectric Spectroscopy

Dielectric spectroscopy (DS) measures the dielectric permittivity and dielectric losses as a function of frequency and temperature, and it can be applied to all non-conducting materials. It is a technique sensitive to dipolar species as well as localized charges in a material; it determines their strength, their kinetics and their interactions, making it a powerful technique for the electrical characterization of non-conducting or semiconducting materials in relation to their crystalline structure and microstructure [16].

Silver paste was added to the surface of the ceramics to form the electrodes. The dielectric properties of the pellets were measured with an Alpha High Resolution dielectric Analyzer novocontrol GmbH. The range of temperatures was of -30 and 170ºC with 10ºC intervals at frequencies from 10^6 to 1Hz.

3.3.6. - Ferroelectric test analyzer

Ferroelectric tests are designed to allow various measurements on ferroelectric materials to determine its main electric characteristics like: hysteresis loop, fatigue leakage, voltage breakdown, and others.

The polarization- electric fields (P-E) hysteresis loop of the ceramic pellets was measured using a standard ferro-tester (Radiant EF amplifier ± 4000V). The samples were polarized perpendicular to each electro face under an electric field.

3.4. – High-Pressure Techniques

Since the introduction of diamond to generate high pressures [17] and the later invention of the diamond anvil cell (DAC) [18] high-pressure techniques has become a powerful tool in the expansion of our knowledge concerning the behavior of matter at high pressures. Indeed hydrostatic pressure is suitable to explore structure-properties connection under extreme conditions. The deformation induced on solid materials by high isostatic pressure can be of the same order of magnitude as the one induced by the thermal agitation that complicates structure refinement at high temperature. This area of study relies in the use of complementary techniques to achieve the objective of the structural characterization, phase transition, and synthesis of novel materials. In addition, the development of DAC technologies for the collection and analysis of diffraction and spectroscopy data under extreme conditions have opened new research areas of study.

A combination of Raman spectroscopy and powder X-ray diffraction have been used during this investigation to identify and structurally characterize the phase transitions of $SrTi_{1-x}Zr_xO_3$ (X= 0.7, 0.6, 0.5, 0.4, 0.3) and $KNb_{1-X}Ta_XO_3$ (X=0.9, 0.6, 0.5, 0.4) at different ranges of pressures. High-pressure Raman experiments were performed using a membrane diamond-anvil cell for all samples. Furthermore, XRD under pressure were carried out using a nutcracker DAC type for the $SrTi_{0.6}Zr_{0.4}O_3$ sample, and a

Merrill-basset DAC for $SrTi_{0.7}Zr_{0.3}O_3$, $KNb_{0.4}Ta_{0.6}O_3$ and $KNb_{0.6}Ta_{0.4}O_3$.

This part of the chapter will give brief description of the DAC components, followed by a discussion of the experimental techniques in which they have been applied.

3.4.1. - Diamond Anvil Cell

The diamond anvil cell also known as DAC is possibly one of the most known and used device in the field of high-pressure research. The principle of this device is based on placing a sample in a metallic gasket along with a pressure calibration material, and a pressure-transmitting medium between two diamond faces, which it is exposed to high pressures when a force pushes the opposed anvils together. Figure 3.7 shows a schematic representation of the DAC.

The use of diamonds allow to see the sample under study which permit to check the sample alignment and also to observe any changes that could take place during the experiment. In addition, the transparency of the diamonds to a wide range of electromagnetic spectrum permits to perform in situ spectroscopy and optical analysis. Furthermore, the low atomic number, minimal X-ray absorption, and the high degree of the quality of the gem help to reduce any interference with the sample under study.

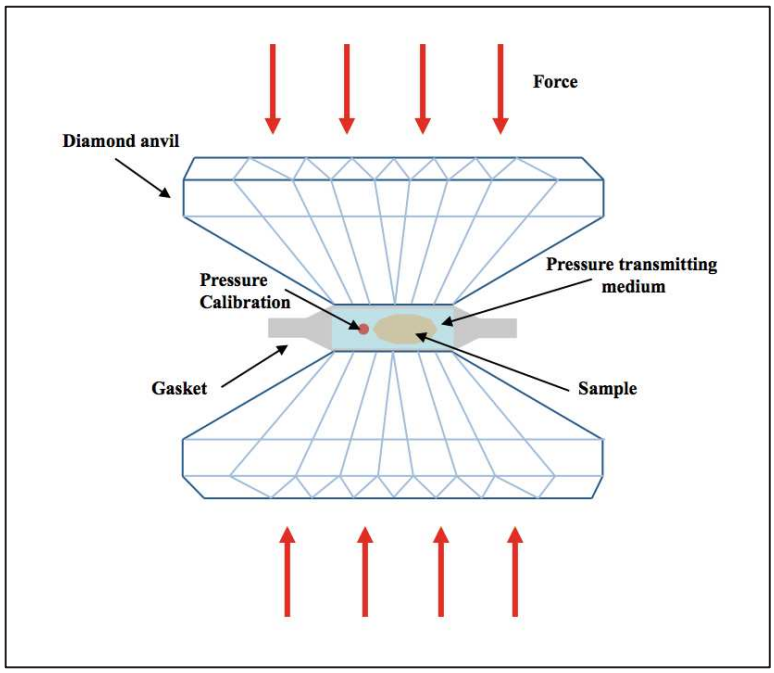

Figure 3.7. Schematic representation of the principles of the diamond

3.4.2. - Pressure Measurement

In order to determine the pressure inside the DAC a material which behavior is well known under pressure is putting along with the sample inside the chamber. In 1975 Piermarini et al. showed that the used of the laser-induced fluorescence of the ruby (Al_2O_3:Cr^{3+}) could be used as a continuous pressure sensor inside the DAC; the two main luminesce bands, R_1 and R_2, of the ruby undergo a noticeable shift as the pressure was applied. The R_1 electronic transition shows a linear dependence with pressure up to 20 GPa at ambient temperature [19]. A ruby florescence spectra obtained under hydrostatic during this investigation is shown in Figure 3.8.

In some cases, it is not possible to have an optical access to the sample chamber of the DAC, and it is needed to use a different calibrating material. In our case, we used NaCl, which have a known equation of state, and the unit cell volume is related to the pressure inside the gasket [20].

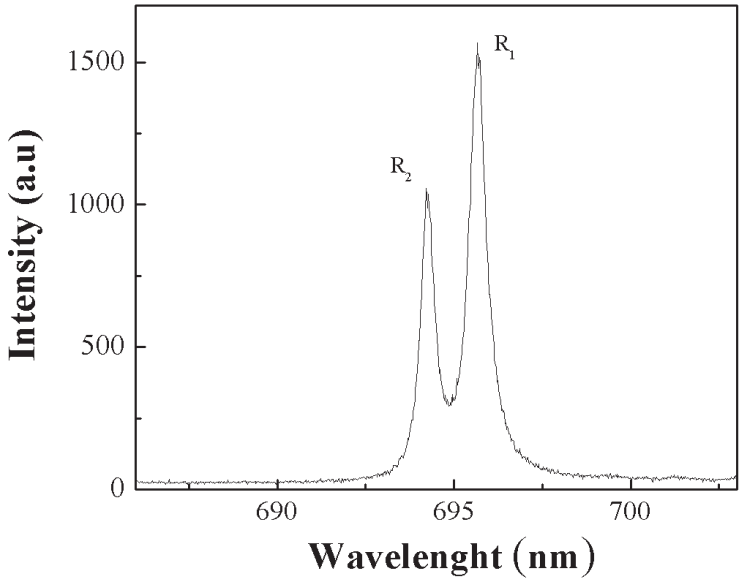

Figure 3.8. Ruby fluorescence signal at 3.63 GPa.

3.4.3. - Pressure-transmitting Medium

When doing high-pressure experiments it is needed to have a completely hydrostatic compression. This is achieved by immersing the sample in a medium that can

display a hydrostatic behavior throughout the pressure range of interest. In addition the medium should not dissolve or react with the sample under studied. Different pressure-transmitting media have been investigated to know the hydrostatic limits of them [21]. During this work, the pressure-transmitting medium was a mix of 4:1 methanol-ethanol that remains hydrostatic up to 10 GPa [21].

3.4.4. - Gasket

A gasket is prepared by pre-compressing a metal foil between two diamonds, and a small hole will be drilling through the center of the indentation that was created by diamond culets. The gasket has two basic purposes; it contains the sample along with the pressure calibrating material and the pressure medium, and provides support to the diamonds. Different types of metal can be used to prepare the gasket like steel; however for large samples volumes tungsten gasket is used because of its high mechanical strength. The preparation of the gasket is a very important step of the experiment and it has to be considered the thickness of it. In the case of the gasket is too thick the outwards force might exceed the friction between the anvils and the gasket. This will produce an expansion of the hole and there is not going to be any pressure applied to the sample, which can cause a gasket failure that could damage the diamonds. On the other hand, a thin gasket will allow to work until high pressure while having a better control at low pressures because the initially force to seal the sample chamber will be lower than by using a very thick gasket [22].

3.5. - Experimental Techniques using the Diamond-Anvil Cell

3.5.1. - Raman Spectroscopy

The scattering of light by a molecule can be understood as the promotion of it from its ground state to a virtual energy state and the subsequent relaxation of it, giving as a result the emission of a photon. Raman spectroscopy relies on inelastic scattering of monochromatic light, in where the molecule relaxes to a different vibrational ground state, resulting in an energy difference between the incident and scattered photons. Figure 3.9 shows the different phenomena that take place when a photon interacts with matter. If the initial state is the same as the final, photons will have the same energy, and this is

called Rayleigh scattering. On the other hand, if the molecule relaxes to a vibrational state of lower energy than the starting level, the scattered photon will have a higher energy than the incident one, and there will be an anti-Stokes Raman scattering. Finally, the Stokes scattering takes place when the difference between the final and initial state is less than the initial transition and the final scattered photon will have less energy than initially [23].

Raman spectroscopy is sensitive to changes in the molecular symmetry, as well as inter and intramolecular interactions variations that can take place in the sample, making it a technique very useful in the identification of phase transitions. Raman spectroscopy can be specifically applied in high-pressure studies because monochromatic light is used to perform the experiments, and any material that is transparent to visible light may be used as a sample chamber, in our case the diamond anvil cell.

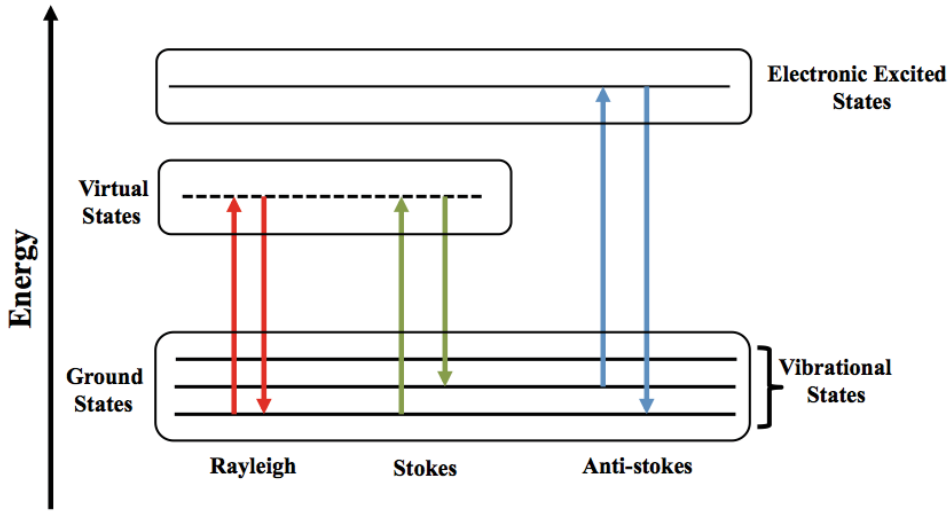

Figure 3.9. Representation of the transitions involved in Raman spectroscopy.

A gas membrane-type DAC was employed to produce high pressures on the polycrystalline samples. In this type of cell the pressure is supplied with a custom-made gas pressure system containing a stainless steel membrane in contact with the DAC which, when inflated by a compressed gas, can supply a compressive force onto the diamond anvil cell. Thenceforth, by monitoring the gas applied to the cell, the pressure can be controlled on the system. A thin stainless steel gasket, with a small pre-drilled

hole must be used to provide lateral control as the sample is compressed. A hydrostatic pressure medium has to be loaded along with the sample to assure that an isotropic stress is applied. Additionally, a calibrate pressure material has to be placed inside with the sample to know the applied pressure.

Raman measurements were performed at room temperature in a membrane-type diamond anvil cell (DAC) with diamond culets of 500 µm diameter. The homogeneous synthesized powder was placed along with a ruby sphere and a 4:1 methanol-ethanol mixture as the pressure-transmitting fluid in a pre-indented 50 µm-diameter hole drilled in the center of a 50 µm thick gasket. The pressure was determined by the ruby florescence method [24].

The Raman spectra and ruby luminescence were collected with a Horiba LabRAM aramis Raman spectrometer using an Ar^+ laser (488 nm). The exciting line was focused on the surface of sample by using a 50X objective on an Olympus microscope coupled to the spectrometer. Pressure was applied to the sample at room temperature by using a He gas inlet to the membrane until the target pressure was reached, and it was then allowed to stabilize for 15 min before collecting the data. Measurements were performed both on increasing and decreasing pressure for all the $SrTi_{1-x}Zr_xO_3$ and $KNb_{1-x}Ta_XO_3$ compounds.

Figure 3.10 shows a photograph of the DAC and the Raman spectrometer used in this investigation.

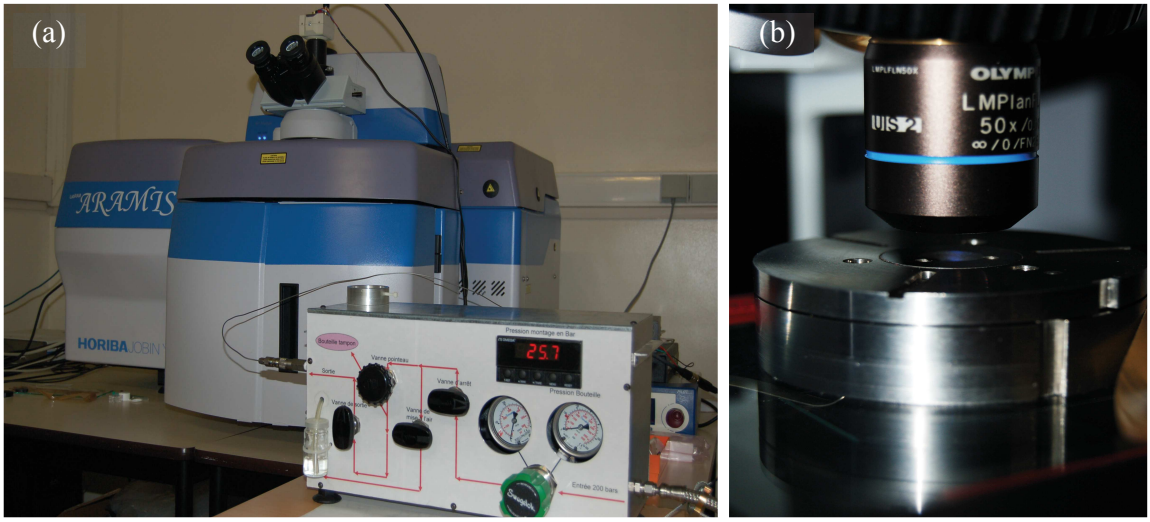

Figure 3.10. Photographs of the high-pressure Raman setup: (a) Raman spectrometer next to the He pressure controller and (b) the gas member DAC with a 50X objective.

3.5.2. - High-Pressure X-ray Powder Diffraction

X-ray diffraction is the method that allows determining a crystal structure and the atomic positions within a crystalline material, definite as a three-dimensional array of identical unit cells with long-range order and translational symmetry. The wavelength of the X-ray radiation is comparable with interatomic separations, typically of the order of few Angstroms. Therefore the interference of X-rays scattered by different atomic planes within the lattice will give as a result a diffraction pattern, from it will be possible to determine the relative atomic positions in the structure of the samples under study [11].

A powder diffraction pattern can be described as a plot of diffraction intensities (I_{obs}) against the scattering angle (2θ). The Rietveld refinement is based on the least-squares refinement method between a calculated diffractogram and a generated one. The principle is to refine the structural parameters as to minimize the difference between the calculated and observed intensities (I_{obs} vs I_{calc}). The quality of the structural refinement depends on two parameters, the weighted R-factor (R_p) that indicates the agreement between the crystallographic model and the experimental data, and the chi squared (χ^2) which represents the goodness of fit, a quantity commonly used to check whether any given data are well described by some postulated function, χ^2 starts with a large value and decreases as the model becomes closer in agreement with the obtained data [25]. In addition there is another method in where it is not necessary to know the structural model and it is called Le Bail method or profile matching. In this method the observed intensities are equal to the calculated ones and the unit cell, background and peak profile are refined [26]. In this work, Le Bail analyses of the various powder diffraction patterns were carried out using the Fullprof software [12].

The high-pressure X-ray powder diffractions were performed in order to determine any possible phases transitions with pressure that were observed by high Pressure Raman spectroscopy studies that were carried out in this investigation.

3.5.3. - Nutcracker-type Diamond Anvil Cell

A nutcracker-type DAC was used to carry out the high-pressure XRD

experiments for $SrTi_{0.6}Zr_{0.4}O_3$. In this kind of DAC, the sample with the pressure-transmitting medium and the pressure calibrating material are placed between two diamonds; the gems are seated in its tabular face, resting in a close-fitting piston mechanism, which it is compressing them. The pistons are free to slide in a cylindrical way that carries the pressure-generating mechanism. The presser-plate is connected to a device, which is twisted in the block and activated by a calibrated spring, located at the upper end of the device that pushes against the piston. The force is produced by a spring, a screw compresses it manually, and it is transmitted perpendicular to the diamonds surface [27]. The experimental setup of this DAC is shown in figure 3.11.

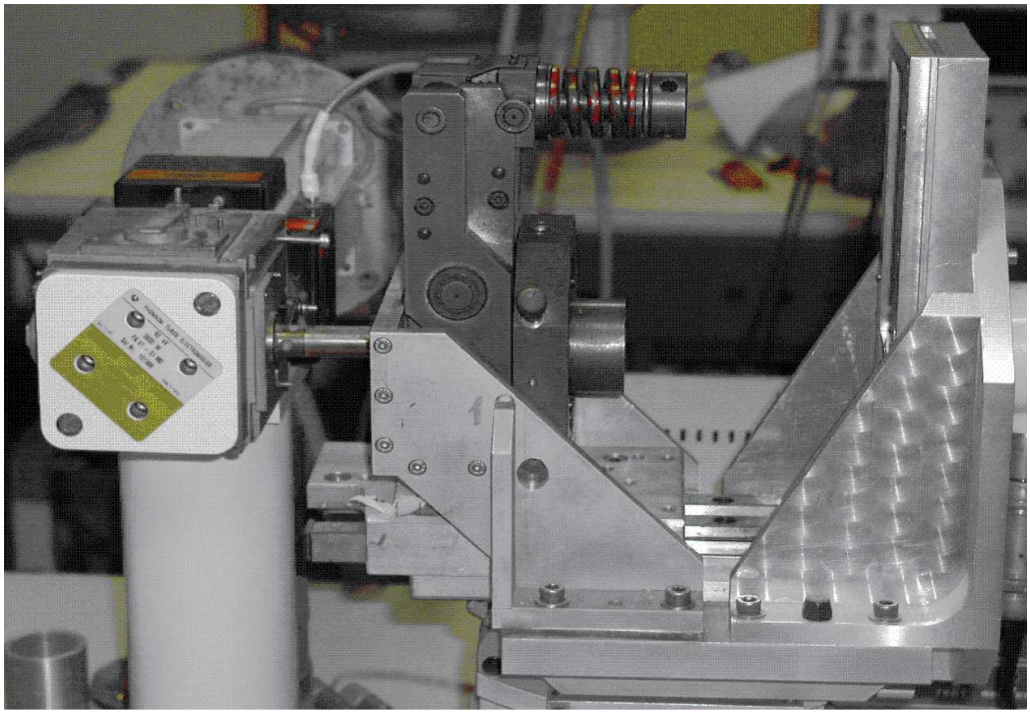

Figure 3.11. Nutcracker-type diamond anvil cell setup used for generating high-pressure in a X-ray powder diffraction apparatus.

X-ray diffraction results were obtained by the conventional angular dispersion method of Debye- Scherrer; powder samples are polycrystalline, many crystal randomly oriented, in where the diffracted beam of each order forms a cone. Arcs of the cones are intercepted by a film surrounded the machine. The diffraction imagines were integrated to produce a diagram of intensity against the diffraction angle. This is represented in

figure 3.12.

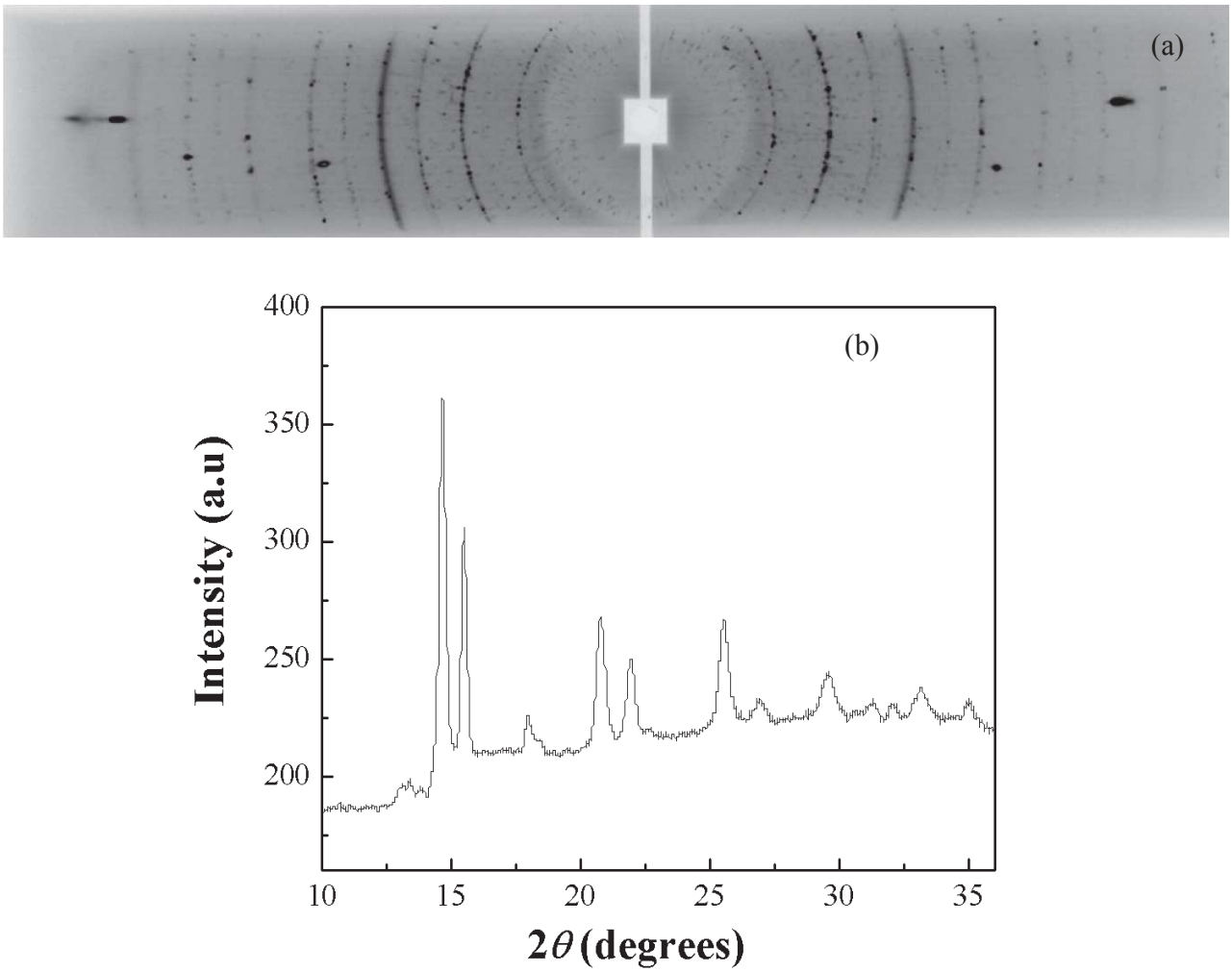

Figure 3.12. **(**a) Diffraction image arising from the spatial averaging of numerous single crystals of $SrTi_{0.6}Zr_{0.4}O_3$ at 8 GPa and (b) integrated data using the Fit2D [28] program to plot the diffraction intensity against scattering angle.

The high pressure angle-dispersive XRD experiments were performed by loading the $SrTi_{0.6}Zr_{0.4}O_3$ powder with NaCl, used as a pressure calibrate [20], and a mix of 4:1 methanol-ethanol as a pressure-transmitting medium in a 160 x 70 μm hole of a tungsten gasket. Two-dimensional XRD patterns were collected in an image plate detector, using a zirconium-filter and molybdenum radiation (K_α=0.71073 Å) from a microfocus tube (800W). The distance between the sample and the detector was of 143.69 mm and the acquisition time for each pressure was approximately 48 to 60 hours. Using the software

Fit 2D [28] it was possible to mask the intense powder diffraction rings of the W gasket and the NaCl and transform the obtained data into two-dimensional images to intensity versus 2θ profiles, and obtaining the cell parameters by using the program Fullprof [12].

The previous experiment took approximately 2 months to be finished. Later it was possible to continue the high-pressure X-ray powder diffraction tests by using a Merrill-basset DAC.

3.5.4. - Merrill-basset Diamond Anvil Cell

The Merrill-basset DAC was developed in 1974. The main achievement of this cell is the small size that has, which can be fixed it in a normal goniometer head. The diamonds are mounted on two backing plates that are sheathed in a steel body. These plates are held in the cell by small screws that permit the alignment of the diamond anvil normal to the axis of thrust. The force is then applied to the external faces of the cell by compressing the three screws that are in the steel body, and the force will be transmitted to the diamonds. It is very important to have a parallel surface when the force is applied in order to avoid any possibility of diamond failure [29]. A photograph of the Merrill-basset DAC used to carry out the experiments is shown in figure 3.13.

The high-pressure experiments using a Merrill-basset diamond anvil cell were performed for $SrTi_{0.7}Zr_{0.3}O_3$, $KNb_{0.4}Ta_{0.6}O_3$ and $KNb_{0.6}Ta_{0.4}O_3$ powders. The sample under studied was mixed with NaCl, in order to have the pressure inside the sample when each measurement was performed [20], along with a ruby [24], to control the pressure when the screws where compressed. These were placed in a 165 μm diameter hole of a tungsten gasket pre-indented to 70 μm thickness fixed to an anvil of a Merrill-Basset DAC equipped with Boehler−Almax diamonds. The DAC was mounted on a goniometer head on the Oxford Diffraction Gemini 4-circle diffractometer with a Sapphire CCD detector placed at 65.00 mm from the sample. Molybdenum radiation was used and the acquisition was performed over a 6° range in ϕ for 2 hours for each pressure to improve the powder averaging. LaB6 was used as the calibrating material. An integration of the images was performed using FIT2D [28] and the unit cell parameters were obtained performing a profile matching with the Fullprof program [12].

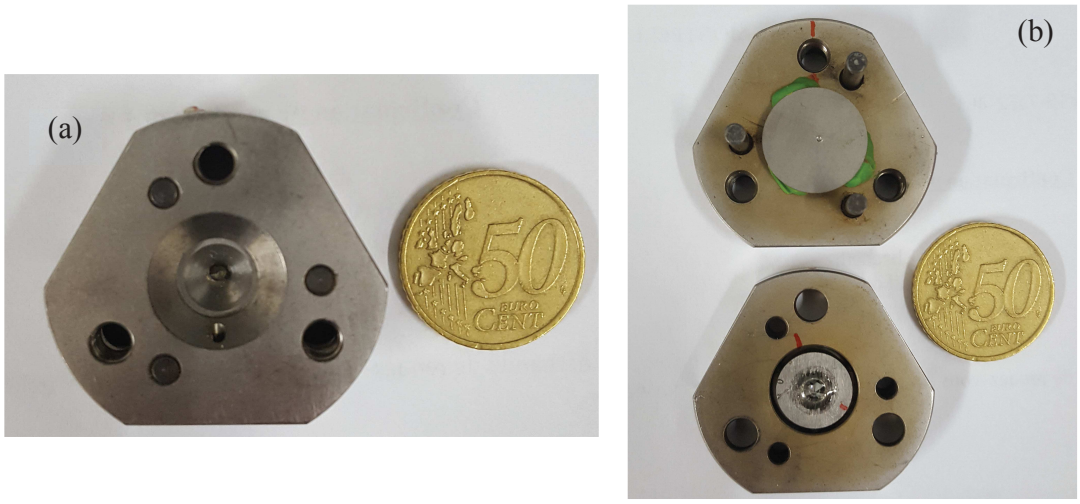

Figure 3.13. Photographs of the Merrill-basset diamond anvil cell, the coin is to compare the size of the cell. (a) Shows the plan view of the DAC and (b) is the cell open, it can be observed the 3 screws and the gasket in the upper steel body.

3.6. – Equations of State

The structural characterization of a material during its compression state allows determining the variation of its volume with pressure and in some cases with temperature. The reduction of volume when a pressure is applied is due to some modifications in the structure of the material, like changes in the interatomic distances, rotation and tilting of polyhedral in the crystal structure.

Static compression studies are generally performed at room temperature; in this case the variation of volume with pressure is called the isothermal Equation of State (EoS). The measured parameters when using an EoS are the bulk modulus (B_0), which is the ratio of the change in pressure to the fractional volume under compression, and its pressure derivatives (B'_0, B''_0) calculated at zero pressure [30].

Different approaches have been developed taking into account diverse assumptions about the behavior of dense solids; this is done because there is no fundamental thermodynamic derivation of equations of state. These assumptions will depend on how accurate the derived EoS reproduces the experimental compression

behavior of the studied sample [30]. These are the most commonly use EoS, the Vinet [31], Murnaghan [32] and Birch-Murnaghan [33] equations, and in this investigation it was only used the Birch-Murnaghan EoS.

The Birch-Murnaghan EoS makes the assumption that the strain energy applied during compression can be expressed as a Taylor series in the finite strain, $f = \frac{1}{2}\left(\left(\frac{V}{V_0}\right)^{-\frac{2}{3}} - 1\right)$, limited to the 2nd, 3rd or 4th order. The 3rd order Birch-Murnaghan EoS can be calculated according to the following equation:

$$P = \frac{3}{2}B_o\left[\left(\frac{V}{V_0}\right)^{-\frac{7}{3}} - \left(\frac{V}{V_0}\right)^{-\frac{5}{3}}\right]\left[1 + \frac{3}{4}(B_0' - 4)\left(\left(\frac{V}{V_0}\right)^{-\frac{2}{3}} - 1\right) + \frac{3}{8}\left(B_0B_0'' + (B_0' - 4)(B_0'' - 3) + \frac{35}{9}\right)\left(\left(\frac{V}{V_0}\right)^{-\frac{2}{3}} - 1\right)^2\right]$$

In this work, the parameters for the equations of state have been determined by fitting the pressure-volume data to a 3rd order Birch-Murnaghan EoS a using the program EosFit7 GUI [34].

Bibliography

[1] S. J. L. Kang, Sintering Densification, Grain Growth and Microstructure. Elsevier Butterworth-Heinemann, 2005.

[2] R. M. German, Sintering Theory and Practice. John Wiley & Sons, LTD. 1996

[3] H.E. Mgbemere, R.P. Herber, G.A. Schneider, Effect of MnO_2 on the dielectric and piezoelectric properties of alkaline niobate based lead free piezoelectric ceramics, J. Eur. Ceram. Soc. 29 (2009) 1729-1733.

[4] I. Smeltere, M. Antonova, A. Kalvane, O. Grigs, M. Livinsh, The effect of dopants on sintering and microstructure of lead-free KNN ceramics. Mater. Sci. 17 (2011) 62–64.

[5] D.H. Kim, M.R. Joung, I.T. Seo, J. Hur, J. H. Kim, B.Y. Kim, S. Nahm, Influence of sintering conditions on piezoelectric properties of $KNbO_3$ ceramics. J. Eur. Ceram. Soc. 34 (2014) 4193-4200

[6] K. Chen, J. Zhou, F. Zhang, X. Zhang, C. Li, L. An, Screening Sintering Aids for $(K_{0.5}Na_{0.5})NbO_3$ Ceramics, J. Am. Ceram. Soc. 98 (2015) 1698–1701

[7] Q. Hu, H. Du, W. Feng, C. Chen, Y. Huang, Studying the roles of Cu and Sb in $K_{0.48}Na_{0.52}NbO_3$ lead-free piezoelectric ceramics, J. Alloys Compd. 640 (2015) 327-334.

[8] K. Chen, F. Zhang, J. Zhou, X. Zhang, C. Li, L. An, Effect of borax addition on sintering and electrical properties of $(K_{0.5}Na_{0.5})NbO_3$ lead-free piezoceramics, Ceram. Int. 41 (2015) 10232-10236.

[9] G.B.P. Ferreira, J.F. da Silva Jr, R.M. do Nascimento, U. Gomes, A. Martinelli, Two-Step Sintering Applied to Ceramics, in: Arunachalam Lakshmanan (Ed.), Sintering of Ceramics - New Emerging Techniques, InTech (2012).

[10] M. Suárez, A. Fernández, J.L. Menéndez, R. Torrecillas, H.U. Kessel, J. Hennicke, R. Kirchner, T. Kesse, Challenges and Opportunities for Spark Plasma Sintering: A Key Technology for a New Generation of Materials, in: Burcu Ertuğ (Ed.), Sintering applications, InTech (2013).

[11] W. Massa, Crystal structure determination (2nd ed.), Springer, Berlin (2004).

[12] J. Rodriguez-Carvajal, Magnetic structure determination from powder diffraction using the program FullProf, in:, H. Morawiec, D. Stróz (Eds.) Applied Crystallography

Proceedings of the XVIII Conference, World Scientific, 200, 30− 36.

[13] Standard Test Methods for Apparent Porosity, Water Absorption, Apparent Specific Gravity and Bulk Density of Burned Refractory Brick and Shapes by Boiling Water. Annual Book of ASTM Standards, C20-00 (2005).

[14] G.E. Lloyd, Atomic number and crystallographic contrast images with the SEM: a review of backscattered electron techniques. Mineral mag. 51 (1987) 3-19.

[15] T. Maitland, S. Sitzman, Electron Backscatter Diffraction (EBSD) Technique and Materials Characterization Examples, in: W, Zhou, Z. L. Wang (Eds.) Scanning Microscopy for Nanotechnology, Springer, New York (2007).

[16] F. Kremer, A. Schönhals, Broadband dielectric spectroscopy (1st ed.). Springer, Berlin (2003).

[17] A.W. Lawson, T.Y. Tang, A diamond bomb for obtaining powder pictures at high pressures, Rev. Sci. Instrum. 21 (1950) 815.

[18] C.E. Weir, E.R. Lippincott, A.V. Valkenburg, E.N. Bunting, Infrared studies in the 1-to 15-micron region to 30,000 atmospheres. J. Res. Natl. Bur. Stand 63 (1959).

[19] G.J. Piermarini, S. Block, J.D. Barnett, R.A. Forman, Calibration of the pressure dependence of the *R*1 ruby fluorescence line to 195 kbarJ. Appl. Phys. 46 (1975) 2774.

[20] D.L. Decker High−Pressure Equation of State for NaCl, KCl, and CsCl J. Appl. Phys. 42 (19710) 3239.

[21] R.J. Angel, M. Bujak, J. Zhao, G.D. Gatta, S.D. Jacobsen, Effective hydrostatic limits of pressure media for high-pressure crystallographic studies, J. Appl. Crystallogr. 40 (2007) 26-32

[22] D.J. Dunstan, Theory of the gasket in diamond anvil high pressures cells, Rev. Sci. Instrum. 60 (1989) 3789

[23] E.B. Wilson, J.C. Decius, P.C. Cross, Molecular vibrations: The theory of infrared and Raman vibrational spectra. McGraw-Hill, New York (1955).

[24] H. Mao, J. Xu, P. Bell Calibration of the Ruby Pressure Gauge to 800 kbar Under Quasi-Hydrostatic Conditions. J. Geophys. Res. 9 (1986) 4673-4676.

[25] H. Rietveld, A profile refinement method for nuclear and magnetic structures J. Appl. Crystallogr. 2 (1969). 65-71.

[26] A. Le Bail, H. Duroy, J.L. Fourquet, Ab-initio structure determination of $LiSbWO_6$

by X-ray powder diffraction. Mat. Res. Bull. 23 (1988) 447-452.

[27] G.J. Piermarini, High pressure X-ray crystallography with the diamond cell at NIST/NBS. J. Res. Natl. Inst. Stand. Technol. 106 (2001) 889–920.

[28] A.P. Hammersley, S.O. Svensson, M. Hanfland, A.N. Fitch, D. Häusermann, Two-Dimensional Detector Software: From Real Detector to idealized Image or Two-Theta Scan. High Pressure res. 14 (996) 235-248.

[29] L. Merrill, W.A. Bassett, Miniature diamond anvil pressure cell for single crystal X-ray diffraction studies. Rev. Sci. Instrum. 45 (1974) 290.

[30] O. L. Anderson, Equations of state of solids for geophysics and ceramic science. Oxford University Press, New York (1995).

[31] P. Vinet, J. Ferrante, J.R. Smith, J.H. Rose, A universal equation of state for solids. J. Phys. C: Solid State Phys. 19 (1986) L467-L473

[32] F.D. Murnaghan, Finite Deformations of an Elastic Solid. Am. J. Math. 59 (1937) 235-260

[33] F. Birch, Finite Elastic Strain of Cubic Crystals. Phys. Rev. 71 (1947) 809.

[34] J. Gonzalez-Platas, M. Alvaro, F. Nestola, R.J. Angel, EosFit7-GUI: A new GUI tool for equation of state calculations, analyses and teaching. J. Appl. Crystallogr. Submitted (2016).

CHAPTER IV

HIGH-PRESSURE STUDY OF TWO LEAD-FREE PEROVSKITE MATERIALS: $SrTi_{1-x}Zr_xO_3$ AND $KNb_{1-x}Ta_xO_3$

A constant trend of device miniaturization, like the use of thin films on today's technology, has made essential to understand how the nano-scale properties deviate from the bulk ones. It is known that the difference of the thermal expansion coefficients and the lattice parameters between the films and the substrates induce stress in the thin film and this might produce changes on its properties.

In the last years, there has been an enormous progress in understanding the different phase transitions on ferroelectric materials depending of its chemical composition or temperature. The use of pressure for investigating ABO_3 perovskites materials has been less common, however, with the development of diamond anvil cells it has been possible to study phase transitions induced by pressure, and to better understand the behavior under pressure of materials at the nano-scale.

It has been reported that $SrTi_{1-x}Zr_xO_3$ (STZ) have phase transitions induced by temperature and composition [1-2]. Moreover, high-pressure experiments have only been performed on the end member of STZ, $SrTiO_3$ and $SrZrO_3$ [3,4]. On the other hand, $KNb_{1-x}Ta_xO_3$ (KNT) solid solutions have phase transitions as function of temperature and composition [5,6]. In addition, high-pressure experiments have been reported only on the rich part of Nb on the $KNbO_3$-$KTaO_3$ system [7].

We carried out high-pressure Raman scattering and X-Ray diffraction experiments on $Sr(Ti_{0.6}Zr_{0.4})O_3$ and $KNb_{1-x}Ta_xO_3$ powders. The studies were performed at room temperature from room pressure and up to 10 GPa, and the aim of this part of the dissertation is to study the potential phase transitions induced by a hydrostatic pressure in these solid solutions.

4.1. - Phase Transformation in $SrTi_{1-x}Zr_xO_3$: A High-pressure Raman and X-ray Diffraction Study

We have experimentally investigated the phase transition induced by pressure in $SrTi_{1-x}Zr_xO_3$ (STZ) polycrystalline sample. We will first present the structural

characterization, followed by the studies under high-pressure that we carried out by means of Raman spectroscopy and X-ray diffraction (XRD).

4.1.1. - X-ray Powder Diffraction

Different calcination processes were performed in order to obtain well-crystallized and phase-pure powders without residual of $SrZrO_3$ (SZ) and $SrTiO_3$ (ST) end-member phases. A two-stage calcinations process was used to obtain highly crystallized materials, as it was described in Section 3.1.1. The corresponding X-ray diffraction patterns are shown in figure 4.1. The results confirm the formation of single-phase perovskites materials without any residual phases detectable by XRD. As already discussed by Bera et al. [8], the STZ solid solution is formed through solid state reaction from the mixture of $SrCO_3$, TiO_2 and ZrO_2 via the formation of ST and SZ phases separately in the system (step 1) and the solid state reaction of ST and SZ to form the solid solution (step 2).

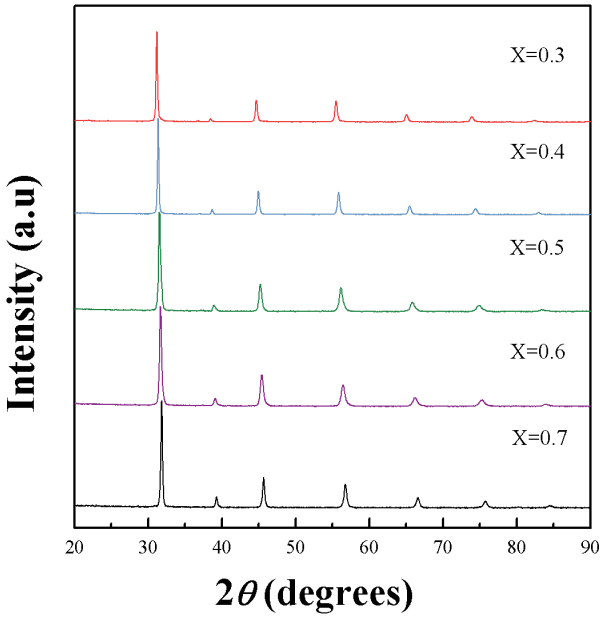

Figure 4.1. X-Ray Diffraction patterns of $SrTi_{1-x}Zr_xO_3$ powders. It can be seen that peaks are shifted to lower angles as the amount of Zr decreases, which is due to an increase of the cell volume.

It has been reported that $SrTi_{1-x}Zr_xO_3$ (x=0.3, 0.4, 0.5) samples have a tetragonal symmetry, with the space group *I4/mcm* [2,9]. Moreover, $STi_{0.4}Zr_{0.6}O_3$ has an

orthorhombic centrosymmetric structure (*Imma)* [1] and $STi_{0.3}Zr_{0.7}O_3$ presents as well an orthorhombic structure with lower symmetry (*Pnma*) [9]. It is known that the transition from cubic (ST) to tetragonal and orthorhombic (Ti-rich STZ) structures involves a small displacement of oxygen atoms associated with the insertion of Zr^{4+} in the lattice (Zr^{4+} ions are bigger than Ti^{4+} ions). This should be characterized in the XRD spectra by the splitting of the (112) peak around 55° in the cubic cell into (321) and (240) peaks for the tetragonal structure and into (321), (240) and (123) for the orthorhombic one. However, the splitting of Bragg peaks related with the motion of the oxygen atoms is barely perceptible unless high-resolution diffraction instruments are used, and in our case, we could not observe the peaks splitting.

A Le Bail analysis was performed in order to determine the cell parameters of the studied compounds. The results obtained are in good agreement with the ones previously reported at room temperature and room pressure [2]. These results are shown in table 4.1. After obtaining the single phase of the compounds, it was continue to carry out the characterization of the samples at high pressure.

Table 4.1. Details of lattice parameters from the XRD patterns obtained in this studied for $SrTi_{1-x}Zr_xO_3$ and the one reported by Parida et al [2].

Composition	Space Group	*a* (Å)	*b*(Å)	*c* (Å)	χ^2
$SrTi_{0.7}Zr_{0.3}O_3$	*I4/mcm*	5.615	5.615	7.939	1.89
Parida et al		5.621	5.621	7.937	-
$SrTi_{0.6}Zr_{0.4}O_3$	*I4/mcm*	5.656	5.656	7.971	2.46
Parida et al		5.631	5.631	7.933	-
$SrTi_{0.5}Zr_{0.5}O_3$	*I4/mcm*	5.685	5.685	7.994	2.77
Parida et al		5.678	5.678	7.998	-
$SrTi_{0.4}Zr_{0.6}O_3$	*Imma*	5.695	5.714	8.054	2.63
$SrTi_{0.3}Zr_{0.7}O_3$	*Pnma*	5.727	5.739	8.105	2.83
Parida et al.	*Pnma*	5.709	5.725	8.102	-

4.1.2. - In-situ Raman Spectroscopy at High Pressure for $SrTi_{1-x}Zr_xO_3$ Samples

An unpolarized Raman scattering study was carried out from standard pressure up to 16 GPa on both compression and decompression for $SrTi_{1-x}Zr_xO_3$ polycrystalline

samples, Figure 4.2 (a and b). We observe a number of sharp peaks, and some broad features between 180 and 300 cm^{-1}, and two other broad bands around 500 and 800 cm^{-1} in those Raman spectra. These results are similar to the spectra obtained by Parida [2] as function of composition. Titanate crystals vibrations can be anharmonic and some times the first order Raman modes could be relatively broad. In addition, in some cases the second order Raman scattering modes may be rather strong, and this can make difficult to differentiate first and second order Raman active modes [10]. The broadening of the bands around 180-300 cm^{-1}, 500 and 800 cm^{-1} might be due to second order Raman scattering, based on a comparison with the second-order spectrum of cubic $SrTiO_3$ or a coupling of different modes [2], only sharp peaks can be taking as first-order Raman bands. After releasing the pressure (fig. 4.2-b), samples recover their initial state, indicating that the changes induced by pressure are reversible without any "relaxing" phenomena.

As it was described before, $SrTi_{0.7}Zr_{0.3}O_3$ (ST70Z30), $SrTi_{0.6}Zr_{0.4}O_3$ (ST60Z40) and $SrTi_{0.5}Zr_{0.5}O_3$ (ST50Z50) are tetragonal with space group *I4/mcm*. The symmetry analysis of the Raman active modes of this phase at room temperature and atmospheric pressure has been reported previously and is characterized by seven Raman active modes ($A_{1g} + B_{1g} + 2B_{2g} + 3E_g$) in where the main signature of this phase is the presence of three basic modes E_g, B_{1g}, and B_{2g} [2,11-13]. The observed frequencies of Raman modes of these samples were thus tentatively assigned by comparison with those reported in the literature [13-15]. At low pressure, the peak around 150 cm^{-1} can be attributed to the E_g mode, mainly due to the motion of A-site ions in the ABO_3 perovskite cell. The broad band near 230 cm^{-1} can be tentatively identified as a coupling of the TO_2, B_{1g} and TO_3 modes, associated with the rotations of oxygen cages and the motion of B-site ions. The peaks around 430 cm^{-1} may correspond to the B_{2g}. The broad band about 505 cm^{-1} is generally associated with vibrations implying O^{2-} ions (bending or internal vibration cages) and it can be a coupling of the LO_3 and E_g modes. Finally, the presence of the LO_4 polar mode was observed about 795 cm^{-1}. No physical significance is claimed for the wide and noisy background.

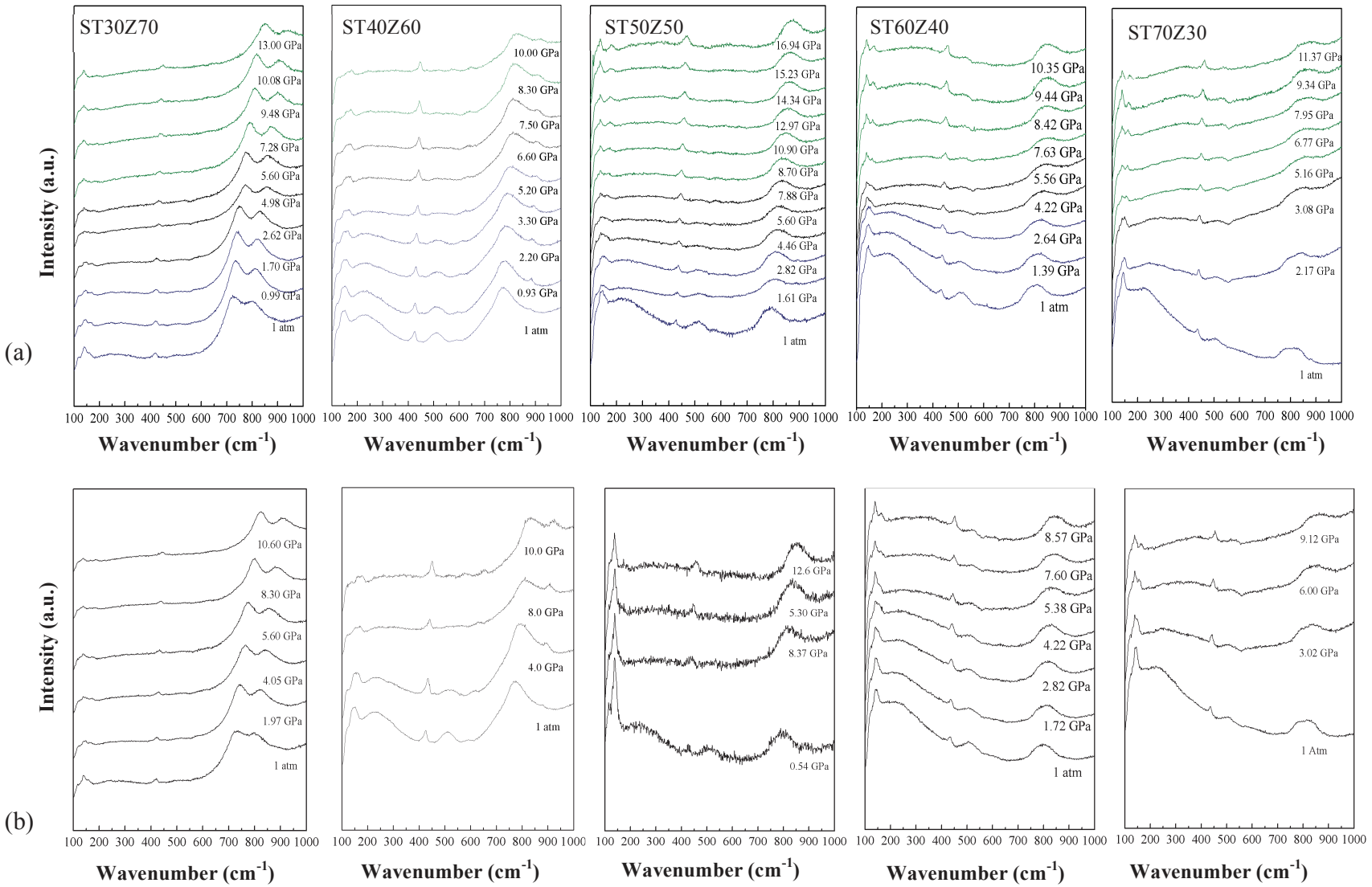

Figure 4.2. Raman spectra at room temperature of $SrTi_{1-x}Zr_xO_3$ polycrystalline samples under pressure: (a) samples upon pressuring and (b) upon decompression. The black color lines in the compression spectra are a guide at which pressure a phase transition is starting.

Hydrostatic pressure induces visible changes in the Raman spectra with a tetragonal structure. The most striking spectra features induced by pressure are (1) the removal of the overlap of the (TO_2, B_{1g} and TO_3) as the pressure is increased and (2) the intensity breakdown or weakening of the modes located at ~ 180 cm^{-1} and ~ 520 cm^{-1}. The progressive disappearances of some Raman bands and the splitting of the Eg bands into A_g and B_{2g} confirm that the tetragonal to orthorhombic (*Imma*) phase transition is taking place [15].

On the other hand $SrTi_{0.4}Zr_{0.6}O_3$ (ST40Z60) sample has an orthorhombic centrosymmetric structure (*Imma)* [1]. The group analysis for *Imma* symmetry gives twelve Raman active modes ($3A_g + 2B_{1g} + 3B_{2g} + 4B_{3g}$) [13]. At room temperature and room pressure we notice that the bands around 150 and 500 cm^{-1} are very broad. These bands are assigned as a coupling of the A_g and B_{2g} modes, which is characteristic of the orthorhombic (*Imma*) structure.

The main difference from the tetragonal spectra of (ST70Z30), (ST60Z40) and (ST50Z50) from the orthorhombic of (ST40Z60) is the weak mode at 600 cm^{-1}, which was reported by Ranson et al. [15] as an active silent mode for the *Imma* phase. New bands appear as the pressure is increased which is an indication that a phase transition to a lower symmetry phase is taking place for ST40Z60. The Raman spectrum at the highest pressure point (10GPa) has some similar characteristics with the spectrum at room temperature and pressure of $SrTi_{0.3}Zr_{0.7}O_3$ (ST30Z70), which has a lower symmetry phase with orthorhombic structure (*Pnma*). Based on this, we might assume that ST40Z60 has a phase transition from *Imma* to *Pnma* at high pressure.

As it was mentioned before, ST30Z70 has an orthorhombic structure with space group *Pnma*. The main difference between the orthorhombic *Imma* and *Pnma* comes from the doubling of the formula units per primitive unit cell (*Z*=2 to *Z*=4 in *Pnma*). This originates that the number of the Raman actives modes doubles from 12 in *Imma* to 24 in *Pnma* ($7A_g + 5B_{1g} + 7B_{2g} + 5B_{3g}$) [8,10,15]. We can observe that the Raman spectrum at room temperature and atmospheric pressure of ST30Z70 is very different from ST40Z60; the appearance of more bands confirms that both compounds have different orthorhombic structures. We can tentatively assign the modes around 150 and 180 cm^{-1} as A_g modes [8], and the band near 400 cm^{-1} can be the B_{2g} mode. This one is followed by two weak

modes around 500 and 600 cm^{-1} that probably correspond to the B_{3g} and A_g phonons, which are characteristic of this phase [9]. As the pressure is gradually increased the intensity of the modes around 150 and 500-600 cm^{-1} decreases, as well as the coupling of some of them and others bands disappeared. This provides an indication of a phase transition is happening; however, from the Raman analysis for this sample we cannot make any conclusion about which new symmetry this sample is changing, and the new phase we will be called high-pressure phase (HPI).

The phase transition zones for these compounds based on the previous analysis are reported in the following diagram:

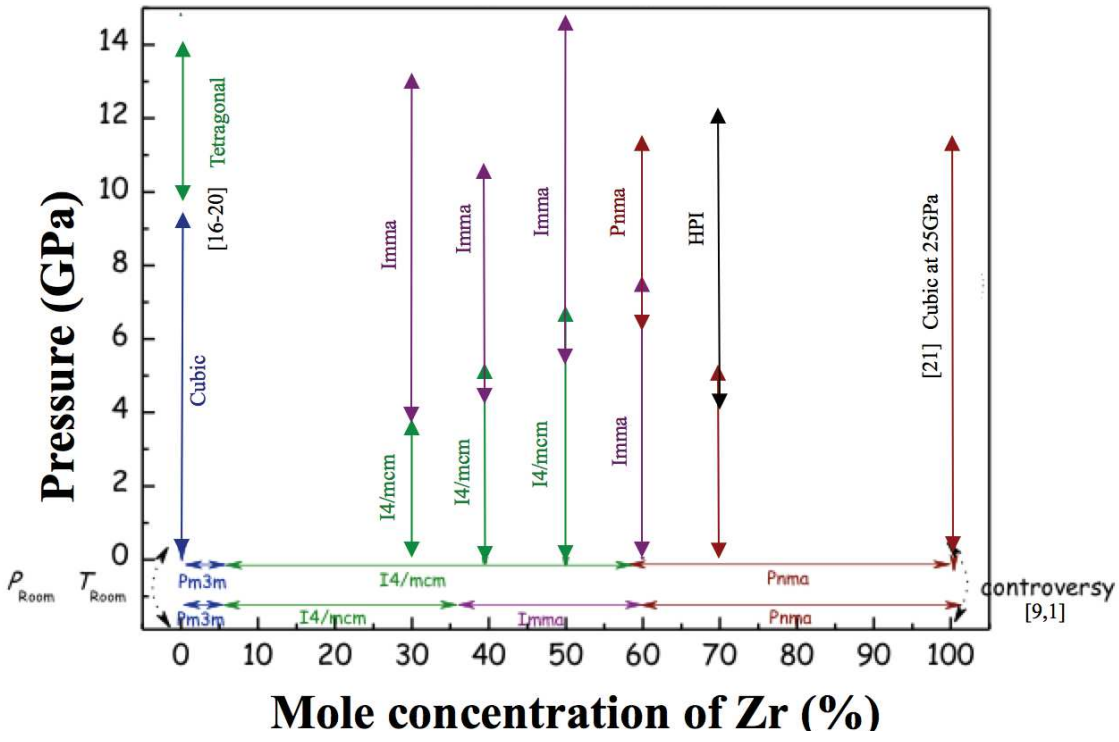

Figure 4.3. Summary of pressure-composition phase diagram for $SrTi_{1-x}Zr_xO_3$ from this work and literature.

4.1.3. - In-situ X-ray Powder Diffraction at High Pressure

The x-ray diffraction under pressure was carried out only for two samples, the tetragonal ST60Z40 and ST70Z30 samples. This was due to the time that takes to perform the experiments. A diamond anvil cell was used to carry out angle-dispersive

XRD at high pressure. The experimental procedure was explained in section 3.5.2.

The XRD data collected for ST60Z40 sample under pressure was on the decompression part of the experiment. It was not possible to collect the compression data due to the precision at setting the initial pressure in the instrument. Figure 4.4 shows the decompression spectra of ST60Z40. We can notice that the peaks shift to lower angles as the pressure decreases due to an increase of the cell volume. Due to our setup intensities, it is unreliable to do a Rietveld refinement; however, the high resolution of the detector used for the experiments allows us to do a full-profile model matching (Le Bail method) of the obtained data.

We plotted the evolution of the volume with pressure at room temperature assuming a pseudo-cubic symmetry of the solid solution. A third-order Birch-Murnaghan equation-of-state (EoS) was fit to the P-V data (Fig.4.5-a) and non-discontinuities could be observed. The first pressure derivative was fixed (B'_0) to 4 and $V_0 = 63.75$ yielding a bulk modulus of $B_0 = 202 \pm 8$ GPa. This value is lower that the one reported by Guennou et al., [19] for the high-pressure tetragonal phase of $SrTiO_3$.

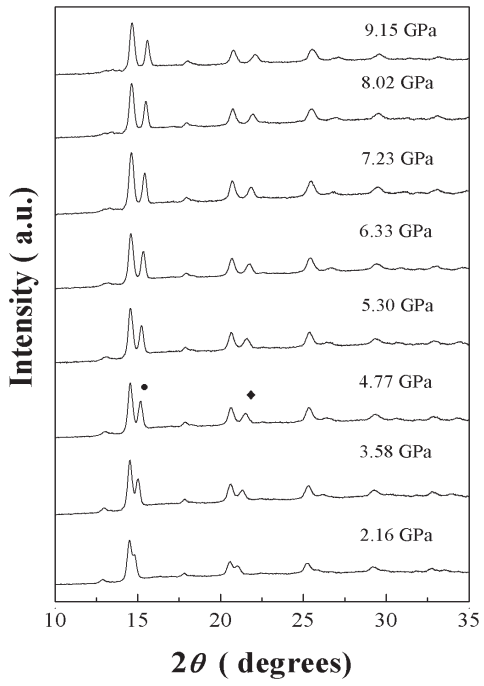

Figure 4.4. X-Ray diffraction patterns of $SrTi_{0.6}Zr_{0.4}O_3$ as a function of pressure. The diffraction lines of NaCl (•) and tungsten gasket (◆) are indicated.

Taking into account the experimental errors of the studied data and the hypothesis of a pressure-induced phase transition observed by the high-pressure Raman study that was previously performed, it is possible to consider two pressure ranges, in where there is a discontinuity around 6 GPa, as it is shown in Fig. 4.4-b. The first fit of the pressure-volume data to a third-order Birch−Murnaghan with B'_0 =7 and V_0= 63.75 Å^3 was carried out between 1 atm and 5.4 GPa yielding a bulk modulus for the low-pressure (LP) phase of $B_0^{(LP)}$ = 205 ± 17 GPa. Moreover, we performed different approximations in order to find an initial volume that would give us the best precision for the fitting at the high-pressure range, 6 to 9 GPa. The fit of the pressure-volume for this range of pressures with B'_0 constrained to 4 and V_0= 64.11 Å^3 gives us a bulk modulus for the high-pressure (HP) phase of $B_0^{(HP)}$ = 171± 58 GPa. The decrease of the compressibility must be related to the occurrence of a phase transition towards a more compressible structure, *i.e.* a lower symmetry system.

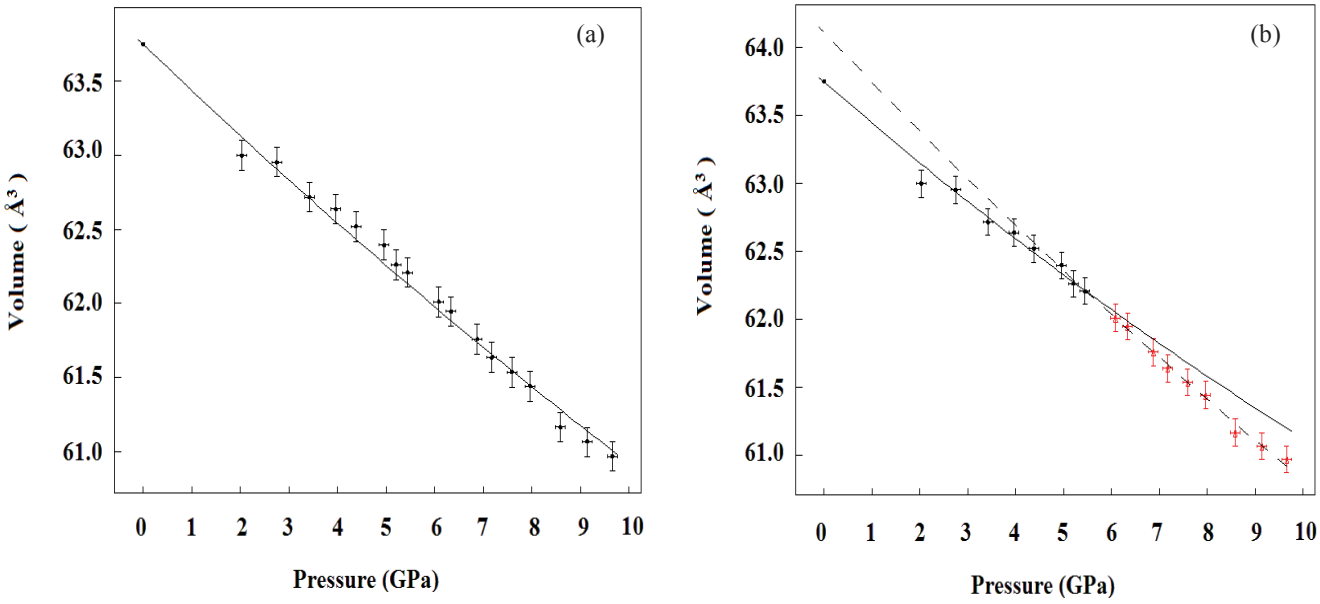

Figure 4.5. Evolution of the volume as a function of pressure at room temperature for ST60Z40. (a) The solid line represents the fit of the Birch−Murnaghan EoS with V_0=63.75 Å^3 and B'_0 = 4 giving a B_0 = 202 ± 8 GPa. (b) The solid line represents the fit of the Birch−Murnaghan EOS for the low-pressure range (L.P) with V_0=63.75Å^3 and B'_0 = 7 and the dash lines is the fit of the high-pressure range (H.P) with B'_0 = 4 and V_0=64.11 Å^3. The bulk modulus are $B_0^{(LP)}$ =205 and $B_0^{(HP)}$=171 GPa.

These results are in good agreement with the persistence of a broad scattering signature in the Raman spectra for the highest pressures that we performed (Fig. 4.6). It is important to note that a high-pressure XRD and Raman scattering studies on $SrTiO_3$ have already revealed a pressure-induced transition from cubic to tetragonal phase around 9.6 GPa, *i.e.* towards a lower symmetry system [19].

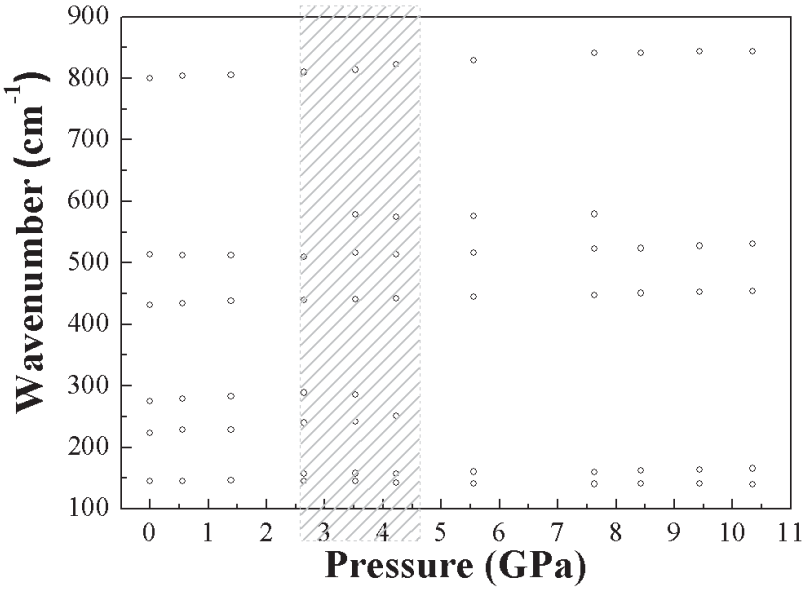

Figure 4.6. Wavenumber versus pressure for the Raman modes observed on the ST60Z40 sample. The Raman modes presented here were described on the previous section. The main signatures of possible phase transition as the pressure increases are the splitting of the E_g modes around 150 and 505 cm^{-1} into the Ag and B_{2g} modes, and the removal of the overlap modes around 200 cm^{-1}.

In order to confirm the phase transition towards a lower symmetry, we decided to study the ST70Z30 compound because this composition is not in the limit between the orthorhombic and tetragonal phases. We proceed to perform the XRD experiment under pressure of ST70Z30 by using another DAC and XRD apparatus. This allowed us to carry out the experiment in a shorter period of time, 3 days instead of 2 months. The XRD data under compression was collected up to 7.24 GPa at room temperature and is shown in figure 4.7. We can observe that as the pressure increases the peaks are shifted towards higher angle, which indicates there is a decrease of the cell volume. A profile matching was performed with the obtained results.

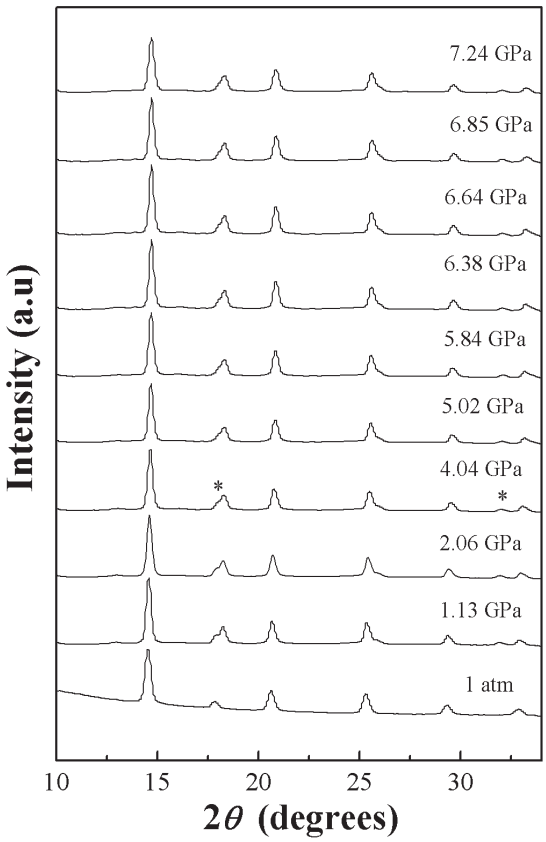

Figure 4.7. X-Ray diffraction patterns of $SrTi_{0.7}Zr_{0.3}O_3$ as a function of pressure. The diffraction lines of tungsten gasket (*) are indicated.

Assuming a pseudo-cubic symmetry of the system, the evolution of the volume as function of pressure was plotted and the results are reported in Fig. 4.8-a. No change of the slope was observed around 4 GPa. However, as it was observed on the high pressure Raman experiments that were carried out for a sample of the sample composition, a phase transition seems to occur around 4 GPa. The isothermal equation of state (EOS) was fitted to the third-order Birch-Murnaghan EOS in where the pressure derivative was constrained (B'_0) to 4 with V_0 = 62.54 Å^3 and the bulk modulus obtained was B_0 = 177 ± 11 GPa. Nevertheless, if we assume that a phase transition takes place around 4GPa, we can consider two pressures ranges (0 to 4 GPa and 4 to 7GPa) to perform the same analysis as it was carried out for the ST60Z40 sample, and the results are show in Fig. 4.8-b. The low pressure range yields a $B_0^{(LP)}$ = 168 ± 36 GPa in where we fixed the B'_0 to 4 and V_0= 62.54 Å^3. On the other hand, for the high pressure range it was obtained a $B_0^{(HP)}$ = 211 ± 89 GPa using a initial V_0= 62.22 Å^3 and a B'_0 fixed to 4.

The value that we obtained for the higher range of pressure can be seeing in two ways if we take the experimental error of the results. One possibility is that the sample undergoes a phase transition towards a higher symmetry due to the increase of the compressibility ($B_0^{(HP)}$ = 211 + 89 GPa) or that a phase transition to a lower symmetry takes place because of the decrease of the bulk modulus ($B_0^{(HP)}$ = 211 - 89 GPa). The later result will be in agreement with the high pressure Raman studied in where we observed a transition at 4 GPa to lower symmetry. Nevertheless, we cannot make any statements based on those results.

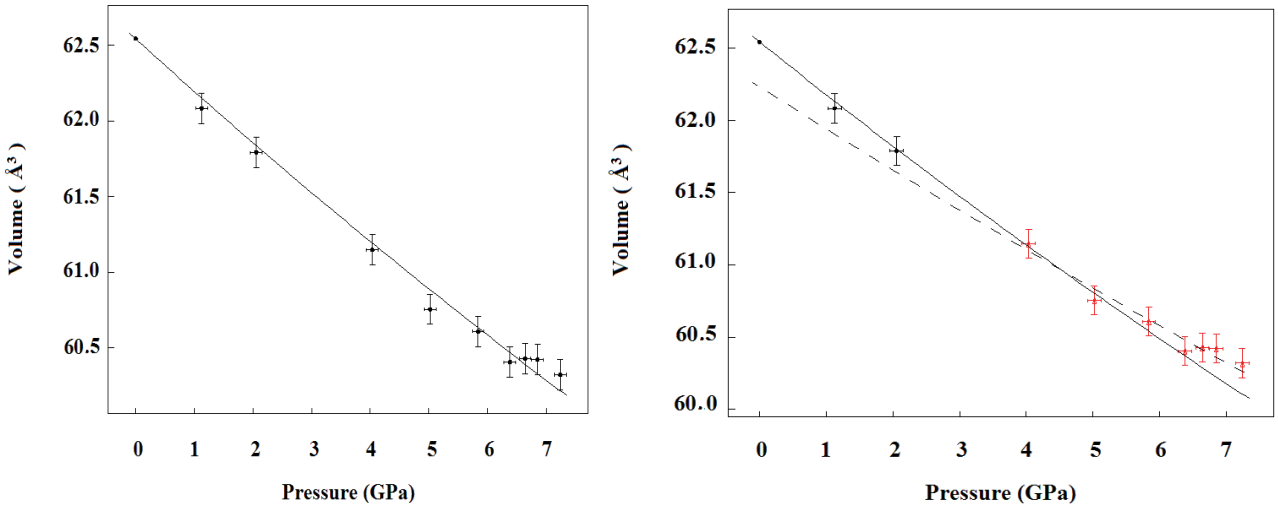

Figure 4.8. Evolution of the volume as a function of pressure at room temperature for ST70Z30. (a) The solid curve is the fit of the Birch−Murnaghan EOS with V_0=62.54 Å^3 and B'_0 = 4 yielding a B_0 = 177 ± 11 GPa. (b) The solid line represents the fit of the Birch−Murnaghan EOS for the low-pressure range (L.P) with V_0=62.54 Å^3 and B'_0 = 4 yielding a $B_0^{(LP)}$ = 168 ± 36 GPa and the dash lines is the fit of the high-pressure range (H.P) with B'_0 = 4 and V_0=62.22 Å^3 giving a $B_0^{(HP)}$= 211 ± 89 GPa

4.2. - Phase Transformation in $KNb_{1-x}Ta_xO_3$: A High-pressure Raman and X-ray Diffraction Study

Continuing with the experiments of high pressure in perovskites materials by means of Raman spectroscopy and X-ray diffraction, we studied as well the effects caused by pressure on $KNb_{1-x}Ta_xO_3$ polycrystalline samples.

4.2.1. - X-ray Powder Diffraction

Four different $KNb_{1-X}Ta_XO_3$ (X=0.9, 0.6, 0.5, 0.4) compositions were synthesized through a solid-state reaction; the experimental procedure was described in Section 3.1.2. The XRD patterns collected for these compositions at room temperature are shown in Figure 4.9 and it can be observed that highly crystallized materials without any second phases were obtained. It has been reported that the crystal structure of $KNb_{1-X}Ta_XO_3$ (KNT) changes according to the composition of $_X$ [6,22]. In order to know the structure and cell parameters of the samples, a Le bail analysis was performed for all the composition. We obtained for $KNb_{0.1}Ta_{0.9}O_3$ (KN10T90), the richest compound on tantalum, a cubic structure (Pm-3m). $KNb_{0.4}Ta_{0.6}O_3$ (KN40T60) has a tetragonal symmetry (*P4mm*) which was also observed by Shamim et al. [7]. In addition, $KNb_{0.5}Ta_{0.5}O_3$ (KN50T50) was studied in the orthorhombic structure with space group *Amm2*; however this composition is very close to the domain of the tetragonal symmetry in the phase diagram [6,22]. Furthermore, $KNb_{0.6}Ta_{0.4}O_3$ (KN60T40) exhibits as well an orthorhombic structure (*Amm2)*. The lattice parameters of the studies compounds are in Table 4.3.

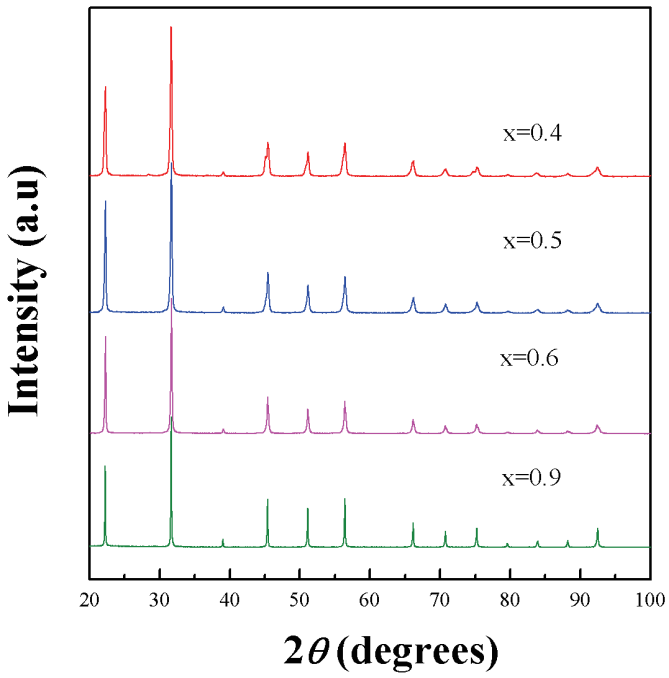

Figure 4.9. X-ray diffraction patterns of polycrystalline samples of $KNb_{1-x}Ta_xO_3$.

The volumes were calculated for a pseudo- cubic structure, we can observe a trend with the increase of the volume towards the orthorhombic phase, which it is something expected as the concentration of tantalum increases; however there is an anomaly for the KN50T50 and this could be due to the compound which is in the limit of two phases, tetragonal and orthorhombic. In addition, the volumes are very similar between them, it is about 1 % difference, other wise the substitution would not be possible and there will be the presence of second phases.

Table 4.2. Details of lattice parameters and cell volume obtained from the XRD patterns through a Le Bail analysis.

Composition	**Space Group**	***a* (Å)**	***b*(Å)**	***c* (Å)**	χ^2	**V** (Å^3)
$KNb_{0.1}Ta_{0.9}O_3$	*Pm-3m*	3.992	3.992	3.992	1.59	63.617
$KNb_{0.4}Ta_{0.6}O_3$	*P4mm*	3.993	3.993	4.002	1.11	63.808
$KNb_{0.5}Ta_{0.5}O_3$	*Amm2*	3.992	5.649	5.702	1.78	64.292
$KNb_{0.6}Ta_{0.4}O_3$	*Amm2*	3.991	5.655	5.689	1.72	64.198

After obtaining well-crystallized samples, high pressure Raman experiments were performed in order to determine at which pressure phase transitions of these compound would occur.

4.2.2. - In-situ Raman Spectroscopy at High Pressure for $KNb_{1-X}Ta_XO_3$ Samples

Raman experiments were carried out at room temperature both on increasing (up to 12 GPa) and decreasing pressure using a membrane-type diamond anvil cell (DAC) with an excited source of Ar^+ ion laser. The Raman spectra of the KNT samples under pressure are shown in figure 4.10. We observe that the main signatures of the samples are modified as function of the pressure. This can give us a direct indication that structural changes are taking place for all the studied compounds in the investigated pressure range.

Studies on temperature inducing phase transitions for similar materials have shown that the Raman spectra are manly dominated by bands related to the internal modes of the $(Nb,Ta)O_6$ octahedron [23-25]. The main features in the analyses of pressure inducing a phase transition in this work will be based on the behavior of the modes around 560 cm^{-1}, 840 cm^{-1} and the resonance-depth at 200 cm^{-1}. These Raman active modes are associated to the $(Nb,Ta)O_6$ octahedron with Oh symmetry and correspond to the Nb-O bond, O-Nb-O stretch vibration modes and O-Nb-O bend vibration modes, respectively.

The main characteristics for the different phase transitions in the KNT compounds are the following:

Orthorhombic-to-Tetragonal (O-T)

A decrease in the resonance-depth at 200 cm^{-1} and the loss of the low frequency wing of the 560 cm^{-1} mode due to a transformation of the $B_1(TO_3)$ and $B_2(TO_3)$ modes into $E(TO_3)$ are the main signatures for undergoing the O-T phase transition [25].

Tetragonal-to Cubic (T-C)

There are three main changes that characterize this phase transition: (1) the fading of the resonance depth internal vibrations of the $(Ta,Nb)O_6$ group at around 200 cm^{-1} until it almost vanishes [25], (2) the appearance of a mode near 450 cm^{-1} which is only

first-order Raman inactive, and it can be only observed as a second-order spectra in the cubic phase [23,26], (3) the disappearance of the first-order $A_1(LO_3)$ mode around 840 cm^{-1} that is forbidden in the cubic phase [23].

KN60T40 and KN50T50 samples undergo two-phase transitions as the pressure increases, O-T-C, Fig.4.10 (a). We observed a decrease in the resonance-depth and a loss of the mode at 560 cm^{-1}, which indicate that the samples are going from an orthorhombic to a tetragonal structure. The high-pressure spectra obtained in our investigation for KN60T40, KN50T50 and KN40T60 in the T-C phase transition are similar to those reported by Manlief et al. as function of temperature [23]. In our samples, there is a mode around 450 cm^{-1} that appears as the pressure increases, and it is well defined in the cubic phase. According to Raman selection rules, this mode is a second order scattering mode in the cubic structure [23,26]; this confirms a transition from tetragonal to cubic structure is taking place. As the pressure increases, the frequency of the mode around 560 cm^{-1} disappears as the phase transition from the orthorhombic to tetragonal structure approaches. In addition, the band at 450 cm^{-1} appears in the tetragonal phase till the cubic phase. The most visible change for KN40T60, KN50T50 and KN60T40 is the disappearance of the mode near 820 cm^{-1} when it reaches the cubic phase.

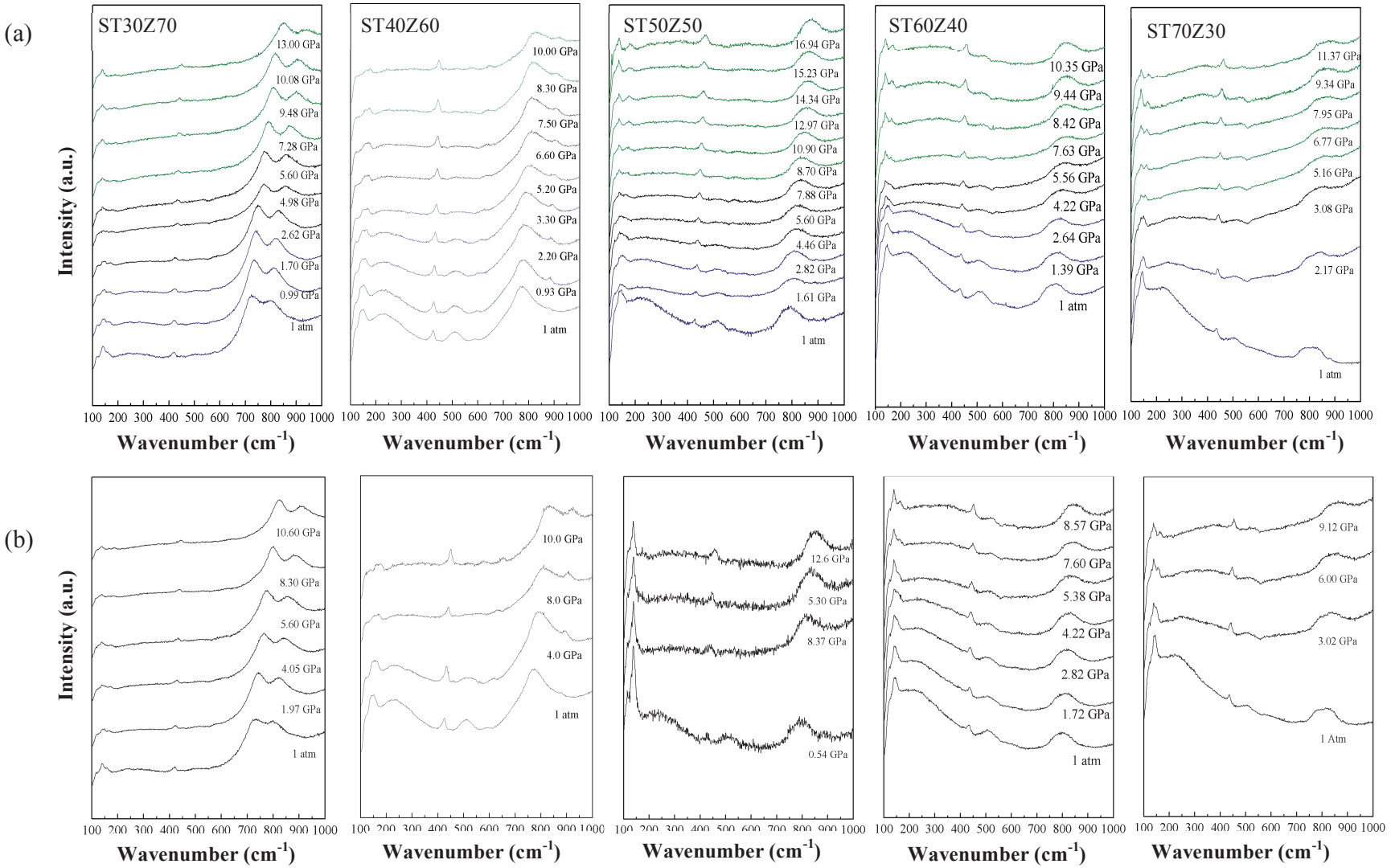

Figure 4.2. Raman spectra at room temperature of $SrTi_{1-x}Zr_xO_3$ polycrystalline samples under pressure: (a) samples upon pressuring and (b) upon decompression. The black color lines in the compression spectra are a guide at which pressure a phase transition is starting.

Moreover, the spectral deconvolution for the 500-650 cm^{-1} region of KN60T40, KN50T50 are shown in figure 4.11; it illustrates the possible identification of the orthorhombic-to-tetragonal phase transition in KN60T40 and KN50T50 trough the shoulder around 530cm^{-1}. Specifically, it can be clearly seen how as the pressure increases the $B_1(TO_3)$ and $B_2(TO_3)$ modes emerges into the $E(TO_3)$ mode and the phase transition takes place. The phase transformations might occur around 3 to 4 GPa for both KN60T40 and KN50T50 samples.

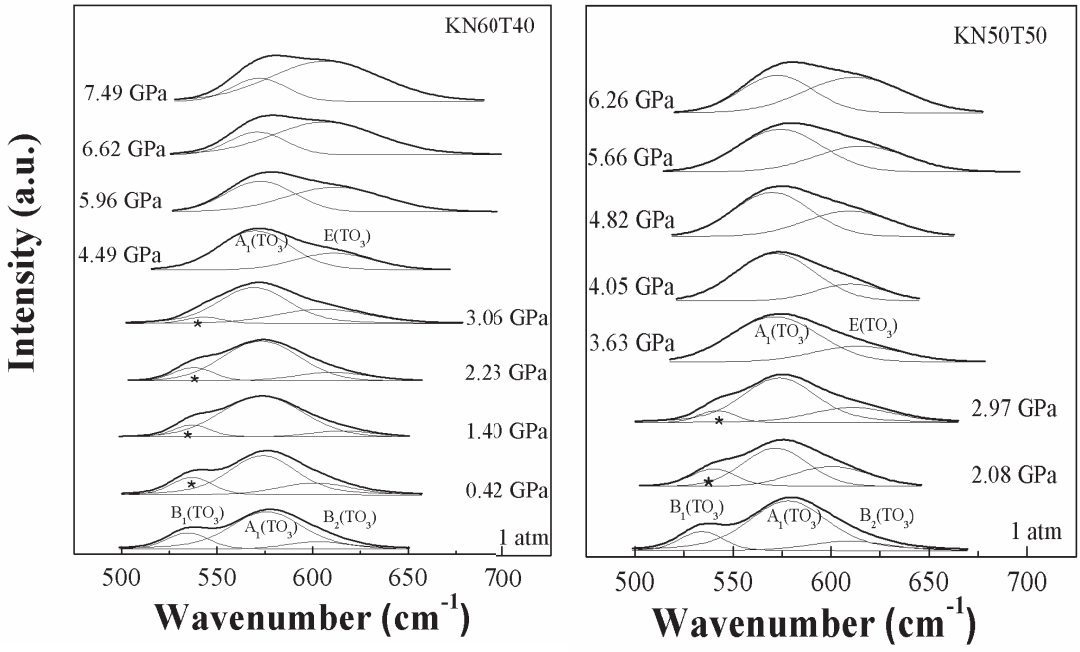

Figure 4.11. Fit of the Raman modes between 500-650 cm^{-1} for $KNb_{1-x}Ta_xO_3$ (x=0.4, 0.5) samples as a function of pressure. The spectral deconvolution illustrates the possible identification of the pressure-induced phase transitions that occur in the materials depending on the composition.

Shamim et al. performed a high pressure Raman study of KN60T40 [7]. They reported the O-T and T-C phase transitions might be around 3 and 4 GPa, respectively; however, in our work, the domain of stability of the tetragonal phase seems to be larger. In addition, we notice that as we increase the amount of tantalum the pressure decreases at the T-C phase transitions. This may be due to the atomic substitution, which can cause a similar effect to the pressure [7].

KN10T90 may be considering almost as a host lattice of $KTaO_3$ in where some of the Ta ions are randomly replaced by Nb. The Raman spectrum of this compound at room temperature and at 1atm is comparable to the Raman spectrum of $KTaO_3$ reported by Nilsen et al. [27] in where only second-order Raman spectrum can be observed. As the pressure is increased we can see that around 2 GPa most of the bands at high-frequency start to flat out and fewer bands are present. This might be an indication that the sample has a higher symmetry than the lower pressure phase. However, as the pressure continues to increase all the modes are very broad and only a very sharp soft mode is present. As we decompress the sample, Fig.4.8 (b), this one kept the same high-pressure Raman spectrum; which it may suggest us that the changes are not reversible and the sample could be amorphous above 6.55 GPa. Shen et al. reported similar results for $KNbO_3$ in where the sample goes from a high symmetry structure until finally an amorphous phase [28]. The decompression spectra for all the other samples shown in Fig.4.10 (b) are reversible.

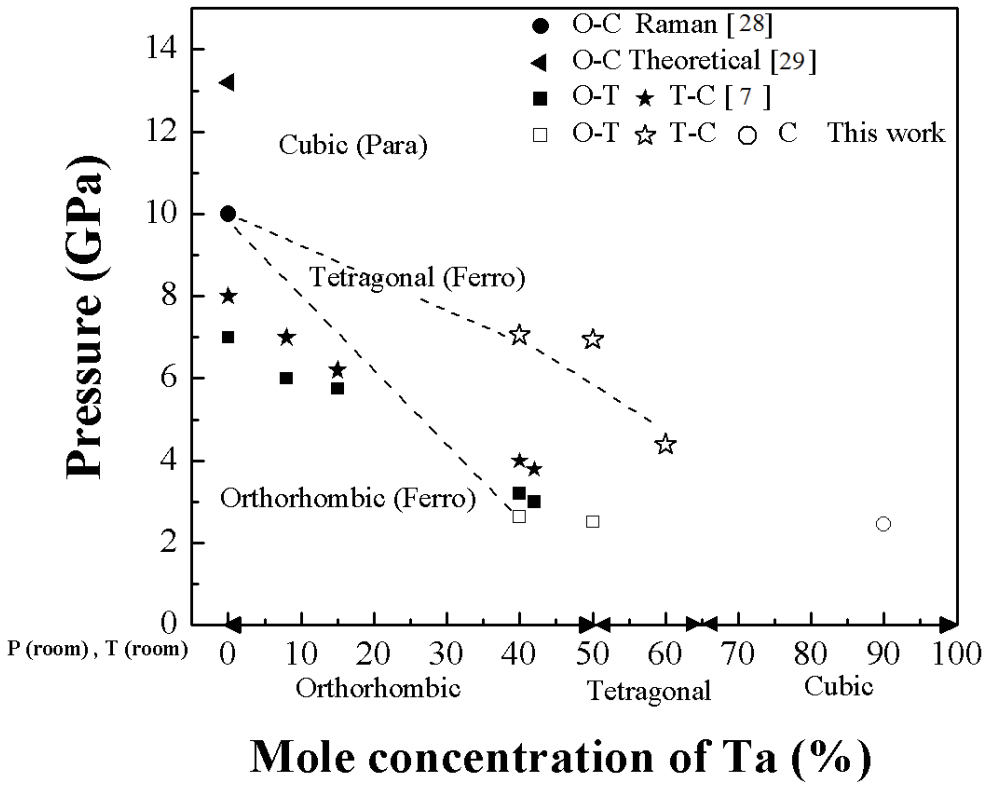

Figure 4.12. Summary of the pressure-composition phase diagram for $KNb_{1-x}Ta_xO_3$ from this work and literature. Dash lines are guides to the eyes for the points of this work.

The transitions pressures for the studied samples were assigned from the above analysis and reviewed in figure 4.12.

After obtaining the pressure range in which there may be a phase transition by means of Raman spectroscopy, we continued to perform XRD under pressure to verify the phase transitions in some of the studied samples.

4.2.3. - In-situ X-ray Powder Diffraction at High Pressure

A diamond anvil cell was used to carry out angle-dispersive XRD experiments at high pressure. Two samples were under studied, a tetragonal (KN40T60) and an orthorhombic (KN60T40). This one was done in order to study the two different structures that present the most visible changes in the Raman experiment performed before. The experimental procedure was explained in Section 3.5.2.

The XRD data collected for these samples was performed on the compression. A full-profile model refinement was obtained with the collected data. Assuming a pseudo-cubic symmetric of the samples, we plotted the evolution of the volume under pressure at room temperature, which is shown in figure 4.13. A third-order Birch-Murnaghan equation-of-state (EoS) was fit to the P-V for both samples and non-discontinuities were observed.

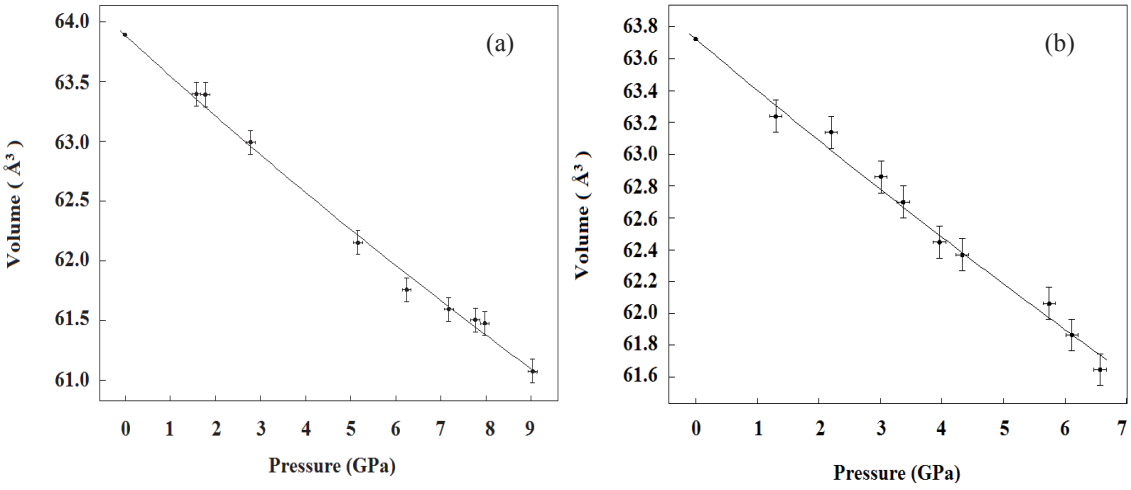

Figure 4.13. Evolution of the volume as a function of pressure at room temperature for: (a) Tetragonal (KN40T60) and (b) orthorhombic (KN60T40). The solid lines represent the fit of the Birch−Murnaghan EOS.

The first pressure derivative for both samples was fixed (B'_0) to 4 and the initial volumes were V_0^{tetra} = 63.73 Å^3 and V_0^{orth}= 63.903 Å^3 for the tetragonal and orthorhombic samples respectively. This gave as a result a bulk modulus of B_0^{tetra} = 195 ± 15 GPa and B_0^{orth} = 181 ± 10 GPa. These values indicate that one system is more compressible than the other and this is due to the symmetry of the compounds, one has a lower symmetry than the other.

It was not possible to detect any structural changes as we increased the pressure in the XRD experiments. As it was explained before, the changes in volume between the different structures are very small and they cannot be detected under the precision of the experiment. However, it was possible to observe the different structural changes at local level through the Raman experiments that were performed.

4.3. - Conclusions

Raman scattering experiments at room temperature up to 10 GPa for $SrTi_{1-x}Zr_xO_3$ and $KNb_{1-x}Ta_xO_3$ have shown the evolution of the Raman modes with pressure. The observation of the different changes on the Raman spectra provides evidence that the samples at local level might undergo pressure-induced phase transitions. The observed phase transition for $SrTi_{0.6}Zr_{0.4}O_3$ under pressure could be in agreement with the X-ray diffraction results under pressure, which exhibit a discontinuity at around 5 GPa in the volume vs. pressure behavior. The rather strong Raman spectrum obtained for this material at high pressure and the decrease of the bulk modulus between the low and high-pressure phases indicate that the high-pressure phase is distinct from the cubic high temperature paraelectric form. Moreover, the evidenced transitions in the Raman spectra for the two $KNb_{0.6}Ta_{0.4}O_3$ and $KNb_{0.4}Ta_{0.6}O_3$, and $SrTi_{0.7}Zr_{0.3}O_3$ polycrystalline samples were no observed on the XRD under pressure.

Bibliography

[1] R.E.A. McKKnight, B.J. Kennedy, Q. Zhou, M.A. Carpenter, Elastic anomalies associated with transformation sequences in perovskites: II. The strontium zirconate–titanate $Sr(Zr,Ti)O_3$ solid solution series, J. Phys.: Condens. Matter. 21 (2008) 015902.

[2] S. Parida, S. Rout, V. Subramanian, P. Barhai, Structural, microwave dielectric properties and dielectric resonator antenna studies of $Sr(Zr_xTi1_{-X})O_3$ ceramics, J. Alloys Compd. 528 (2012) 126-134.

[3] E.K.H. Salje, M. Guennou, P. Bouvier, M.A. Carpenter, J. Kreisel, High pressure ferroelectric phase transition in $SrTiO_3$, J. Phys.: Condens. Matter. 23 (2011) 275901.

[4] D. Andrault, J.P. Poirier, Evolution of the distortion of perovskites under pressure: An EXAFS study of $BaZrO_3$, $SrZrO_3$ and $CaGeO_3$, Phys. Chem. Miner. 18 (1991) 91-105.

[5] A. Reisman, E. Banks, Reactoin of the Groupe VB Pentoxides. VIII. Thermal, density and X-ray studies of the system $KNbO_3$-$NaNbO_3$ and $KNbO_3$-$KTaO_3$, J. Am. Chem. Soc. 80 (1958) 1877–1882.

[6] S. Triebwasser, Study of Ferroelectric Transitions of Solid-Solution Single Crystals of $KNbO_3$-$KTaO_3$, Phys. Rev.114 (1959) 63-70.

[7] M.M. Shamim, T. Ishidate, K. Ohi, High Pressure Raman Study of $KNbO_3$-$KTaO_3$ and $KNbO_3$-$NaNbO_3$ Mixed Crystals, J. Phys. Soc. Jpn. 72, (2003) 551-555.

[8] J. Bera, S.K. Rout, $SrTiO_3$–$SrZrO_3$ solid solution: Phase formation kinetics and mechanism through solid-oxide reaction, Mat. Res. Bull. 40 (2005) 1187-1193.

[9] T. Wong, B. Kennedy, C. Howard, B. Hunter, T. Vogt, Crystal Structures and Phase Transitions in the $SrTiO_3$-$SrZrO_3$ Solid Solution, J. Solid State Chem, 156 (2001) 255-263.

[10] P. McMillan, The Raman Spectra of Several Orthorhombic Calcium Oxide Perovskites, Phys. Chem. Miner. 16 (1988). 21-28.

[11] W.G. Nilsen, J.G. Skinner, Raman spectrum of Strontium Titanate, J. Chem. Phys. 48 (1968) 2240-2248.

[12] P. Ranson, R. Ouillon, J.P. Pinan-Lucarre, Ph. Pruzan, S.K. Mishra, R. Ranjan, D. Pandey, The various phases of the system Sr_{1-x} Ca_xTiO_3. A Raman scattering study, J. Raman Spectrosc. 36 (2005) 898–911.

[13] A. Sirenko, I. Akimov, J. Fox, A. Clark, L. Hong-Cheng, S. Weidong, X. Xi, Observation of the First-Order Raman Scattering in $SrTiO_3$ Thin Films, Phys. Rev. Lett. 82 (1999) 4500–4503.

[14] R. Ouillon, J. Pinan-Lucarre, P. Ranson, P. Pruzan, S. Mishra, R. Ranjan, D. Pandey, A Raman scattering study of the phase transitions in $SrTiO_3$ and in the mixed system $(Sr_{1-x}Ca_x)TiO_3$ at ambient pressure from T = 300 K down to 8 K, J. Phys.: Condens. Matter. 14 (2002) 2079–2092.

[15] P. Ranson, R. Ouillon, J. Pinan-Lucarre, P. Pruzan, S. Mishra, R. Ranjan, D. Pandey, The various phases of the system $Sr_{1-x}Ca_xTiO_3$—A Raman scattering study, J. Raman Spectrosc. 36 (2005) 898–911.

[16] S.A. Hayward, E. K.H. Salje, Cubic-tetragonal phase transition in SrTiO3 revisited: Landau theory and transition mechanism, Phase Transit. 68 (1999) 501–22.

[17] G.A. Samara, T. Sakudo, K. Yoshimitsu, Important Generalization Concerning the Role of Competing Forces in Displacive Phase Transitions, Phys. Rev. Lett. 35 (1975) 1767.

[18] D. Lheureux, A. Polian, M. Fischer, M. Gauthier, J.-P. Itié, Ultrasonic and brillouin scattering measurements under pressure near the structural phase transition of strontium titanate, in 2000 IEEE Int Ultrason Symp Proc. (2000) 557–560.

[19] M. Guennou, P. Bouvier, J. Kreisel, Pressure-temperature phase diagram of $SrTiO_3$ up to 53 GPa, Phys. Rev. B, 81 (2010) 054115.

[20] S.-C. Weng, R. Xu , A. H. Said, B. M. Leu, Y. Ding , H. Hong , X. Fang, M.Y. Chou, A. Bosak, P. Abbamonte, S. L. Cooper, E. Fradkin, S.-L. Chang, T.-C. Chiang, Pressure-induced antiferrodistortive phase transition in SrTiO3: Common scaling of soft-mode with pressure and temperature, EPL. 107 (2014) 36006.

[21] D. Andrault, J.P. Poirier, Evolution of the Distortion of Perovskites Under Pressure: An EXAFS Study of $BaZrO_3$, $SrZrO_3$ and $CaGeO_3$, Phys. Chem. Minerals. 18 (1991) 91-105.

[22] D. Rytz, H.J. Scheel, Crystal Growth of KTa_1-xNb_XO_3, J. Cryst. Growth 59 (1982) 468-84.

[23] S.K. Manlief, H.Y. Fan, Raman Spectrum of $KTa_{0.64}Nb_{0.36}O_3$. Phys. Rev. B. 5 (1972) 4046-4060.

[24] N.N. Zhang, R.S. Wei, J.Y. Wang, X.B. Hu, H.J. Zhang, CC. Santos, I. Guedes, Phase transition investigation by Raman spectroscopy in highly diluted KTN crystals, J. Alloys Compd. 531(2012) 14-17.

[25] A. Bartasyte, J. Kreisel, W. Peng, M. Guilloux-Viry, Temperature-dependent Raman scattering of KTa_{1-x} Nb_xO_3 thin films. Appl. Phys. Lett. 96 (2010) 262903.

[26] M.M. Rahaman, T. Imai, J. Miyazu, J. Kobayashi, S. Tsukada, M.A. Helal, Relaxor-like dynamics of ferroelectric $K(Ta_{1-x}Nb_x)O_3$ crystals probed by inelastic light scattering, J. Appl. Phys. 116 (2014) 074110.

[27] W.G. Nilsen, J.G. Skinner, Raman spectrum of Potassium Tantalate. J. Chem. Phys. 47 (1967) 1413-1418.

[28] Z. Shen, Z. P. Hu, T. C. Chong, M. H. Kuok, Pressure-induced strong mode coupling and phase transitions in $KNbO_3$, Phys. Rev. B. 52 (1995) 3976-3980.

[29] S. Li, R. Ahuja, B. Johansson, Pressure-induce phase transitions of $KNbO_3$, J.Phys.: Condens.Matter. 14 (2002) 10873-1087.

CHAPTER V

PROCESSING, CHARACTERIZATION, AND DIELECTRIC STUDIES ON $K(Nb_{0.4}Ta_{0.6})O_3$ AND $(K_xNa_{1-x})Nb_{0.6}Ta_{0.4}O_3$ CERAMICS

In recent years, potassium niobate tantalate $K(Nb_{1-x}Ta_x)O_3$ (KNT) and potassium sodium niobate $(K_{0.5}Na_{0.5})NbO_3$ (KNT) have appeared as potential environmental-friendly candidates for substituting lead-based materials which are used on today's technology as transducers and actuators [1-6]. KNT solid solutions present a perovskite-type structure, which varies at room temperature and room-pressure, from cubic to tetragonal and orthorhombic symmetry as tantalum is substituted by niobium [7]. Consequently, the ferroelectric properties of KNT, like the Curie temperature, can be adjusted by controlling the composition.

One major obstacle for technical applications of KTN and KNN ceramics is the challenge of processing these materials due to the presence of alkaline elements, which due to its low vapor pressures can evaporate at high-temperature, and as a consequence these ceramics exhibit a poor sinterability and a difficult control of the microstructure. These leave a limited number of processing techniques to produce dense ceramics with suitable dielectric, ferroelectric and piezoelectric properties.

In this chapter a comparative study using three sintering methods, sintering aids, two-step sintering (TSS) in air, and spark plasma sintering (SPS) will be discussed for $KNb_{0.4}Ta_{0.6}O_3$ (KN40T60) and $(K_xNa_{1-x})Nb_{0.6}Ta_{0.4}O_3$ (x=1.0, 0.9, 0.8, 0.7, 0.6, 0.5) ceramics. It will be focused on the influence of these sintering techniques on the morphology, density and dielectric properties of the final ceramics. We need to point out that only two compositions, $KNb_{0.4}Ta_{0.6}O_3$ and $KNb_{0.6}Ta_{0.4}O_3$ were studied during this part of the dissertation due to the non centrosymmetric structures that they have at room temperature, tetragonal and orthorhombic, respectively [7].

5.1. - Elaboration and Characterization of $KNb_{0.4}Ta_{0.6}O_3$ ceramics

The aim of this part of the chapter is to discuss the influence of three different sintering techniques, sintering aids, CuO, MnO_2, WO_3, $CuNb_2O_6$, $CuTa_2O_6$ and KF by a conventional sintering process, the use of two-step sintering, and spark plasma sintering on the physical properties of $KNb_{0.4}Ta_{0.6}O_3$ (KN40T60) ceramics.

5.1.1. - Conventional sintering

X-ray diffraction (XRD) pattern of KN40T60 powders is shown in Figure 5.1. No impurity peaks other than KN40T60 perovskite peaks were observed. A Le Bail analysis of the XRD was performed using a tetragonal structure (*P*4*mm* space group); this was previously reported for the single crystal phase diagram of $KNb_{1-x}Ta_xO_3$ [7,8]. The sample kept the same tetragonal symmetry after a conventional sintering method in air was performed to consolidate the powder.

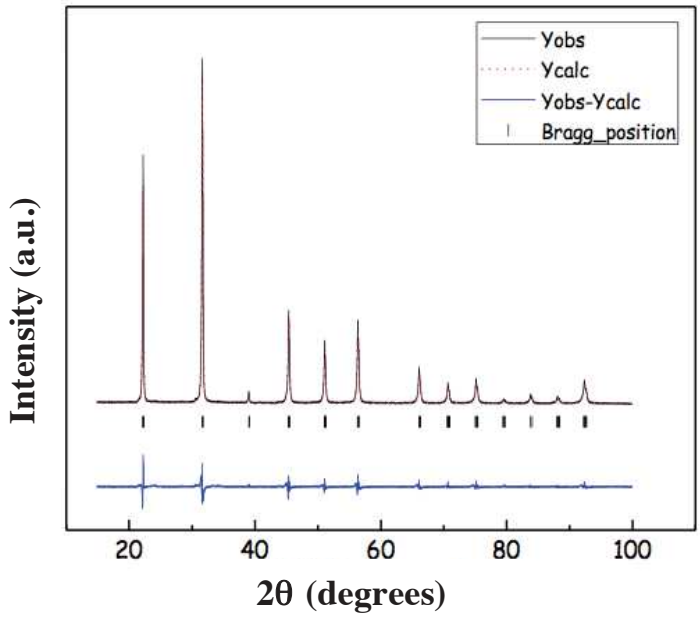

Figure 5.1. XRD pattern with the experimental and calculated profiles from the Le Bail analysis. Cell parameters are *a*=*b*= 3.99285Å and *c* =4.00169Å for the tetragonal (*P*4*mm*) structure of $KNb_{0.4}Ta_{0.6}O_3$ at room temperature and room pressure.

Complementary to the XRD, a fracture surface of the sintered pellet was observed by SEM. Figure 5.2 shows a porous microstructure consisted of grains presenting a bimodal distribution and cubic shape. EDX analysis on different regions revealed a homogeneous composition within the grains without significant changes at the grain boundaries. However, oxygen vacancies were formed and the average value of the measured Nb:Ta ratio was 0.7, which is higher than the nominal value of 0.67 for the $KNb_{0.4}Ta_{0.6}O_3$ compound. The difficulty in maintaining the exact stoichiometric ratio of Nb:Ta at the B-site in air-sintered samples has already been reported [9, 10].

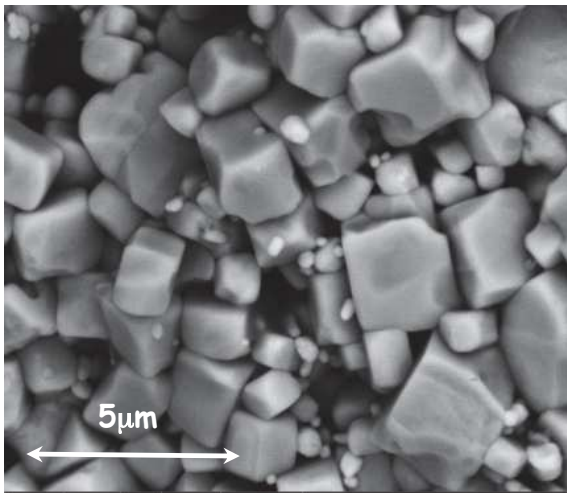

Figure 5.2. SEM micrograph of $KNb_{0.4}Ta_{0.6}O_3$ ceramic sintered in air by conventional sintering at 1150°C during 6h.

After confirming the purity and crystal structure of the air-sintered KN40T60 ceramic, dielectric measurements were performed. Figure 5.3 shows that the maximum of the dielectric constant appears around 0 °C. This value is lower compared to the Curie temperature (T_C) around 50°C for a single crystal of the same 40:60 nominal composition [7]. As it has already been reported [9-11], this difference in the T_C might be due to the fluctuations between the measured and nominal compositions of the samples but also to the presence of oxygen vacancies. Indeed for ferroelectric ceramics like $BaTiO_3$ the T_C considerably depends on the presence of oxygen vacancies, which tend to remove locally the tetragonal symmetry and the ferroelectric state leading to a reduction of T_C [12, 13]. Furthermore, the sample exhibits strong frequency dispersion in the dielectric properties and high dielectric losses, with a peak at low frequency that decays at higher temperatures, before the normal electrical conductor behavior at high temperatures occurs. This could be associated with the low density of the sample and the resultant microstructure. Indeed, the dielectric loss of ferroelectric materials is affected by two factors, intrinsic and extrinsic [14-16]. Intrinsic losses depend on the crystal structure and are due to the interaction of the phonons of the material with the applied AC electric field. [14, 15]. On the other hand, extrinsic losses are associated with imperfections in the crystal structure, *e.g.* impurities, microstructural defects, grain boundaries, porosity and

micro cracks [14-16]. In ceramics, the dielectric losses are mainly attributed to extrinsic factors due to the polycrystalline nature of the samples. In our case, we can suggest that the high dielectric losses of the studied air-sintered KN40T60 ceramic are due to the high porosity and bimodal size distribution. S.T. Penn & al. developed a model for polycrystalline ceramics in which they explained how the dielectric losses depend strongly on the pore volume with only a small degree of porosity having a marked effect on the losses [17].

Different sintering temperatures and time, as well as double-sintering processes were used to try to obtain well-densified ceramics by conventional methods. However, the relative density of the specimen was 85% of the theoretical density.

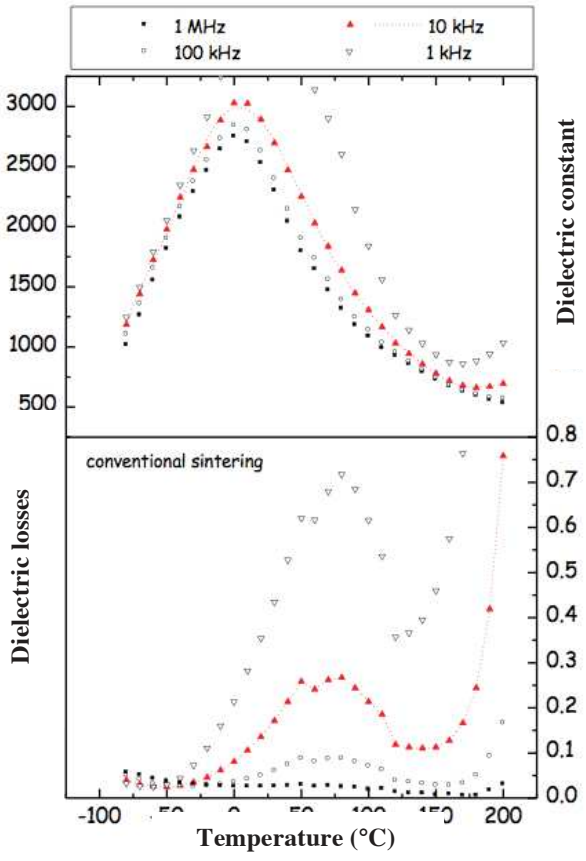

Figure 5.3. Dielectric constant and dielectric losses of $KNb_{0.4}Ta_{0.6}O_3$ ceramic sintered in air by conventional sintering as function of temperature and frequency.

5.1.2. - Effect of chemical additives on sinterability

The addition of sintering aids did not affect the crystallographic structure of the ceramics significantly unless they enter in the crystalline lattice. In all the samples, the perovskite structure is confirmed and no secondary phases were detectable by XRD (Fig. 5.4). It was not possible to distinguish for all the diffraction patterns the splitting of the (200) peak into (200) and (002) around 45 degrees. Note that these two peaks are very close to each other for pure KN40T60 ceramics, resembling a pseudocubic perovskite structure. We can suggest that the sintering aids could have diffused, to a certain extent, into the KN40T60 lattice; this explains the slight changes in the lattice parameters and c/a ratio observed for these samples as it is reported in Table 5.1. Except for WO_3, the likely partial heterovalent substitution tends to reduce the c/a ratio of the tetragonal unit cell, and therefore there could be a decrease of the Curie temperature [12].

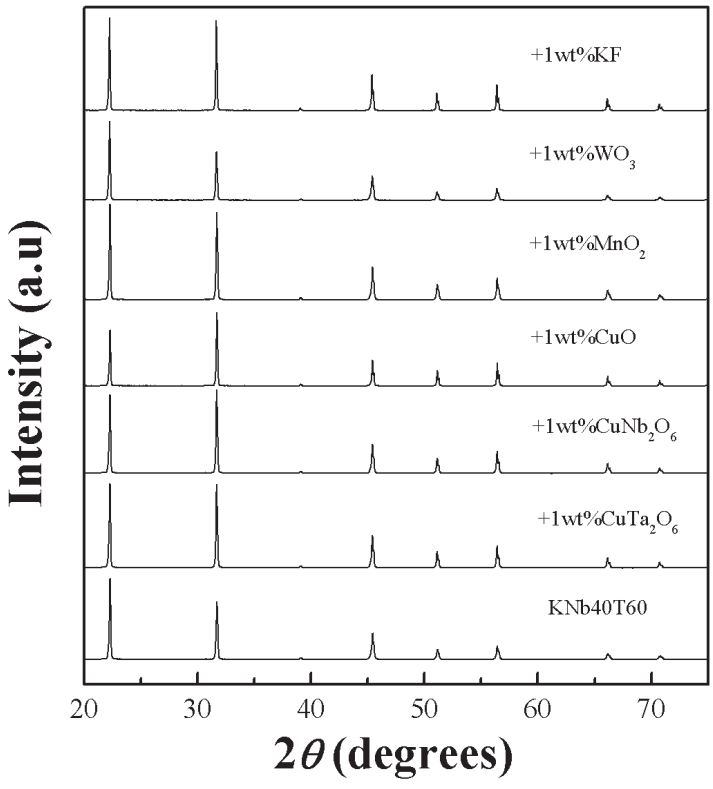

Table 5.4. X-Ray Diffraction patterns of $KNb_{0.4}Ta_{0.6}O_3$ ceramics sintering in air using different sintering aids with 1wt%.

This assumption seems to be confirmed by EDX analyses; it revealed that the compositional changes in the grains are stronger for samples prepared with sintering aids, even though the Nb:Ta ratio at the B-site approaches the stoichiometric 40:60 (0.67) ratio. Dispersions from 0.55 to 0.77 within the particles were observed whatever the sintering aid was used. However, the use of a KF showed less inhomogeneities in composition, variation of the Nb:Ta ratio from 0.60 to 0.72.

Table 5.1. Lattice parameters of $KNb_{0.4}Ta_{0.6}O_3$ (KN40T60) ceramics sintering in air using different sintering aids with 1wt% and the c/a ratio. It can be observe a decrease of the tetragonality with the different sintering aid.

	***a=b*(Å)**	***c* (Å)**	***c/a***
KN40T60	3.9923	4.0032	1.00274
+ WO_3	3.9927	4.0039	1.00282
+ MnO_2	3.9939	4.0027	1.00221
+$CuNb_2O_6$	3.9944	4.0015	1.00178
+ $CuTa_2O_6$	3.9947	4.0014	1.00167
+ CuO	3.9948	4.0002	1.00134
+ KF	3.9943	3.9995	1.00131

The microstructures of KN40T60 using different sintering aids were investigated using SEM, as shown in figure 5.5. All samples exhibit rectangular shaped grains, which is a common feature in KNT-based compounds [18-20]. Dense microstructure, 93% of the theoretical one, was formed for ceramics with 1%wt of KF and Cu-based additives, exhibiting a similar morphology consisting of well-defined particles with average grain size of 2.3 μm. However, a homogeneous porous microstructure consisting of small grains with an average grain size of 1.1 μm was obtained for samples containing WO_3 and MnO_2 whose density was lower than 90%. The addition of sintering aids could have generated the partial formation of liquid phase at the grain boundaries during the sintering process, which helped in the densification process. In our case, due to the low amount of sintering aids, it was not possible to detect by SEM the effects on the microstructure. It can be suggested that a transient liquid phase was formed during the

sintering process, with high solubility in the KNT system that led to its eventual disappearance with sintering time and/or sintering temperature.

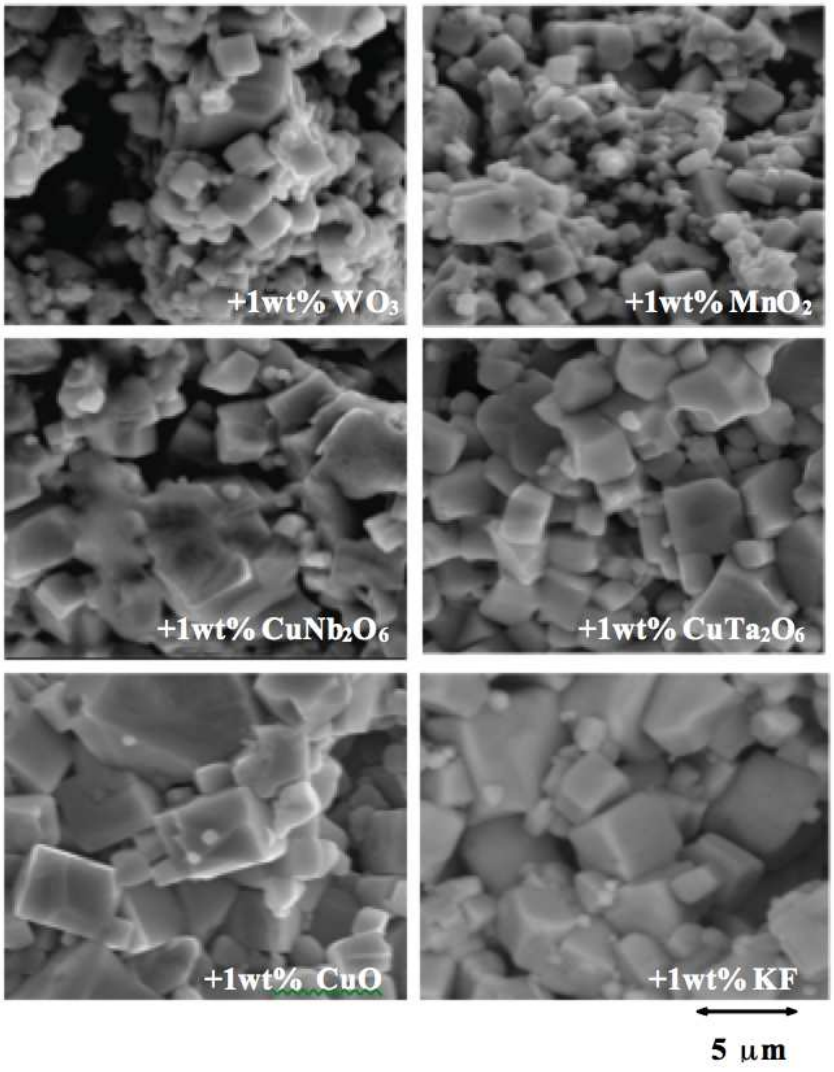

Figure 5.5. SEM micrograph of $KNb_{0.4}Ta_{0.6}O_3$ ceramics sintered in air with 1wt% sintering aids.

The temperature dependence of the dielectric properties was significantly modified depending on the sintering aids that were used, as shown in Fig. 5.6. The phase transition for all the samples is broadened suggesting the appearance of a diffuse phase transition, which is in agreement with the above-mentioned compositional dispersion within the grains. Depending on the sintering aid, the T_C was shifted to lower

temperatures (around 0°C for KF and MnO_2) to higher temperature (around 30°C for WO_3) or separated into two peaks (from -25°C to 11°C for Cu-based compounds). We can notice that KF seems as the most effective sintering aid in markedly reducing and in stabilizing the dielectric losses over a wide range of temperatures without decreasing the dielectric constant. In addition, by using KF there could be an improvement of the sintering process because K^+ might diffuse into the lattice, and this could possibly compensate the volatilization of the alkali element during the heat treatment without disturbing the overall stoichiometry of KN40T60. Moreover, the possible presence of a thin layer of potassium oxide between KN40T60 particles is also expected to reduce further volatilization of alkali elements within the KN40T60 lattice itself [21].

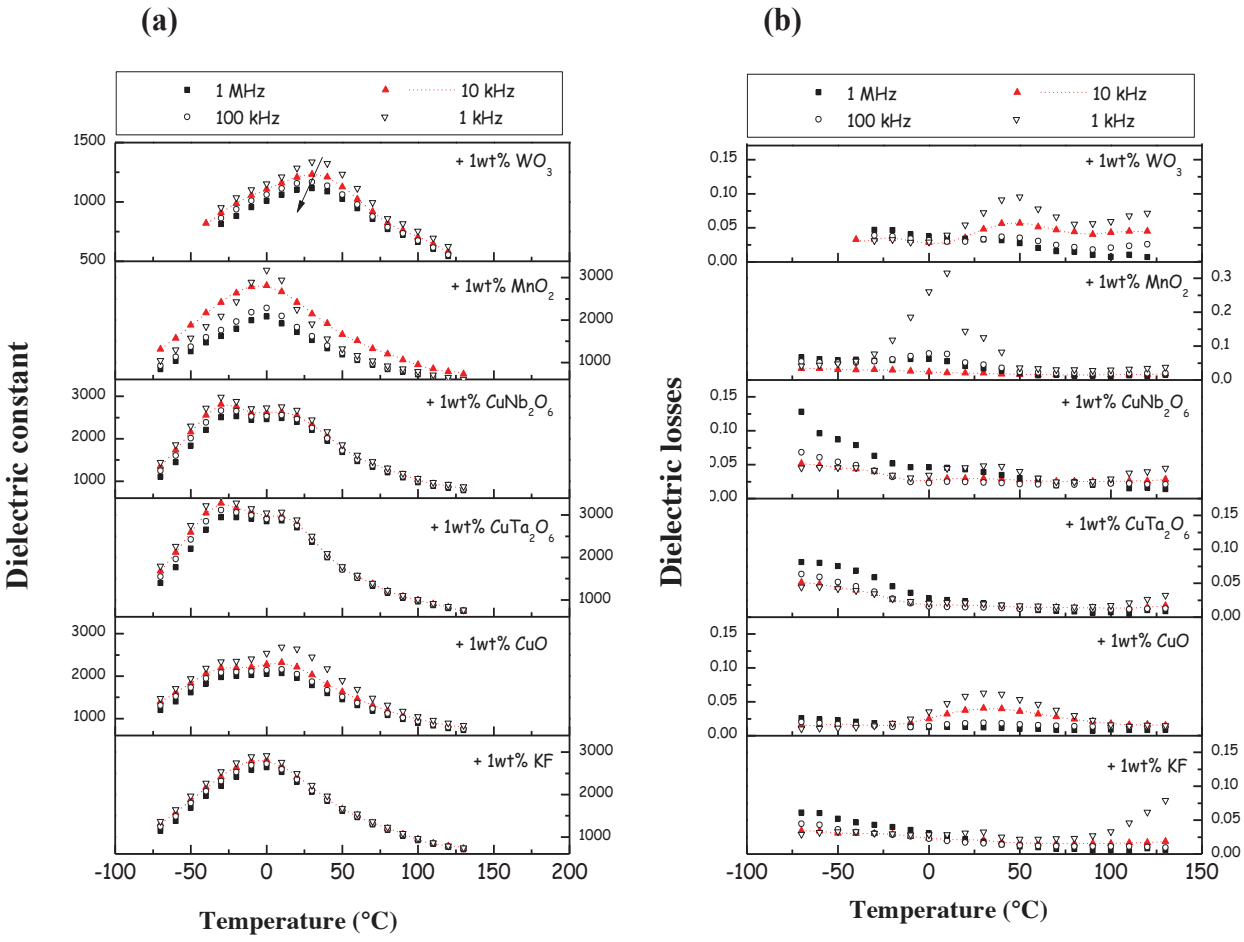

Figure 5.6. a) Dielectric constant and (b) dielectric losses of $KNb_{0.4}Ta_{0.6}O_3$ ceramics sintered in air with 1wt% sintering aids as a function of temperature and frequency..

On the other hand, MnO_2 and WO_3 appear as less reliable chemical additives when looking at the dielectric properties. The addition of WO_3 induces a decrease of the dielectric constant values; the temperature dependence of the dielectric constant curve becomes flat. According to the Shannon's effective ionic radii, W^{6+} (0.60Å) can enter into the B-site to substitute Nb^{5+}/Ta^{5+} (0.64Å) because of radius matching. The higher valence of W^{6+} could substitute the lower valence state of Nb^{5+}/Ta^{5+} producing alkali vacancies and this will result in (1) a slight distortion of the unit cell, (2) a creation of polar defects associated with A-site vacancies, and (3) a decrease of the dielectric constant [22]. Moreover, W is known to be stable under different valence states (W^{6+}, W^{5+}), which could be responsible for electronic charge carriers by hopping process. The addition of WO_3 also induces a relaxor behavior, which could be attributed, in some extent, to the decrease of the grain size, or core-shell structure if the diffusion of W is limited to the surface of the grains, as observed by SEM. Studies on $Ba_xSr_{1-x}TiO_3$ solid solutions have shown that as the grain size decreases the relative permittivity decreases as well and the transition become diffuse. In particular, for grain sizes smaller than 1 μm the relaxation frequency becomes higher [23]. On the other hand, Mn has three different valance states, Mn^{4+}, Mn^{3+} and Mn^{2+} that can generate oxygen vacancies when entering into crystal structure to substitute Nb^{5+}/Ta^{5+}. Dielectric losses might be associated to domain wall contribution, which are in connection with the oxygen vacancies that are generated when using Mn [24].

Moreover, using Cu-based additives helped to decrease the dielectric losses over a wide temperature range, less than 1%; however, the dielectric constant profile is more difficult to understand because of the presence of two peaks in dielectric constant versus temperature curves. One possible explanation is the existence of a core-shell effect, as a result of sintering aids diffusion from the surface to the core of the grains, which could induce a bi-modal distribution of Curie temperatures due to the coexistence of two ferroelectric phases.

5.1.3. - Effect of technical process on sinterability

The use of technical-assisted sintering processes, TSS and SPS, allowed us to obtained pure KN40T60 dense ceramics. The microstructure of the TSS-sample is shown

in figure 5.7a. We can observe that the surface morphology is similar to those sintered by using sintering aids, cubic-shaped grains, and that the grain boundaries appear less angular than those obtained by the conventional sintering method. This can be due to the formation of some liquid phase during the sintering process, indicated by an arrow in figure 5.7a, which helped to obtain a dense microstructure, 95%, with an average grain size of 2.2 μm.

Dielectric measurements of TSS-KN40T60 ceramics are shown in figure 5.10a. No drastic changes are observed in both maximum of the dielectric constant (~3000) and the position of the Curie temperature (~0°C) when compared with conventional sintered samples. On the other hand, the use of a TSS process had an important effect on the frequency dispersion of the dielectric constant and on the values of the dielectric losses, which was drastically reduced as a result of the higher densification state.

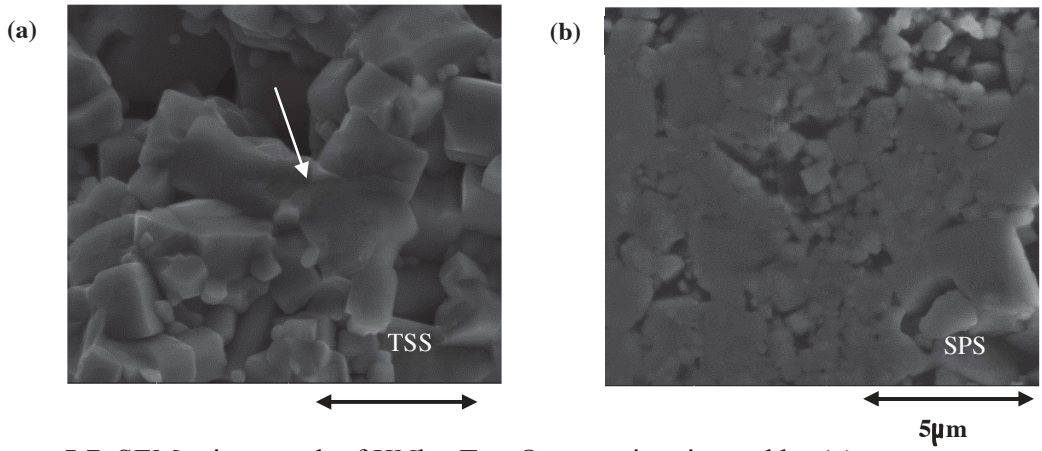

Figure 5.7. SEM micrograph of $KNb_{0.4}Ta_{0.6}O_3$ ceramics sintered by **(a)** two-step sintering (TSS) in air and **(b)** spark plasma sintering (SPS)

On the other hand, the microstructure of the sample sintered by SPS is shown in figure 5. 7b. We can observe a dense microstructure was formed, 98%, and an abnormal grain growth occurred, resulting in the presence of two types of grains, a small and a large grain, with average grain sizes of 0.7 and 2.2 μm respectively. The abnormal growth of some particles could be related to the annealing process that was applied to the sample after the SPS experiment was performed. This treatment is necessary to remove carbon traces on the pellets, coming from the SPS mold, which could represent charge carriers during the dielectric characterizations.

A polished sample of $KNb_{0.4}Ta_{0.6}O_3$ was prepared to carry out an EBSD analysis. It was first performed an EDS study and the resulting phase map, together with the tantalum and niobium elemental maps, are shown in Fig. 5.8. Ta and Nb elements were readily distinguished by the computerized phase differentiation. The high Nb content in the Ta map was identified as the darker zones on the figure while the bright one were of Ta (5.8a). The opposite case is shown on figure 5.8b, where the darker zones were richer on Ta and the light ones on Nb. Carbon element was not detected in this region of study and these results confirm that the grains in the sample are no stoichiometrically homogeneous.

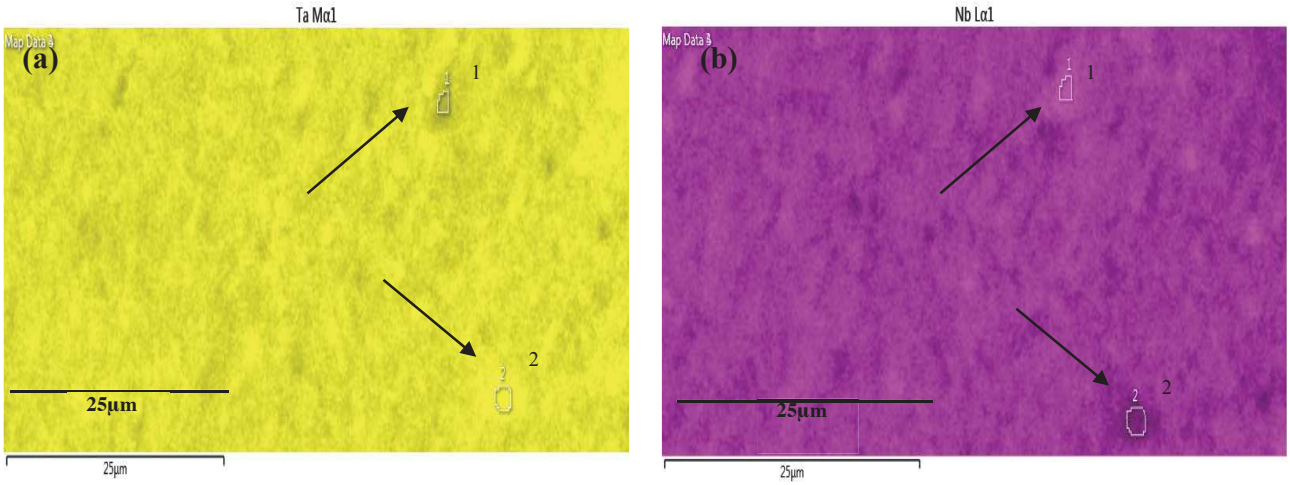

Figure 5.8. EDS phase map showing the rich zone of tantalum and niobium on a polished sample of $KNb_{0.4}Ta_{0.6}O_3$. (a) signal from the Ta Mα1 and (b) signal from the Nb Lα1.

The EBSD analysis of the different grain orientations is shown in figure 5.9. The different colors show grains orientations, blue color grains are oriented on <111> while red ones are the <001> and green ones are on the <101> directions. This indicates that $KNb_{0.4}Ta_{0.6}O_3$ SPS sample have different grain orientations, which it is something expected, as the sample is a ceramic, and it is a polycrystalline material. In addition, the average grain size of the pellet by EBSD was of ~ 1.23 µm. This confirms that by using SPS it can be obtained dense samples with fine grains.

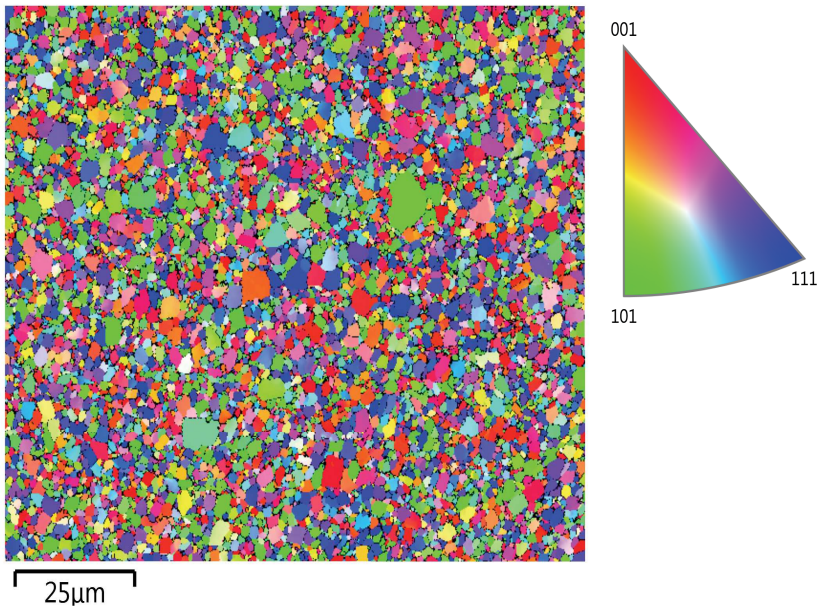

Figure 5.9. EBSD maps representing the orientation of the grains along the z-axis through inverse pole figure color-coding.

The dielectric constant and dielectric losses of the $KNb_{0.4}Ta_{0.6}O_3$ ceramic sintered by SPS as function of temperature are shown in figure 5.10b. The peak around 0°C corresponds to the tetragonal-cubic (T_C) phase transition temperature, and the overall dielectric constant behavior is not affected by the use of SPS, even though a slight decrease of the maximum of the relative permittivity is observed (~2500) which is due to a grain size effect observed in many ferroelectric perovskite materials [25]. The best results in terms of reduction of the dielectric losses (tgδ) compared with the other techniques used in this investigation were achieved by the SPS method. The tgδ values were less than 1.5% over a wide range of temperature, even at the Curie point (Fig.5.10b). The lower sintering temperature (1100°C) and shorter sintering time (5 min), compared to the TSS method, along with very high heating and cooling rates, might have reduced the concentration of defects that can degrade the dielectric properties in the $KNb_{0.4}Ta_{0.6}O_3$ ceramic. Moreover these results can also be related to the higher density of the material, very close to the theoretical one (98%), and the fine grain size confirmed by SEM and EBSD results. It has been already observed in $BaTiO_3$-based ceramics that the grain size reduction combined with high densification decreases the dielectric losses [26,27].

At high temperatures (>100°C), the tgδ continuously increases with temperature for both TSS- and SPS-samples, as shown in Figures 5.10 due to the electrical conductivity thermally activated. The strong increase of the losses for frequencies lower than 10 kHz implies the presence of electrically charged species mobile at low frequencies which give rise to an AC conductivity, as already pointed out by J. Venkatesh in air and hot-pressed KNT samples [9]

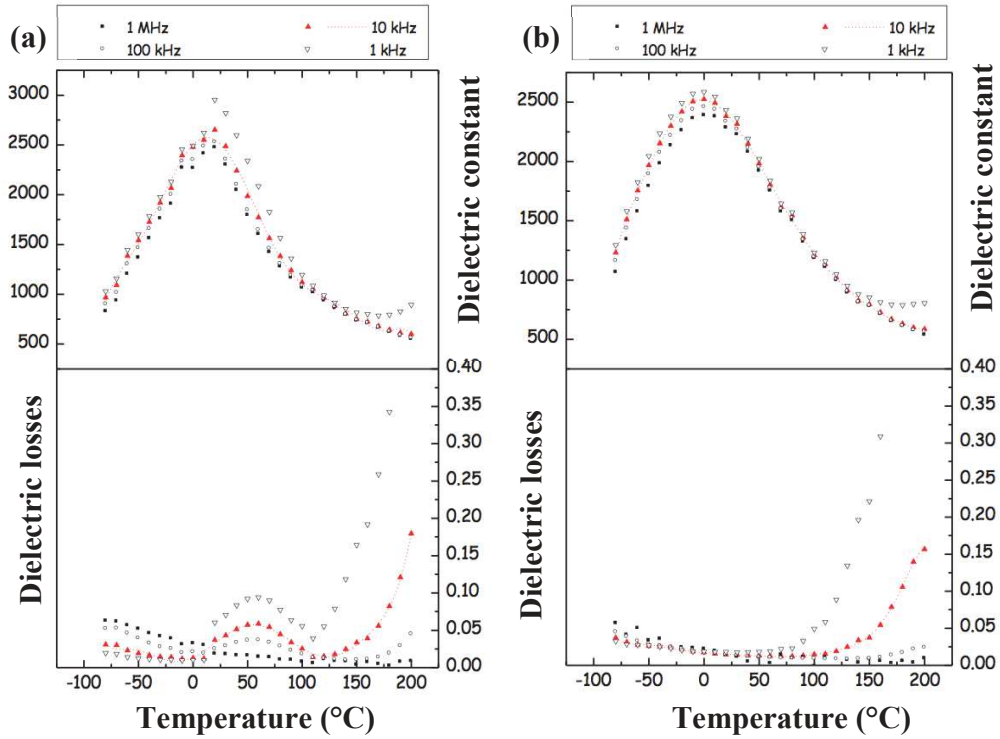

Figure 5.10. Dielectric constant and dielectric losses of $KNb_{0.4}Ta_{0.6}O_3$ ceramic sintered by **(a)** TSS and **(b)** (SPS) as a function of temperature and frequency.

It is known that the sintering conditions strongly affect the chemical composition, especially for compounds containing light elements such as alkali K^+. The EDX analysis for both TSS and SPS samples confirmed the good stoichiometry of the material, close to the exact 40:60 ratio, with no major compositional dispersion and an homogeneous Nb:Ta distribution within the grains. As a result, the use of these two sintering techniques can produce KNT samples with a dense microstructure without affecting the nominal

composition; this can be related to the lower sintering temperature used to finally consolidate the pellets, and the very fast sintering process that limits the K^+ losses

The following table presents the main characteristics of the $KNb_{0.4}Ta_{0.6}O_3$ ceramics that were studied on this investigation.

Table 5.2 Grain distribution, average grain size and density depending of the three different sintering techniques, conventional sintering (C.S), two-step sintering (TSS) and spark plasma sintering (SPS), used on the $KNb_{0.4}Ta_{0.6}O_3$ ceramics.

Sintering technique	**Sample**	**Grain size distribution [µm]**	**Average grain size [µm]**	**Density (%)**
Conventional sintering	KN40T60	0.3< ⌀ <2.5	1.8	83
	+ KF	0.3< ⌀ <3.2	2.3	93
	+ CuO	0.5< ⌀ <3.2	2.3	93
	+ $CuTa_2O_6$	0.2< ⌀ <2.5	2.3	93
	+$CuNb_2O_6$	0.2< ⌀ <3.4	2.3	93
	+ MnO_2	0.2< ⌀ <1.6	1.1	90
	+ WO_3	0.1< ⌀ <0.9	1.1	90
TSS	KN40T60	0.6< ⌀ <3.2	2.3	95
SPS	KN40T60	0.6< ⌀ <2.4	1.5	98

5.1.4. – P-E hysteresis loop behavior

Figure 5.11 shows the polarization versus electric field (P-E) hysteresis loop at -10 °C of the KN60T40 ceramics sintering with different methods. The obtained data suggests that by achieving high densities the hysteresis loops change significantly. Using sintering aids, TSS and SPS methods it was possible to enhance the ferroelectric properties of this compound.

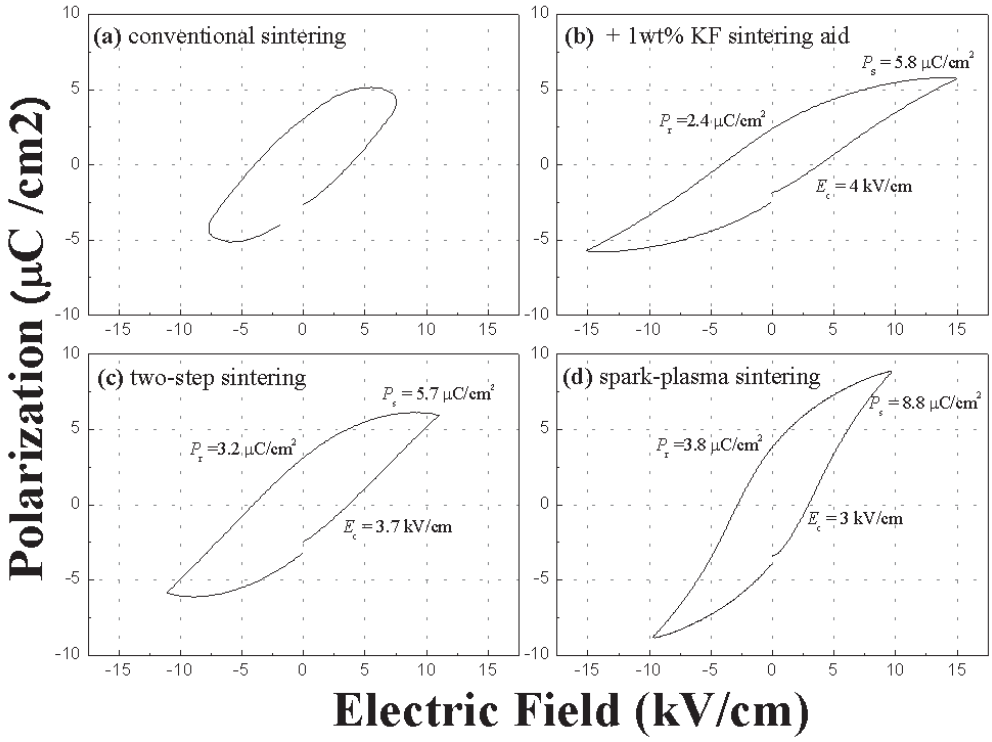

Figure 5.11. Ferroelectric hysteresis loops at -10 °C and at 1Hz of the KN60T40 ceramics: (a) conventional sintering (b) 1wt% KF sintering aid (c) two-step sintering and (d) spark plasma sintering.

The sample sintered through a conventional method, which exhibits a low density, shows a round loop (Fig. 5.11.a) that may be attributed to a high leakage currents [28], which can be confirmed by the large dielectric losses (fig. 5.3). Higher remnant polarization and reduction of the coercive electric field values were obtained for the SPS sample (Table 5.3). In addition, we can observe a decrease of the coercive field as the density increases that could be an indication that SPS ceramic contained fewer defects that impeded the domain reversal, thus an improvement of the ferroelectric response was obtained by using this sintering technique.

Table 5.3. Values of coercive field (E_c), remnant polarization (P_r), saturation polarization (P_s) and density of the KN60T40 ceramics sintered through different sintering techniques.

Sintering technique	E_c (KV/cm)	P_r ($\mu C/cm^2$)	P_s ($\mu C/cm^2$)	Density (%)
Conventional sintering	/	/	/	85
1wt% KF sintering aid	4.0	2.4	5.8	93
Two-step sintering	3.7	3.2	5.7	95
Spark plasma sintering	3.0	3.8	8.8	98

5.2. - Elaboration and Characterization of $(K_xNa_{1-x})Nb_{0.6}Ta_{0.4}O_3$ ceramics

In this part we will discuss the influence of sodium on the physical properties of $(K_xNa_{1-x})Nb_{0.6}Ta_{0.4}O_3$ (KNNT) ceramics. KNNT ceramics with various sodium concentration (x in the range of 0.9-0.5) were prepared by three different sintering processes: sintering aids, two-step sintering and spark plasma sintering. This was performed to enhance the densification of the ceramics and to study the role of these different sintering methods on their microstructure and dielectric properties.

5.2.1. - Sintering of KNNT ceramics using sintering aids through a conventional sintering process

In the previous analysis that were carried out by using different sintering aids on $K(Nb_{0.40}Ta_{0.60})O_3$ we determine that KF appeared as the most effective, the values of the dielectric losses were stable and lower than 3% over a large range of temperatures, and dense ceramics were obtained. This was the main reason why we decided to continue using 1%wt KF to sinter KNNT ceramics through a conventional sintering (CS) process. The experimental conditions were described in section 3.1.2.

Density and microstructure

The green pellets were sintered at their optimum temperatures between 1080-1170°C for 6h. The best conditions were determined by measuring the density of the final samples by the Archimedes method. Table 5.4 shows the density as function of the

composition. We can observe that the bulk density for all the compositions is higher or equal than 92% of the theoretical one.

Table 5.4. Density of ceramics depending on composition and sintering process.

Composition	Density (%)
	1%wt KF (CS)
$KNb_{0.6}Ta_{0.4}O_3$	92
$K_{0.9}Na_{0.1}Nb_{0.6}Ta_{0.4}O_3$	96
$K_{0.8}Na_{0.2}Nb_{0.6}Ta_{0.4}O_3$	95
$K_{0.7}Na_{0.3}Nb_{0.6}Ta_{0.4}O_3$	96
$K_{0.6}Na_{0.4}Nb_{0.6}Ta_{0.4}O_3$	95
$K_{0.5}Na_{0.5}Nb_{0.6}Ta_{0.4}O_3$	92

The SEM microstructures of the KNNT samples are shown in figure 5.12. All samples exhibit the typical morphology of quadrate grains; however, the pellets without any content of Na (x=1.0) presents uniform grains sizes (average grain size of 2.5 μm), with small precipitates; it was confirmed by EDX analysis that those small grains have more Ta content. In addition, there is no indication that the sintering of this sample occurred through the presence of some liquid phase. Moreover, the sample with the highest amount of Na (X=0.5) has an enlargement of the grains and the presence of small grains still remains. We can observe that even though the sintering temperature was at 1170 °C the ceramic exhibits some porosity, which is confirmed by the density measurement (92% of the theory). Nonetheless, all the other samples have a dense microstructure and abnormal grain growth occurred. This gives as a result a bimodal grain size distribution, in where it is evidenced that the sintering process was assisted by the presence of liquid phase. This might be due to the increase of the temperature in order to have samples with higher density. In order to obtain a reliable matrix of composition of the KNNT ceramics, SEM/EDX analysis was performed on a number of grains. The average value of the measured K:Na and Nb:Ta ratio are presented in the table 5.5.

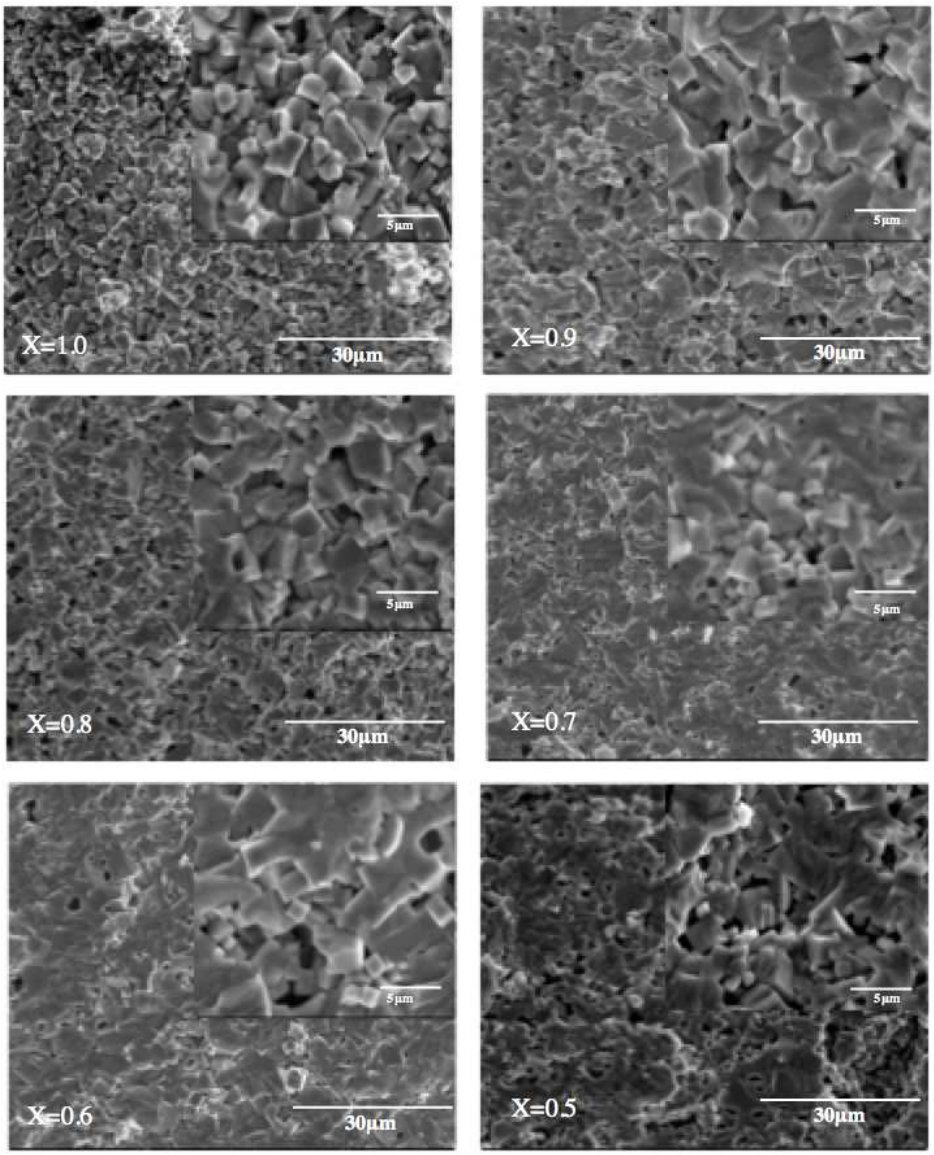

Figure 5.12. SEM images of $(K_xNa_{1-x})Nb_{0.6}Ta_{0.4}O_3$ ceramics sintered by CS with 1%wt KF. x =1.0 sintered at 1080°C/6h, x=0.9 at 1080°C/6h, x=0.8 at 1100°C/6h, x=0.7, 0.6 and 0.5 at 1170°C/6h.

As it was stated before, one major drawback of $(K,Na)(Nb,Ta)O_3$ ceramics are the special handing of the starting raw materials due to volatile alkaline elements, high sensitivity of the stoichiometry and complex densification process. However it was possible to obtain dense samples close to the stoichiometric compositions.

Table 5.5. Average ratio of the measured and nominal values of KNNT ceramics sintered by using 1%wt of KF as sintering aid

$K_xNa_{1-x}Nb_{0.6}Ta_{0.4}O_3$	Measured K:Na	Nominal K:Na	Measured Nb:Ta	Nominal Nb:Ta
x=1.0	0	0	1.32	1.50
x=0.9	11.03	9.0	1.20	
x=0.8	4.69	4.0	1.36	
x=0.7	2.93	2.3	1.44	
x=0.6	1.96	1.5	1.41	
x=0.5	1.22	1.0	1.42	

X-ray diffraction and crystalline structure

The X-ray diffraction patters of KNNT ceramics as function of the Na content are shown in figure 5.13. It is known that the crystal structure at room temperature for pure $KNb_{0.6}Ta_{0.4}O_3$ is orthorhombic [7,8]. Regardless of the added amount of Na the peaks of KNNT ceramics were all closely consistent with those of $KNb_{0.6}Ta_{0.4}O_3$. The XRD confirmed the formation of solid solutions with a perovskite phase without the presence of any second phases.

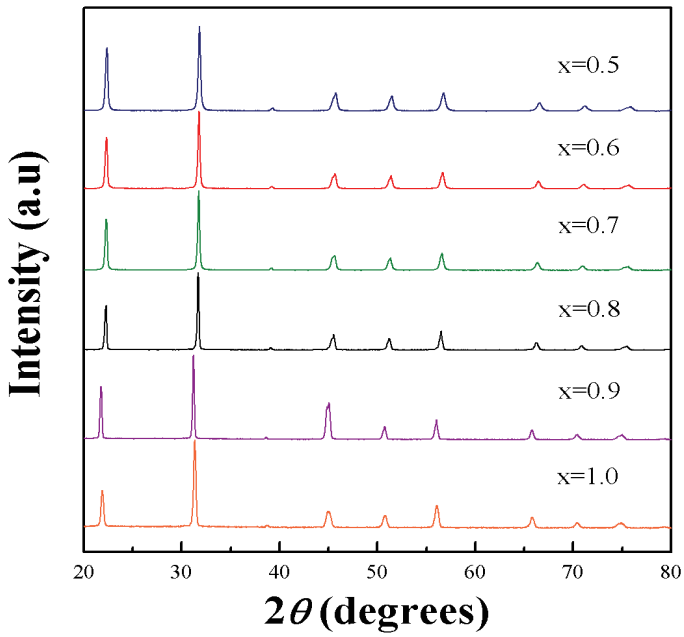

Figure 5.13. X-ray diffraction patterns of $K_xNa_{1-x}Nb_{0.6}Ta_{0.4}O_3$ ceramics with 1%KF used as sintering aid. Samples were densified through the conventional sintering method.

It was not possible to observe any splitting of the diffraction peaks for all the ceramics. However, the XRD peaks of the sintered bodies are slightly shifted toward higher angles as the amount of K decreases.

A Le bail analysis was performed for all the patterns assuming an orthorhombic symmetry (*Amm2*). Table 5.6 summarizes the lattice parameters of the KNNT ceramics.

Table 5.6. Lattice parameters of the KNNT ceramics sintered by conventional method with 1%wt KF.

Composition	*a*(Å)	*b*(Å)	*c*(Å)	V(Å^3)
$KNb_{0.6}Ta_{0.4}O_3$	3.992	5.669	5.670	128.307
$K_{0.9}Na_{0.1}Nb_{0.6}Ta_{0.4}O_3$	3.986	5.656	5.675	127.940
$K_{0.8}Na_{0.2}Nb_{0.6}Ta_{0.4}O_3$	3.977	5.638	5.670	127.135
$K_{0.7}Na_{0.3}Nb_{0.6}Ta_{0.4}O_3$	3.974	5.630	5.669	126.844
$K_{0.6}Na_{0.4}Nb_{0.6}Ta_{0.4}O_3$	3.970	5.622	5.666	126.454
$K_{0.5}Na_{0.5}Nb_{0.6}Ta_{0.4}O_3$	3.963	5.612	5.657	125.807

The volume of the lattice cell decreases linearly as the amount of potassium decreases. We can suggest that the main reason for the decrease in the volume was the effect of the substitution of sodium for potassium in where the cation radius of sodium r(Na^+) is smaller than the potassium radius r(K^+).

Raman spectroscopy at room temperature

Raman spectroscopy is a very sensitive technique used to study at local level structural changes on materials like on perovskites materials. Some of the structural modifications can be due to the tilting of the octahedral and/or cationic displacements; this could produce large changes in the vibrational modes associated with BO_6 octahedron, which will generate modification on the Raman spectrum.

The Raman spectra of the $K_xNa_{1-x}Nb_{0.6}Ta_{0.4}O_3$ sintered pellets are shown in Figure 5.14. At room temperature $KNb_{0.6}Ta_{0.4}O_3$ and $K_{0.5}Na_{0.5}NbO_3$ have orthorhombic structure in where the Raman spectrum is dominated by bands related to internal modes

of the BO_6 octahedron [29-32]. The main features in the Raman spectrum of $KNb_{0.6}Ta_{0.4}O_3$ samples are the resonance-depth at 200 cm^{-1}, the low frequency wing around 560 cm^{-1} and the mode around 840 cm^{-1} [29-31]. We can notice that as Na substitutes K there are some changes in the Raman spectra of the ceramics, being the main characteristic the loss of the resonance-depth until there is just the presence of one mode around that region. $K_{0.5}Na_{0.5}NbO_3$ has an orthorhombic structure at room temperature and the Raman spectrum is distinguishing by modes around 200 cm^{-1}, 600 cm^{-1}, and at 840 cm^{-1}, which are stretching and bending modes of the BO_6 octahedron [32,33]. These confirm that as we increase the amount of Na, the Raman spectrum changes towards the $K_{0.5}Na_{0.5}NbO_3$ spectrum, and that all the samples have at local level an orthorhombic structure. In addition, these results confirmed that the different samples have an orthorhombic structure, which was previously observed by XRD.

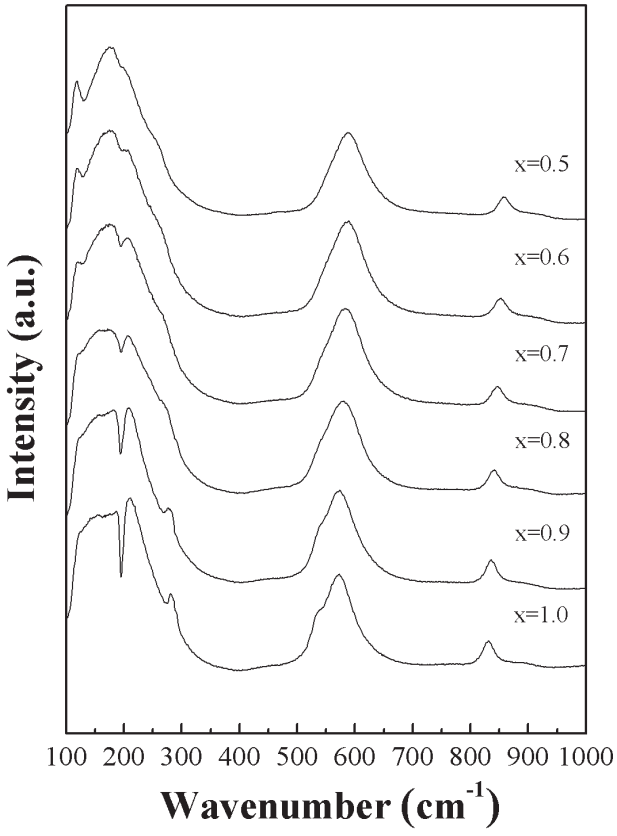

Figure 5.14. Raman spectra of the $K_xNa_{1-x}Nb_{0.6}Ta_{0.4}O_3$ ceramics sintered with 1%wt KF through a conventional method.

Dielectric properties

The dielectric constant and dielectric losses at 1MHz, 100kHz, 10kHz and 1kHz as function of temperature for unpoled $K_xNa_{1-x}Nb_{0.6}Ta_{0.4}O_3$ ceramics are given in figure 5.15. The curves have two picks, one around 45 °C and the other at 140 °C, which represent the orthorhombic-tetragonal (T_{O-T}) and the tetragonal-cubic phase transitions, the last one corresponds to the Curie Temperature (T_C). We need to point out that the sample with x=1.0 was measured between 20 and 200 °C at 10kHz and 1kHz, due to some problems with the instrument. All the other samples were tested between -30 and 180 °C. In addition, it can be observed that the Curie temperature slightly moves towards higher temperatures as the amount of K was reduced; this increment is within the uncertainty of the measurement, ± 5°C.

It has been reported for $K_{0.5}Na_{0.5}NbO_3$ single crystals that the T_{O-T} and T_C are at 192 and 410°C, respectively with a dielectric constant of 1015 at room temperature [34]. Moreover, it was shown that for ceramics with a composition of $K_{0.5}Na_{0.5}Nb_{0.7}Ta_{0.3}O_3$ the T_{O-T} and T_C were approximately 80 and 220 °C with a dielectric constant of 967 at room temperature [35], this is summarized in Table 5.7.

Table 5.7 T_{O-T} ,T_C and dielectric constant values of KNN and KNNT samples at 1kHz.

Composition	**T_{O-T} (°C)**	**T_C (°C)**	**Dielectric constant (Room Temperature)**
$K_{0.5}Na_{0.5}NbO_3$ [31]	192	410	1015
$K_{0.5}Na_{0.5}Nb_{0.7}Ta_{0.3}O_3$ [32]	80	220	967
$K_{0.5}Na_{0.5}Nb_{0.6}Ta_{0.4}O_3$	45	135	1302

Moreover, it was shown that the shift of T_{O-T} and T_C is mainly due to the Nb/Ta ratio [36,37]. Figure 5.15 shows how the dielectric constant of KNNT ceramics at the T_c increased as the amount of sodium was increased. These results are similar for those reported previously for KNN and KNNT samples [38, 39]. Besides, changes of the T_{O-T} and T_C were not observed as the amount of Na increased. This confirms that the Nb/Ta ratio is the responsible on shifting to lower temperatures the T_{O-T} and T_C transitions. Moreover, The sample with x=0.1 has the broadest maximum around 175 °C, indicating

that the ferroelectric to paraelectric transition becomes diffusive.

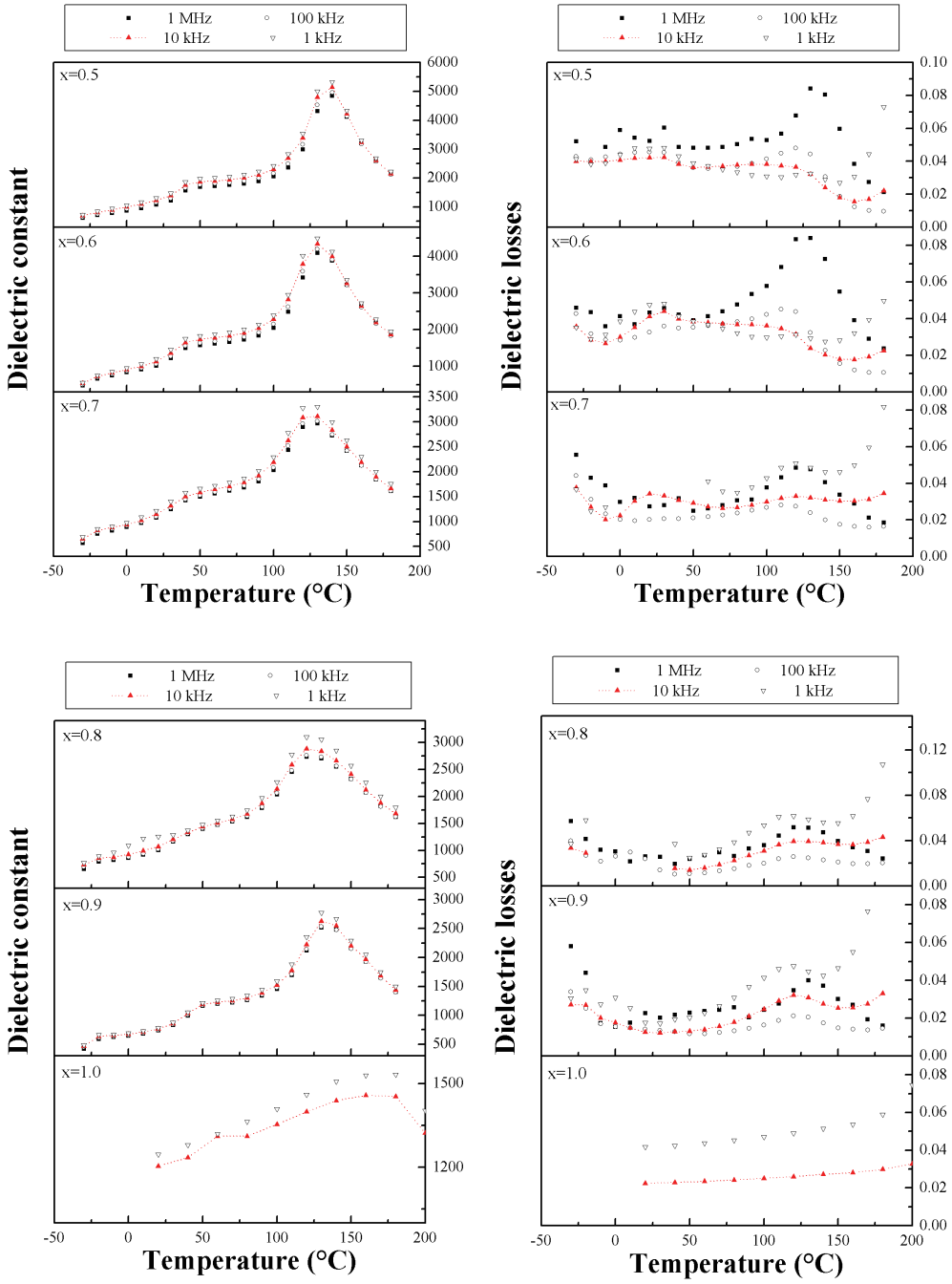

Figure 5.15. Temperature dependence of the dielectric constant and dielectric losses of $K_xNa1_{-x}Nb_{0.6}Ta_{0.4}O_3$ ceramics sintered with 1%wt KF by a conventional method.

The two changes observed in the dielectric constant versus temperature, are also

identified in most of the dielectric losses of the KNNT ceramics. The dielectric losses did not exceed 4% from room temperature and even after the first transition (T_{O-T}). At the Curie temperature the dielectric losses increased up to 8%. The dielectric losses increases with temperature after the T_c and these large values are most probably contributed to the electrical conductivity thermally activated.

5.2.2. - Sintering of KNNT ceramics by two-step sintering process

The second technique used to sinter the $(K_xNa_{1-x})Nb_{0.6}Ta_{0.4}O_3$ (KNNT) ceramics was two-step sintering (TSS). Different temperatures and conditions were carried out in order to have well dense samples. The experimental procedure was described in section 3.2.2.

Density and microstructure

Two sintering temperatures were used during this sintered process; the first temperature was between 1150 and 1200°C for 6min, followed by a second sintering temperature in the range of 1100 and 1150°C for 6h, depending on the composition. Table 5.8 shows the density values obtained by the Archimedes method.

Table 5.8. Density of the ceramics sintered by TSS depending on composition.

Composition	Density (%)
	TSS
$KNb_{0.6}Ta_{0.4}O_3$	94
$K_{0.9}Na_{0.1}Nb_{0.6}Ta_{0.4}O_3$	97
$K_{0.8}Na_{0.2}Nb_{0.6}Ta_{0.4}O_3$	94
$K_{0.7}Na_{0.3}Nb_{0.6}Ta_{0.4}O_3$	96
$K_{0.6}Na_{0.4}Nb_{0.6}Ta_{0.4}O_3$	95
$K_{0.5}Na_{0.5}Nb_{0.6}Ta_{0.4}O_3$	98

The final bulk density for all the compositions is between 94 and 98 % of the theoretical one. We can observe that by using TSS it was obtained samples with a higher density than those sintered using 1%wt KF through a CS process. However, by using this method high temperatures are needed for a very short time in order to have some liquid phase during the sintering process and to obtain dense samples.

SEM analysis was performed on the surface fracture for all the samples. As it can be seen in figure 5.16 the grains for all the pellets are cubic like shape. Sample with x=1.0 have a dense microstructure, with average grain size of 2.3 μm; there is some grain enlargement, and the presence of small ones which are rich on Ta. On the other hand, pellets with x=0.8 and 0.7 have a very uniform grain size distribution in where there is no indication that the sintering process was assisted through some liquid phase, and grains are well define with average size of 1.6 and 2.3 μm, respectively. In addition, the pellet with x=0.6 have a bimodal distribution, with some abnormal grains size along with cubic particles. We can assume that due to the high temperature there was some liquid phase during the sintering process. Finally, the surface morphology of the samples with x=0.9 and 0.5 is characterized by irregular-shape grain in where the grain boundaries are not well define. This confirms that for those samples the sintering occurred through the present of liquid phase. Some pores have still been observed for all the samples, confirmed by the measured density.

An EDX analyses were performed on different grains of each sample in order to have the matrix composition of each of them. Table 5.9 shows the average measured ratio of K:Na and Nb:Ta.

Table 5.9. Average ratio of the measured and nominal values of KNNT ceramics sintering by TSS method.

$K_xNa_{1-x}Nb_{0.6}Ta_{0.4}O_3$	Measured	Nominal	Measured	Nominal
	K:Na	K:Na	Nb:Ta	Nb:Ta
x=1.0	-	-	0.98	1.50
x=0.9	8.4	9.0	1.55	
x=0.8	6.0	4.0	1.81	
x=0.7	3.6	2.3	1.68	
x=0.6	1.9	1.5	1.37	
x=0.5	1.3	1.0	1.50	

The sintering conditions strongly affect the chemical composition of potassium-based compounds. It has been reported before that in KNN-based ceramics Na evaporates

more actively than K with temperature [40]. The high temperatures used during the TSS process might have promoted the evaporation of the alkaline elements and the measured stoichiometric composition differs from the nominal.

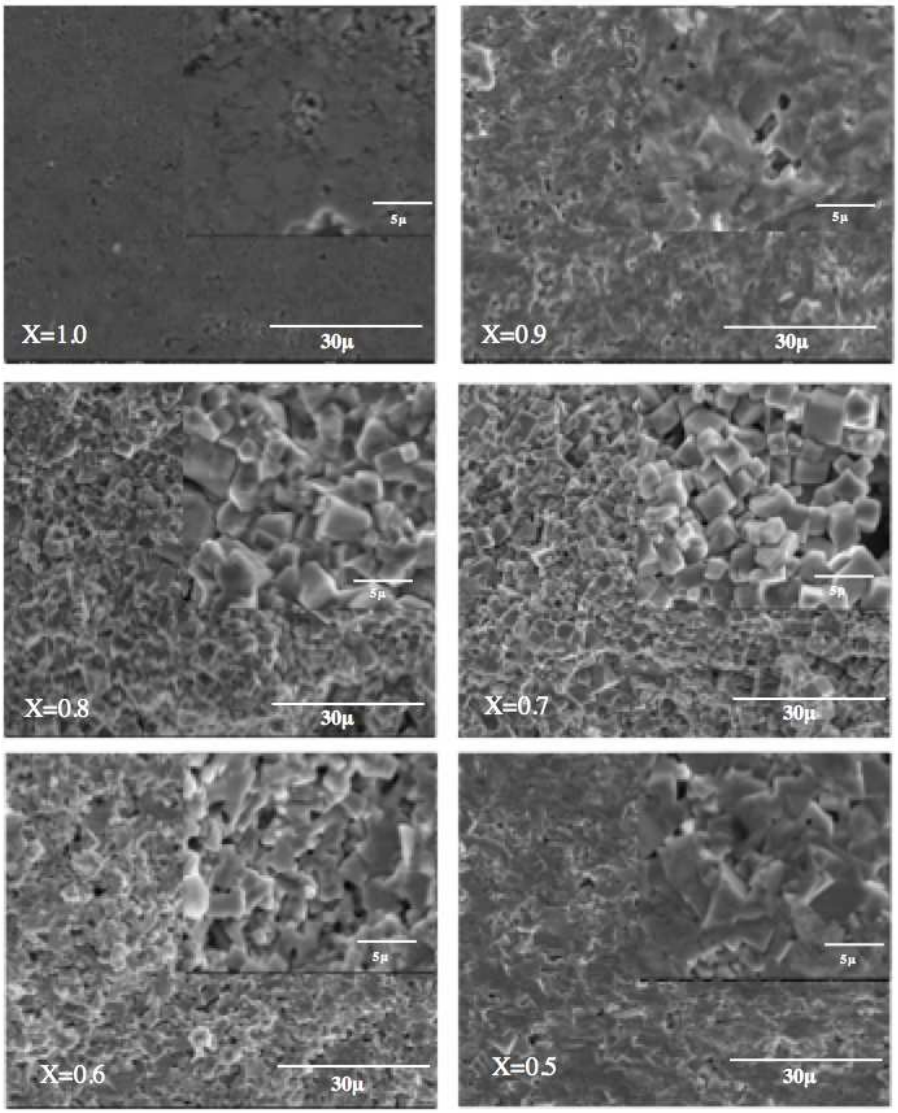

Figure 5.16. SEM images of $(K_xNa_{1-x})Nb_{0.6}Ta_{0.4}O_3$ ceramics sintered by TSS. x =1.0 sintered at 1150°C/0.1h - 1100°C/6h , x=0.9 at 1150°C/0.1h - 1100°C/6h , x=0.8 at 1160°C/0.1h - 1100°C/6h, x=0.7, 0.6 at 1170°C/0.1h - 1150°C/6h, and X=0.5 at 1200°C/0.1h - 1150°C/6h.

X-ray diffraction and crystalline structure

The X-ray diffraction patterns of KNNT ceramics samples as function of the Na content are presented in figure 5.17. It is known that the room-temperature crystal structure of pure $KNb_{0.6}Ta_{0.4}O_3$ is orthorhombic [7,8]. Regardless of the added amount of Na the peaks of KNNT ceramics were all closely consistent with those of $KNb_{0.6}Ta_{0.4}O_3$. The XRD confirmed the formation of solid solutions with a perovskite phase without the presence of any second phases. In addition, it was not possible to observe any peak splitting; however, as the amount of Na was increased there is a small shift to higher angles.

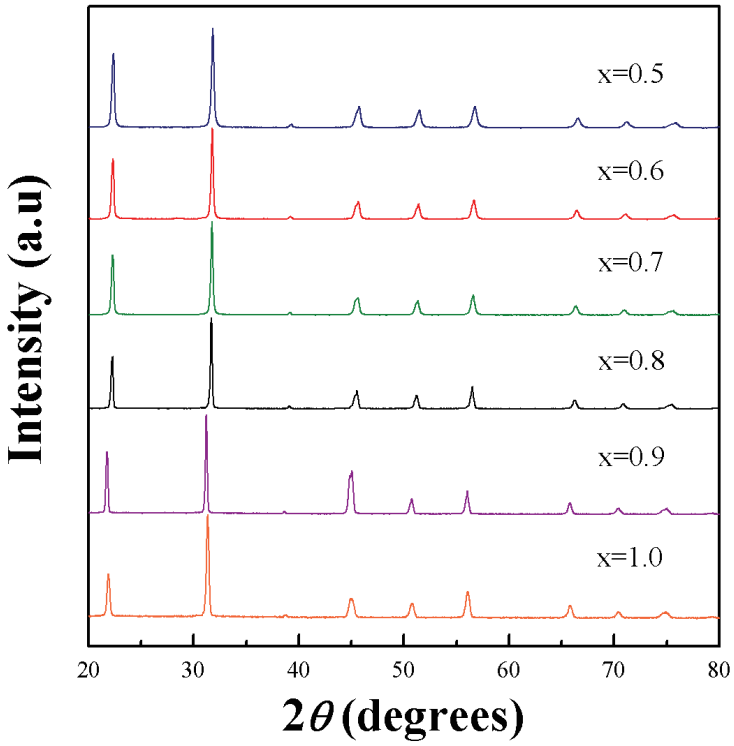

Figure 5.17. X-Ray Diffraction patterns of $K_xNa_{1-x}Ta_{0.4}Nb_{0.6}O_3$ ceramics obtained through a 2-step sintering method.

A profile matching was carried out for all the diffractogram supposing an orthorhombic structure. The lattice parameters are shown on table 5.10; it can be seen that the cell volume decreases as the amount of Na increases due to element substitution of Na for K.

Table 5.10. Lattice parameters of the KNNT ceramics sintered by TSS method

Composition	*a*(Å)	*b*(Å)	*c*(Å)	V(Å^3)
$KNb_{0.6}Ta_{0.4}O_3$	3.992	5.665	5.657	127.953
$K_{0.9}Na_{0.1}Nb_{0.6}Ta_{0.4}O_3$	3.982	5.645	5.674	127.547
$K_{0.8}Na_{0.2}Nb_{0.6}Ta_{0.4}O_3$	3.978	5.638	5.675	127.292
$K_{0.7}Na_{0.3}Nb_{0.6}Ta_{0.4}O_3$	3.977	5.635	5.676	127.209
$K_{0.6}Na_{0.4}Nb_{0.6}Ta_{0.4}O_3$	3.970	5.627	5.661	126.461
$K_{0.5}Na_{0.5}Nb_{0.6}Ta_{0.4}O_3$	3.962	5.616	5.657	125.874

Raman spectroscopy at room temperature

As it was described before, it is possible to see structural changes at local level with the use of Raman spectroscopy. Figure 5.18 shows the main features of $KNb_{0.6}Ta_{0.4}O_3$ (x=1.0), which are a resonance-depth at 200 cm^{-1}, a low frequency wing around 560 cm^{-1} and a mode around 840 cm^{-1} [29-31]. As the amount of Na increases, the Raman spectrum of the ceramics changes from the pure like spectrum of $KNb_{0.6}Ta_{0.4}O_3$ towards the $K_{0.5}Na_{0.5}NbO_3$ spectrum, which is orthorhombic at room temperature as well [31]. This confirms that all the samples at a local level have an orthorhombic structure at room temperature. We have to point out that the small peak around 510 cm^{-1} for the composition with x=0.7 does not comes from sample and it is due to the instrument.

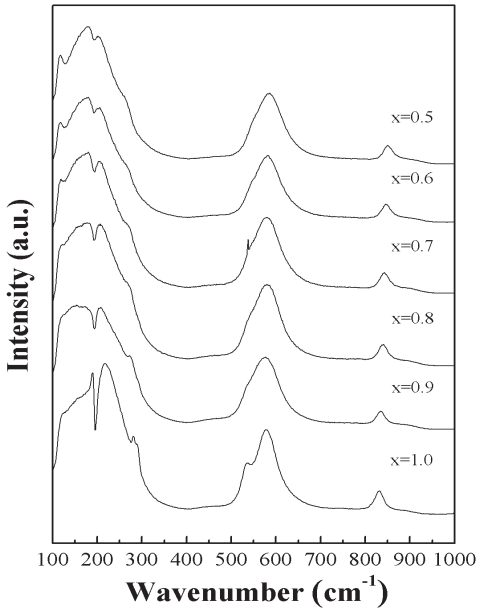

Figure 5.18. Raman spectra of the $K_xNa_{1-x}Nb_{0.6}Ta_{0.4}O_3$ ceramics sintered through a two-step method.

Dielectric properties

The dielectric measurements for the samples sintered in air by a two-step sintering method are shown in figure 5.19 and 5.20. The ceramics with x=1.0, 0.9 and 0.8 compositions show a diffuseness of the T_C transition, around 125°C. One possible reason for this behavior is the fluctuation in the composition of the ceramics, which was already reported for KNT samples [11].

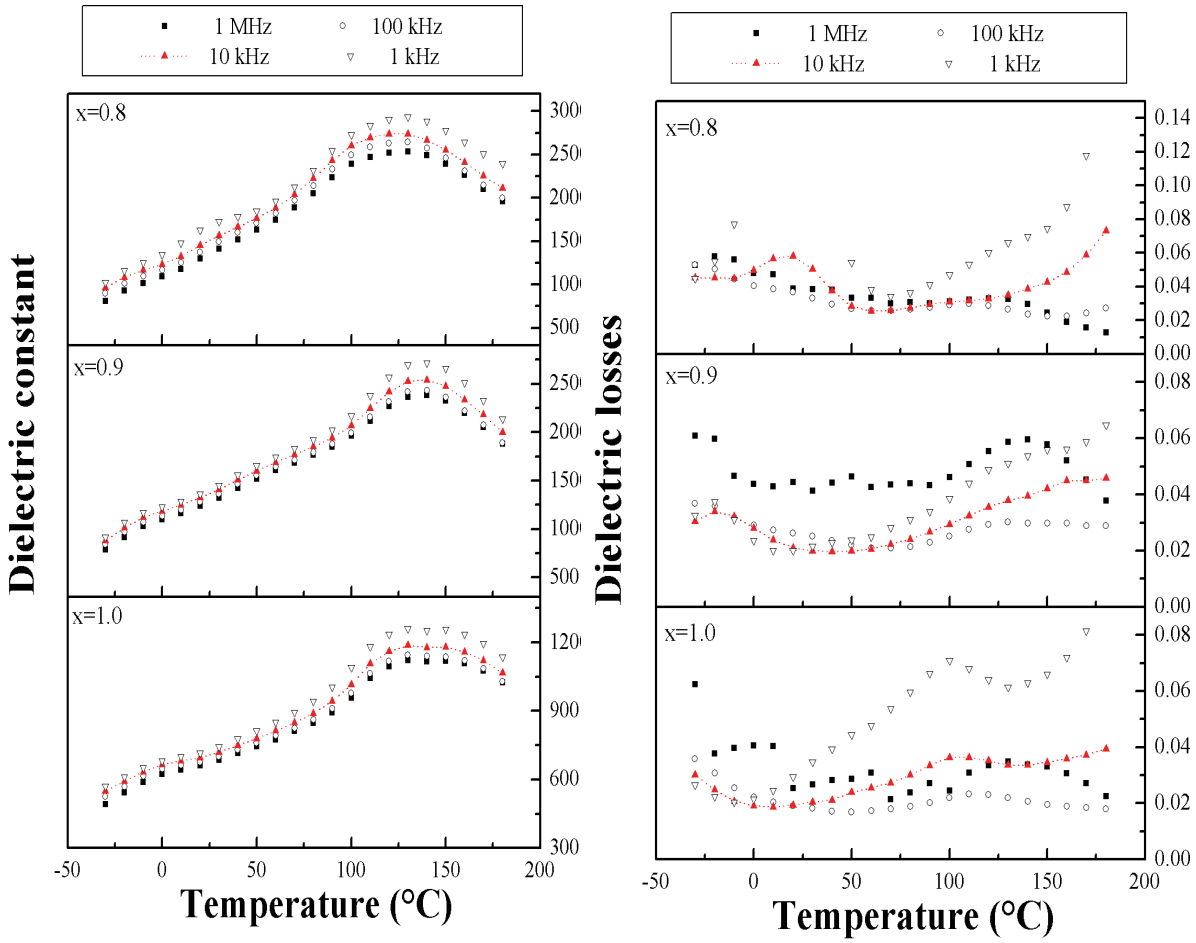

Figure 5.19. Temperature dependence of the dielectric constant and dielectric losses of $K_xNa1_{-x}Nb_{0.6}Ta_{0.4}O_3$ (x=1.0, 0.9, 0.8) ceramics sintered by a TSS method.

On the other hand, the two-phase transitions, T_{O-T} and T_C, were observed for all the other pellets approximately at 45 and 125 °C. These values are near to the ones obtained for the ceramics of the same composition sintered with 1%KF by conventional

methods. The highest maximum of the dielectric constant at the T_C was for the $K_{0.5}Na_{0.5}Nb_{0.7}Ta_{0.3}O_3$ sample. In addition, as the amount of Na increases the dielectric constant increases as well, which confirms the results obtained previously for the samples sintered by CS.

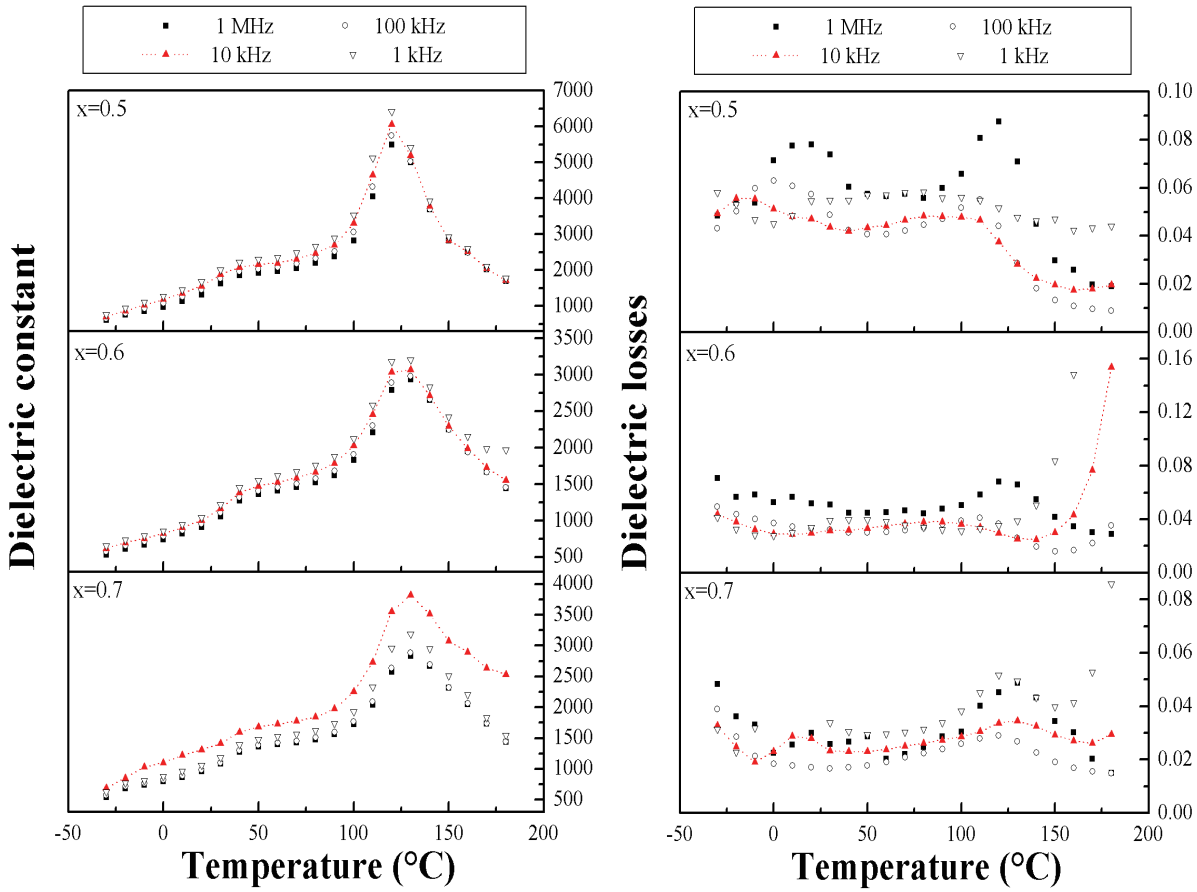

Figure 5.20. Temperature dependence of the dielectric constant and dielectric losses of $K_xNa_{1-x}Nb_{0.6}Ta_{0.4}O_3$ (x=0.7, 0.6, 0.5) ceramics sintered by a TSS method.

The dielectric losses were around 4 to 8%, being the highest losses at the T_C, and they continued to increase after this transition. The value of the dielectric losses at high temperatures for these samples is much larger than those sintered by the CS method. This may be due to the fact that the firing temperatures were higher and it is likely to induce more defects on the samples, like charge defect concentration [9]. However, the overall dielectric constant behavior is not affected by the use of the TSS method.

5.2.3. – Sintering of KNNT ceramics by spark plasma sintering process

In this part, the effect of spark plasma sintering (SPS) on the phase structure of four $(K_xNa_{1-x})Nb_{0.6}Ta_{0.4}O_3$ (x=0.1, 0.9, 0.8 and 0.6) ceramics is discussed in detail by considering the microstructure, XRD patterns, as well as the temperature dependence of the dielectric constant.

Density and microstructure

As it was mentioned before, SPS is a technique that allows to fully densified samples while keeping small grains because of the fast way of heating and applying pressure at the same time. The temperature range was between 1000 and 1100°C for very short time and with a pressure of 100MPa. The experimental conditions are described on section 3.2.3. The density values obtained by the Archimedes method are presented in the following table. We can observe that by using the SPS method we were able to obtain the most densified samples, around 99%, from all the other methods described before.

Table 5.11. Density of the ceramics sintered by SPS depending on composition.

Composition	Density (%)
	SPS
$KNb_{0.6}Ta_{0.4}O_3$	98
$K_{0.9}Na_{0.1}Nb_{0.6}Ta_{0.4}O_3$	98
$K_{0.8}Na_{0.2}Nb_{0.6}Ta_{0.4}O_3$	99
$K_{0.6}Na_{0.4}Nb_{0.6}Ta_{0.4}O_3$	99

Microstructures of fracture surfaces of the samples with compositions of KNNT after annealing are shown in figure 5.21. The microstructure of the samples with x=1.0 and 0.8 consisted of rectangular shape grains with average grain size of 1.25-2.20 μm, respectively and the fracture mechanism was mainly intergranular. On the other hand, we can observe that the facture took place in the grains for the pellets with x=0.9 and 0.6 and the grain size was determine about 5μm. Although SPS method enables to control the grain growth mechanism, an enlargement in grain size was observed. This results point out that the grain growth of the samples may be attributed to the element substitution.

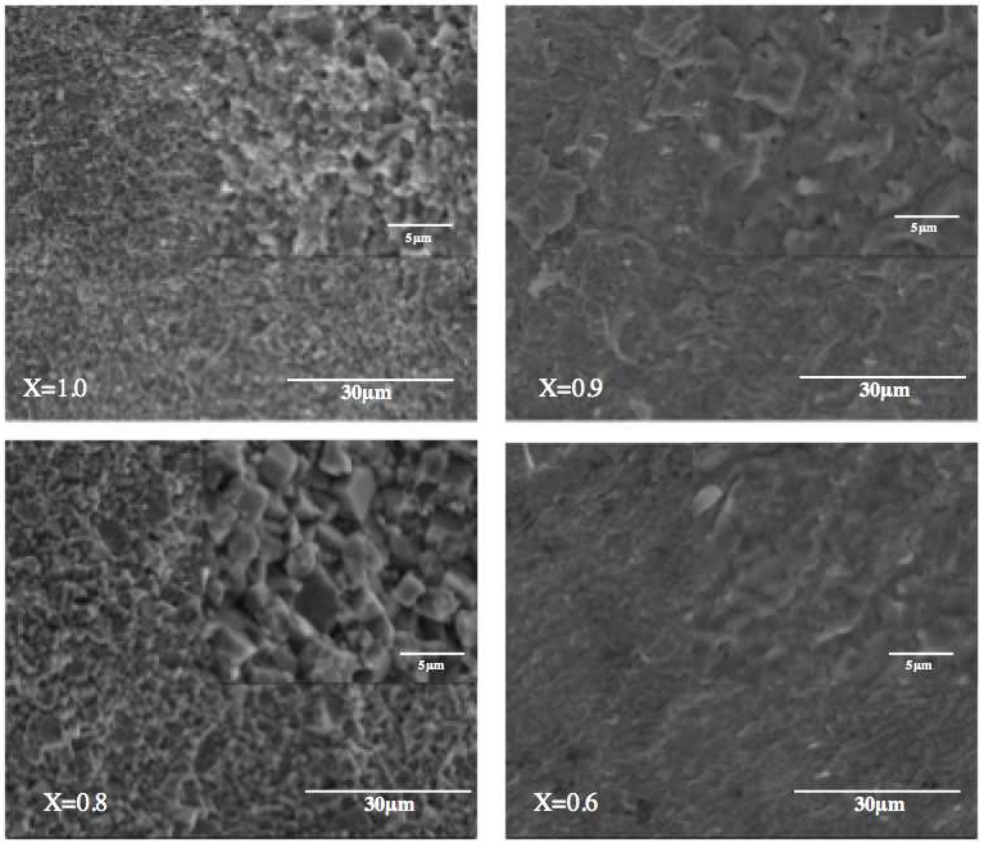

Figure 5.21. SEM images of $(K_xNa_{1-x})Nb_{0.6}Ta_{0.4}O_3$ ceramics sintered by SPS. x =1.0 sintered at 1040°C/5min-100MPa, x=0.9 at 1000°C/1min-100MPa, x=0.8 at 1020°C/1min – 100MPa, and X=0.6 sintered at 1050°C/1min – 100MPa

The EDX analyses were done on different grains of each sample in order to have their matrix composition. We can see that there are small inhomogeneities between the nominal and measured values. This could be due to the temperatures used during the calcination and sintering process.

Table 5.12. Average ratio of the measured and nominal values of KNNT ceramics sintering by SPS method.

$K_xNa_{1-x}Nb_{0.6}Ta_{0.4}O_3$	Measured K:Na	Nominal K:Na	Measured Nb:Ta	Nominal Nb:Ta
x=1.0			1.39	1.50
x=0.9	10.4	9.0	1.29	
x=0.8	4.9	4.0	1.34	
x=0.6	1.9	1.5	1.40	

X-ray diffraction and crystalline structure

The ceramics XRD of the air annealed SPS samples are shown in figure 5.22. It can be seen clear perovskite single phase for KNNT ceramics without any graphite contamination detected.

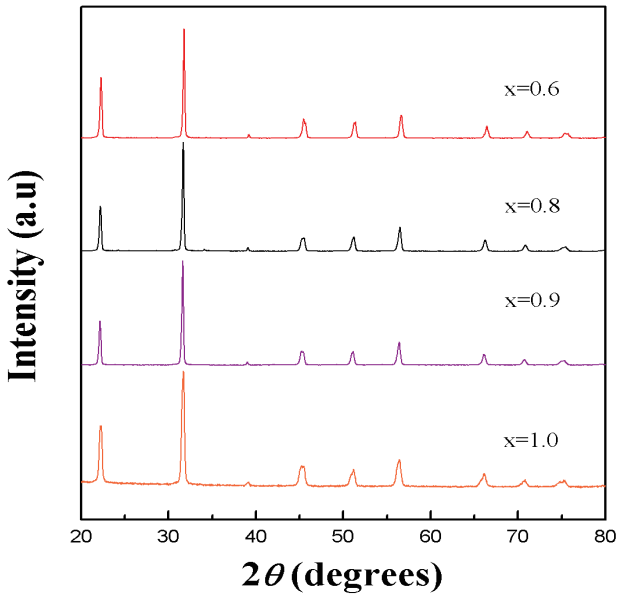

Figure 5.22. X-Ray Diffraction patterns of $K_xNa_{1-x}Ta_{0.4}Nb_{0.6}O_3$ ceramics sintered by SPS technique.

A profile matching was performed using an orthorhombic structure (*Amm2*). The results are shown on table 5.13. A decrease of the cell volume is observed, which could be due to the replacement of K with Na ion in the unit cell. This can be as well seen on the XRD patterns with a small shift to higher angles as K decreases.

Table 5.13. Lattice parameters of the KNNT ceramics sintered by SPS method.

Composition	*a*(Å)	*b*(Å)	*c*(Å)	V(Å^3)
$KNb_{0.6}Ta_{0.4}O_3$	3.989	5.655	5.697	128.530
$K_{0.9}Na_{0.1}Nb_{0.6}Ta_{0.4}O_3$	3.983	5.648	5.676	127.680
$K_{0.8}Na_{0.2}Nb_{0.6}Ta_{0.4}O_3$	3.982	5.643	5.681	127.669
$K_{0.6}Na_{0.4}Nb_{0.6}Ta_{0.4}O_3$	3.9719	5.6291	5.6649	126.6567

Raman spectroscopy at room temperature

The Raman spectrum of $KNb_{0.6}Ta_{0.4}O_3$ (x=1.0) showed the main features associated with the BO_6 vibrations [29-31]. As the amount of Na was increased there were some changes on the spectra of the samples evolving towards the $K_{0.5}Na_{0.5}NbO_3$ spectrum [31]. All the samples were confirmed as consisting of an orthorhombic structure. These results are in good agreement with the ones obtained previously during this investigation by using the CS and TSS methods.

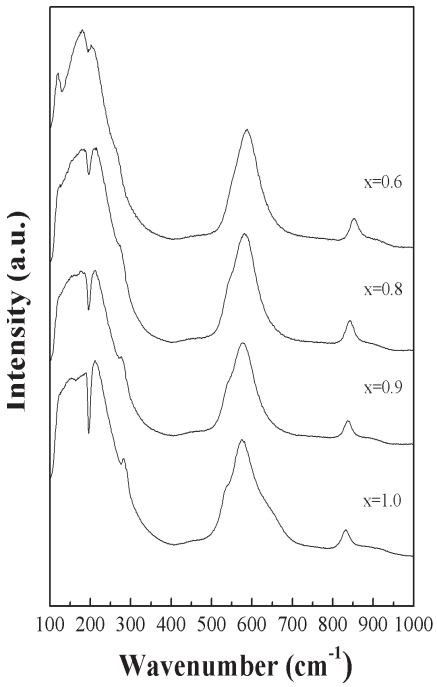

Figure 5.23. Raman spectra of the $K_xNa_{1-x}Nb_{0.6}Ta_{0.4}O_3$ ceramics sintered by SPS.

Dielectric properties

The temperature dependence of the dielectric constant and dielectric losses for KNNT samples sintered by SPS is shown in figure 5.24. The dielectric constant versus temperature for samples with x=1.0, 0.9 and 0.8 shows a broad peak at the Curie temperature and no other transitions were observed for this samples at lower temperature. These broad maximum around 120°C indicates that the ferroelectric to paraelectric transition becomes diffusive. Meanwhile the sample with the lowest content of K (x=0.6) shows the two-phase transitions, T_{O-T} and T_C, around at 50 and 130 °C. The fact that the

grain growth increased and that the diffusiveness was reduced for this sample might be an indication that the perovskites was compositionally inhomogeneous.

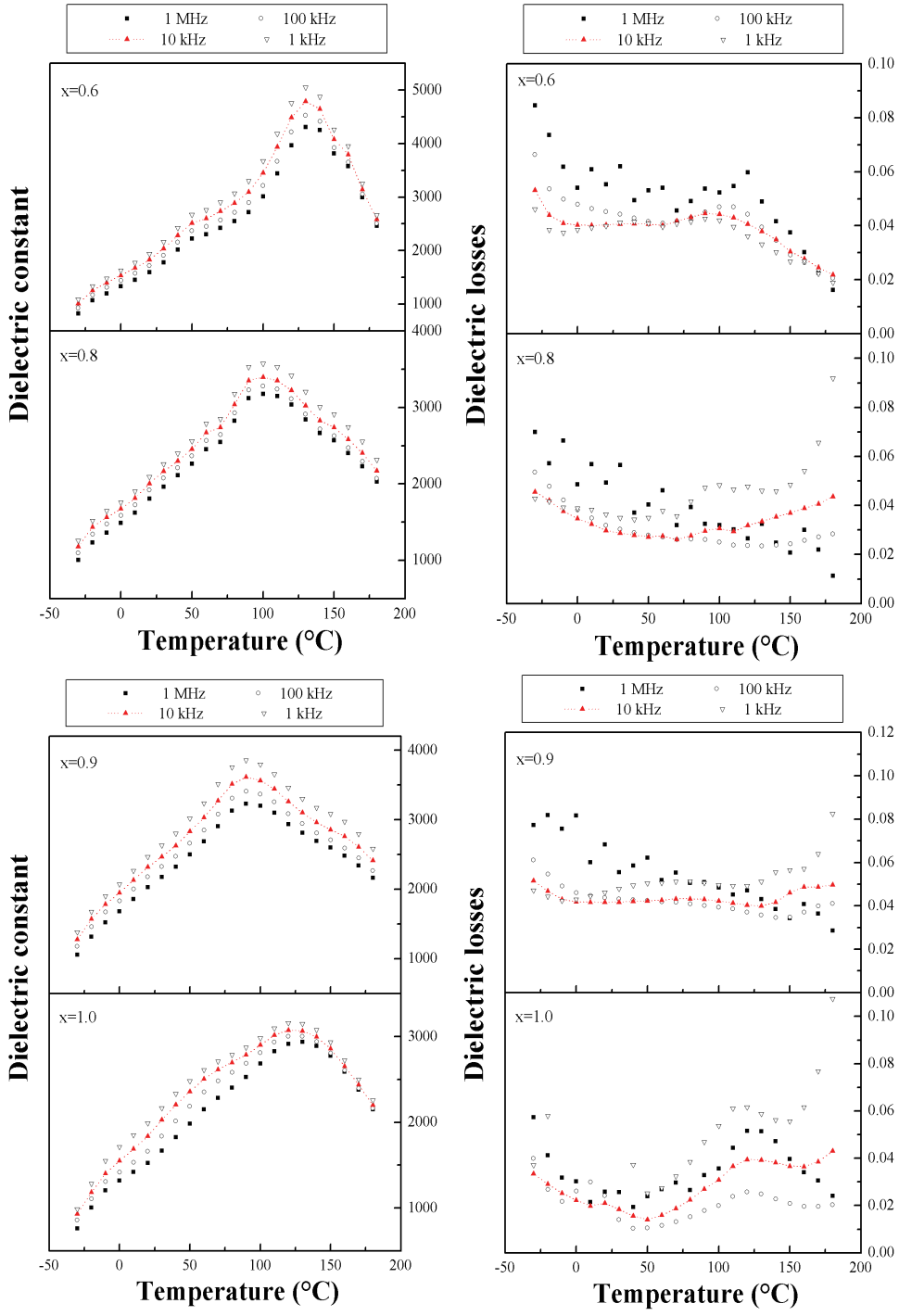

Figure 5.24. Temperature dependence of the dielectric constant and dielectric losses of $K_xNa_{1-x}Nb_{0.6}Ta_{0.4}O_3$ ceramics sintered by SPS.

In addition, it was also observed that as Na increased, there was an increase of the dielectric constant value. The dielectric losses were between 2 and 8% for a very long range of temperature. At high temperatures it was observed the same behavior as for CS and TSS samples.

5.2.4. – P-E hysteresis loops behavior

The best ferroelectric results obtained for the KN40T60 ceramics were for the sample sintered through the SPS method due to the high densification that was achieved. Therefore, the ferroelectric study for the KNNT pellets was conducted for the samples sintered through the same technique. Figure 5.25 shows the room temperature P-E hysteresis loops for the $(K_xNa_{1-x})Nb_{0.6}Ta_{0.4}O_3$ (x=1.0, 0.9, 0.8, 0.6) ceramics sintered by SPS. All samples display well-saturated ferroelectric curves, except for the (K90Na10)N60T40 sample (fig.5.25.b) that has a rounded-like shape, attributable to some degree of electric conductance. This conductance at room temperature could be due to composition inhomogeneities that were already discussed on the dielectric properties. On the other hand, we can observe that the ferroelectric properties are stable at different frequencies and the remnant polarization increases with the Na content (Table 5.14). The saturation polarization could not be reached due to device restrictions; this explains the low values observed for P_r and P_s

Table 5.14. Values of coercive field (E_c), remnant polarization (P_r), saturation polarization (P_s) of the KNaN60T40 ceramics sintered through different sintering techniques at 0.1Hz.

Sample	E_c (KV/cm)	P_r ($\mu C/cm^2$)	P_s ($\mu C/cm^2$)
KN60T40	2.7	3.8	8.8
(K90Na10)KN60T40	2.8	4.0	7.0
(K80Na10)KN60T40	3.1	5.0	9.2
(K60Na40)KN60T40	3.1	7.5	15

Similar trend was obtained for the dielectric behavior, which showed an enhancement of the dielectric constant with the amount of Na. furthermore, the composition of (K60Na40)N60T40 has an optimal ferroelectric behavior compared to the pure KN60T40 sample, remnant polarization is almost two time higher and the coercive field did not increase significantly.

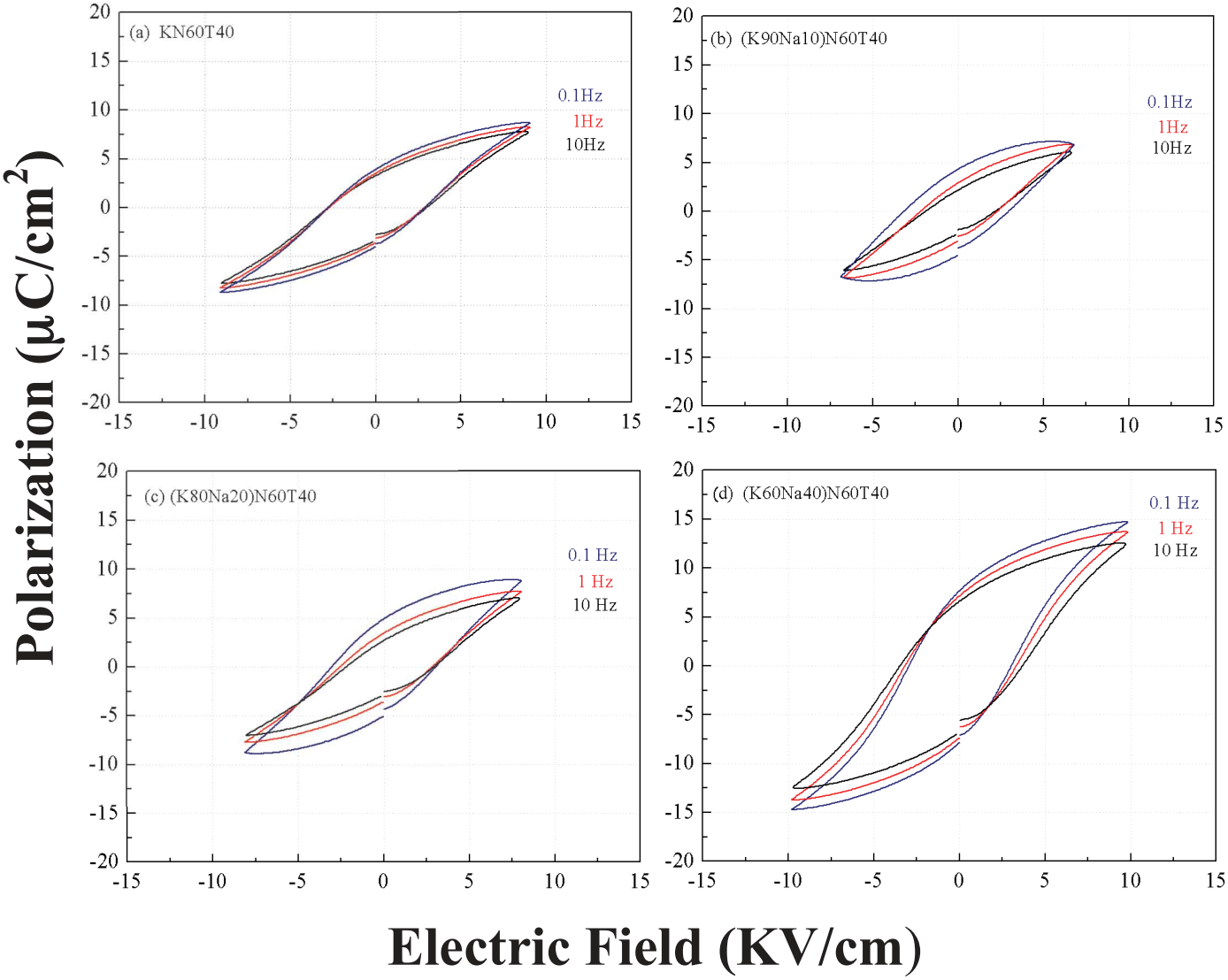

Figure 5.25. P-E hysteresis loops at room temperature of KNNT ceramics: (a) $KNb_{0.6}Ta_{0.4}O_3$, (b) $K_{0.9}Na_{0.1}Nb_{0.6}Ta_{0.4}O_3$, (c) $K_{0.8}Na_{0.2}Nb_{0.6}Ta_{0.4}O_3$ and (d) $K_{0.6}Na_{0.4}Nb_{0.6}Ta_{0.4}O_3$

5.3. – Conclusions

$K(Nb_{0.40}Ta_{0.60})O_3$ ceramics were sintered to a high relative density through the use of sintering aids, two-step sintering and spark plasma sintering methods, and their microstructure and dielectric properties were studied. The *Tc* for all the ceramics were shifted to lower temperatures, and the maximum of the dielectric constant was obtained for the samples sintered with the use of KF and the TSS technique. Additionally, their dielectric losses were significantly reduced. The presence of an excess of K decreased the formation of potassium vacancies and enhanced the dielectric properties. SEM images showed fine-grain size for SPS ceramic, the maximum density of 98% and the lowest dielectric losses (tan δ <1.5%) were obtained through the use of this technique.

Moreover, $(K_xNa_{1-x})Nb_{0.6}Ta_{0.4}O_3$ samples were sintered as well using the three sintering techniques mentioned above and the highest density was obtained with the SPS technique. Ceramics composition was near the stoichiometric one, and XRD and Raman analysis confirmed that all samples have an orthorhombic structure at room temperature. A diffuse phase transition was observed for composition with x=1.0,0.9,0.8 on TSS and SPS samples, which might be due to compositional dispersion within the grains. Moreover, the dielectric constant and ferroelectric properties were enhanced as the amount of Na increased. Changes on the T_{O-T} and T_C were not observed due to influence of Na but mainly to the Nb/ta ratio, and the dielectric losses were around 2 and 4 % at room temperature.

Bibliography

[1] P.K. Panda, Review: environmental friendly lead-free piezoelectric materials, J. Mater. Sci. 44 (2009) 5049-5062.

[2] J. Rodel, W. Jo, K.T.P. Seifert, E.-M. Anton, T. Granzow, Perspective on the Development of Lead-free Piezoceramics, J. Am. Cerm. Soc. 92 (2009) 1153-1177.

[3] R.-A Eichel, Recent Developments and Future Perspectives of Lead-free Ferroelectrics, Funct. Mater. Lett. 3 (2010) 1-4.

[4] P.K. Panda, B. Sahoo, PZT to Lead Free Piezo Ceramics: A Review, Ferroelectrics 474 (2015) 128-143.

[5] Y. Wang, D. Damjanovic, N. Klein, N. Setter, High-Temperature instability of Li-and Ta-Modfied (K,Na)NbO_3 Piezoceramics, Je. Am. Ceram. Soc. 91 (2008) 1962-1970.

[6] C. Sen, B. Alkan, I. Akin, O. Yucel, F.C. Sahin, G.Goller, Microstructure and ferroelectric properties of spark plasma sintered Li substituted ($K_{0.5}Na_{0.5}$)NbO_3 ceramics, J. Ceram. Soc. Jpn. 119 (2011) 355-361.

[7] S. Triebwasser, Study of Ferroelectric transitions of Solid-Solutions Single Crystals of $KNbO_3$ –$KTaO_3$, Phys. Rev. 114 (1959) 63-70.

[8] D. Rytz, H.J. Scheel, Crystal Growth of $KTa_{1-x}Nb_XO_3$ ($0<X \leq 0.04$) Solid solutions by a slow-cooling method, J. Cryst. Growth 59 (1982) 468-484.

[9] J. Venkatesh, V. Sherman, N. Setter, Synthesis and Dielectric Characterization of Potassium Niobate Tantalate Ceramics, J. Am. Ceram. Soc. 88 (2005) 3397-3404.

[10] P.E. Debely, P. Gunter, H. Arend, Preparation and Electro-optic Properties of Hot-Pressed Potassium Niobate-Tantalate Ceramics, Am. Ceram. Soc. Bull. 58 (1979) 606-609.

[11] C. B. DiAntonio, S.M. Pilgrim, Processing, Characterization, and Dielectric Studies on $K(Ta_{1-x}Nb_x)O_3$ for Use at Cryogenic Temperatures, J. Am. Ceram. Soc. 84 (2001) 2547-52.

[12] P. Hansen, D. Hennings, H. Schreinemacher, Dielectric Properties of Acceptor-Doped (Ba,Ca)(Ti,Zr)O_3 Ceramics, J. Electroceram. 2 (1998) 85-94.

[13] Y. Sun, H. Liu, H. Hao, S. Zhang, Effect of Oxygen vacancy on Electrical Properties of Acceptor Doped $BaTiO_3$-$Na_{0.5}Bi_{0.5}TiO_3$-Nb_2O_5 X8R Systems, J. Am. Ceram.Soc.

(2016) 1-7.
[14] V.B. Braginsky, V.S. Ilchenko, K.S. Bagdassarov, Experimental observation of fundamental microwave absorption in high quality dielectric crystals, Phys. Lett A 120 (1987) 300-305.
[15] V.L. Gurevich, A.K. Tagantsev, Intrinsic dielectric loss in crystals, Adv. Phys. 40 (1991) 719-767.
[16] G. Liu, S. Zhang, W. Jiang, W. Cao, Losses in Ferroelectric Materials, Mat. Sci. Ang. R 89 (2015) 1-48.
[17] S. J. Perm, N. M. ALford, A. Templeton, X. Wang, M. Xu, M. Reece, K. Schrapelt, Effect of Porosity and Grain Size on the Microwave Dielectric Properties of Sintered Alumina, J. Am. Ceram. 80 (1997) 1885-88.
[18] Y. Wang, D. Damajonovic, N. Klein, N. Setter, High-Temperature Instability of Li- and Ta-Modified (K,Na)NbO_3 Piezoceramics, J. Am. Cerami. Soc. 91(2008) 1692-1970.
[19] Y.G. Lv, C.L. Wang, J.L Zhang, L. Wu, M.L Zhao, J.P. Xu, Tantalum influence on physical proprties of $(K_{0.5}Na_{0.5})(Nb_{1-x}Ta_x)O_3$ ceramics, Mater. Res. Bull. 44 (2009) 284-287.
[20] Y.S. Sung, J.H. Lee, S.W Kim, T.H Lee, J.M kim, J.H. Cho, T.K. Song, M.H. Kim, T.G. Park, Enhanced piezoelectric properties of $(Na_{0.53}K_{047})(Nb_{1-x}Ta_x)O_3$ ceramics by Ta substitution, Ceram. Int. 38S (2012) S301-S304.
[21] R.M. German, Liquid Phase Sintering, Plenum Press, New York, 1985.
[22] H. Sun, X. Wang, X. Yao, Effect of WO_3 doping on dielectric and ferroelectric properties of $0.94(Bi_{0.5}Na_{0.5})TiO_3$–0.06 $BaTiO_3$ ceramics, Ceram. Int. 38S (2012) 373-377.
[23] L. Zhang, M.L. Zhang, C.L. Wang, Y.P. Peng, Y.G. Wang, Size dependence of dielectric properties and structural metastability in ferroelectrics, Eur. Phys. J. B 11 (1999) 565-573.
[24] R.E. Stanculescu, C.E. Ciomagaa, N. Horchidana, C. Galassib, F.M. Tufescua, L. Mitoseriua, The influence of post-sintering re-oxidation treatment on dielectric response of dense and porous $Ba_{0.70}Sr_{0.30}TiO_3$ ceramics, Ceram. Int. 42 (2016) 527-536.
[25] V. R Mudinepalli, L. Feng, W.-C Lin, B.S. Murity, Effect of grain size on dielectric and ferroelectric properties of nanostructured $Ba_{0.8}Sr_{0.2}TiO_3$ ceramics, J. adv. Ceram. 4

(2015) 46-43.

[26] M.P. McNeal, S.J. Jang, R.E. Newnham, Particle size dependent high frequency dielectric properties of barium titanate, J. Appl. Phys. 83 (1996) 837-840.

[27] S. Tusseau-Nenez, J.P. Games, M. Maglione, A. Morell, J.C. Niepce, M. Paté, BST ceramics: Effect of attrition milling on dielectric properties, J. Eur. Ceram. Soc. 24 (2004) 3003-3011.

[28] L. Jin, F. Li, S. Zhang, Decoding the Fingerprint of Ferroelectric Loops: Comprehension of the Material Properties and Structures, J. Am. Ceram. Soc. 97 (2014) 1–27.

[29] S.K. Manlief, H.Y. Fan, Raman Spectrum of $KTa_{0.64}Nb_{0.36}O_3$, Phys. Rev B, 5 (1972) 4046-4060.

[30] N.N. Zhang, R.S. Wei, J.Y. Wang, X.B. Hu, H.J. Zhang, CC. Santos, I. Guedes, Phase transition investigation by Raman spectroscopy in highly diluted KTN crystals, J. Alloys Compd. 531 (2012) 14-17.

[31] A. Bartasyte, J. Kreisel, W. Peng, M. Guilloux-Viry, Temperature-dependent Raman scattering of KTa_{1-x} Nb_xO_3 thin films, Appl. Phys. Lett. 96 (2010) 262903.

[32] N. Klein, E. Hollenstein, D. Damjanovic, H.J. Trodahl, N. Setter, M. Kuball, A study of the phase diagram of $(K,Na,Li)NbO_3$ determined by dielectric and piezoelectric measurements, and Raman spectroscopy, J. Appl. Phys. 102 (2007) 014112.

[33] F. Rubio-Marcos, P. Marchet, T. Merle-Méjean, J.F Fernandez, Role of sintering time, crystalline phases and symmetry in the piezoelectric properties of lead-free KNN-modified ceramics. Mater. Chem. Phys. 123 (2010) 91-97.

[34] H. Urši, A. Benan, M. Škarabot, M. Godec, M. Kosec, Dielectric, ferroelectric, piezoelectric, and electrostrictive properties of $K_{0.5}Na_{0.5}NbO_3$ single crystals. J. Appl. Phys. 107 (2010) 033705.

[35] Y.G. Lv, C.L. Wang, J.L Zhang, L.Wu, M.L Zhao, J.P. Xu, Tantalum influence on physical properties of $(K_{0.5}Na_{0.5)}(Nb_{1-}xTa_x)O_3$ ceramics, Mater. Res. Bull. 44 (2009) 284-287.

[36] M. Matsubara K. Kikuta, S. Hirano, Piezoelectric properties of $K_{0.5}Na_{0.5}Nb_{1-x}Ta_xO_3$−$K_{5.4}CuTa_{10}O_{29}$ ceramics, J. Appl. Phys. 97 (2005) 114105.

[37] J. Wu, D. Xiao, J. Zhu, Potassium Sodium Niobate Lead-Free Piezoelectric Materials: Past, Present, and Future of Phase Boundaries, Chem. Rev. 115 (2015) 2559–2595.

[38] H. Tian, C. Hu, X. Meng, P. Tan, Z. Zhou, J. Li, B. Yang, Top-Seeded Solution Growth and Properties of $K_{1-x}Na_xNbO_3$ Crystals, Cryst. Growth Des. 15(2015) 1180–1185.

[39] H. Tian, X. Meng, C. Hu, P. Tang, X. Cao, G. Shi, Z. Zhau, R. Zhang, Origin of giant piezoelectric effect in lead-free $K_{1-x}Na_xTa_{1-y}Nb_yO_3$ single crystals, Sci. Re. 6 (2016) 25637.

[40] J. Wu, Y. Wang,Two-step sintering of new potassium sodium niobate ceramics: a high d_{33} and wide sintering temperatures, Dalton Trans. 43 (2014) 12836-12841.

GENERAL CONCLUSIONS

The purpose of this work was to synthesize and characterize three lead-free ferroelectric materials that might be potentially candidates for further investigation on replacing PZT materials. The first part of this work was dedicated to study the stability under pressure of $SrTi_{1-x}Zr_xO_3$ (STZ) and $KNb_{1-X}Ta_XO_3$ (KNT) polycrystalline samples. The high-pressure studies that we performed were based on DFT calculations (annex), which showed that these compounds have a pressure induce phase transitions at low pressures. Moreover, the second part of this research was focused on improving the sinterability of $K(Nb_{0.40}Ta_{0.60})O_3$ by using different sintering techniques such as sintering aid, two step sintering and spark plasma, and to study the microstructure, dielectric and ferroelectric properties of this compound. We finally investigated the influence of Na on the dielectric properties of $(K_xNa_{1-x})Nb_{0.6}Ta_{0.4}O_3$ ceramics by using the same sintering techniques mentioned above.

The high-pressure analyses that we performed on the polycrystalline sample of $SrTi_{1-x}Zr_xO_3$ and $KNb_{1-X}Ta_XO_3$ were intended to lead us to a better understanding of the different phase transitions that could be induced by pressure. We reported the first high pressure Raman studies on $SrTi_{1-x}Zr_xO_3$ (x= 0.3, 0.4, 0.5, 0.6, 0.7) in this work. Using Raman scattering experiments enabled us to follow the evolution of the Raman modes of these compositions with pressure. Our results showed an increase of the Raman modes in the spectra with pressure, which evidence that at the local level the samples undergo a pressure induce phase transition towards lower symmetries. We also presented that the observed transition pressure for $SrTi_{0.6}Zr_{0.4}O_3$ around 5 GPa by Raman Spectroscopy was in agreement with the high-pressure X-ray diffraction results that we obtained. On the other hand, the high-pressure X-ray diffraction results for $SrTi_{0.7}Zr_{0.3}O_3$ revealed there was no discontinuities in the evolution of the volume as a function of pressure and only the structural changes were observed at the local level by Raman spectroscopy.

Furthermore, we reported the first studies for the rich part of tantalum on $KNb_{1-X}Ta_XO_3$ (x=0.4, 0.5, 0.6, 0.9) powders. We showed by the high pressure Raman spectroscopy experiments a decrease of the Raman modes as the pressure was increased, which is an indication that phase transitions towards higher symmetries at the local level are induced by pressure. We were able to follow the evolution of the main Raman modes

for the orthorhombic and tetragonal phases until the cubic phase was reach, and based on the Raman results we presume that above 3GPa $KNb_{0.1}Ta_{0.9}O_3$ might become amorphous since the sample did not recover the initial spectrum as the pressure was release. Nevertheless, we did not detect any structural changes as we increased the pressure in the XRD experiments that we carried out for $KNb_{0.4}Ta_{0.6}O_3$ and $KNb_{0.6}Ta_{0.4}O_3$.

The high-pressure Raman results that we obtained during this investigation allowed us to propose a pressure-composition phase diagram for $SrTi_{1-x}Zr_xO_3$ and $KNb_{1-x}Ta_xO_3$ compounds.

The study of different sintering methods in order to well densified $K(Nb_{0.4}Ta_{0.6})O_3$ ceramics revealed an improvement of the dielectric constant and dielectric losses by using KF as sintered aid and the TSS method. Furthermore, we showed that the SPS pellet has a fine microstructure with the highest density compared with all the other samples and the best ferroelectric behavior.

Moreover, we obtained dense $(K_xNa_{1-x})Nb_{0.6}Ta_{0.4}O_3$ ceramics by using KF as sintering aid, TSS and SPS techniques. We confirmed by XRD and Raman spectroscopy that all samples have an orthorhombic structure at room temperature. In addition, we observed a diffuse phase transition for some of the TSS and SPS samples, which might be due to composition fluctuation of the pellets. We reported an increase of the dielectric constant for all the ceramics as the amount of Na increased, and the highest value was around 6000 for the TSS ceramics with 50/50 ratio. No changes on the Curie temperature were perceived due to Na or to the sintering methods that we use but an improvement of the ferroelectric properties for the SPS samples was observed with the amount of Na.

PERSPERCTIVES

The study under high pressure for the $SrTi_{1-x}Zr_xO_3$ and $KNb_{1-x}Ta_xO_3$ solid solutions has given important information on the different phase transitions ranges and opens many topics for further research. Therefore, an investigation of these compositions by using large-scale facilities will confirm the phase transitions observed by Raman spectroscopy but also it would clarify the crystal structure of the different phase transitions observed at high pressure that we determined in this investigation.

Concerning the microstructure, dielectric and ferroelectric characterization of $KNb_{0.4}Ta_{0.6}O_3$ and $(K_xNa_{1-x})Nb_{0.6}Ta_{0.4}O_3$ ceramics it would be important to further study the influence of the grain size by different sintering techniques on the final properties of these compounds. It was observed that Na enhanced the dielectric and ferroelectric properties of $(K_xNa_{1-x})Nb_{0.6}Ta_{0.4}O_3$ and it would be interesting, to study the influence of other dopants on the B-site for this composition.

APPENDIX

APPENDIX A. DIELECTRIC STUDIES ON $SrTi_{0.3}Zr_{0.7}O_3$ CERAMICS

At room temperature $SrTi_{0.3}Zr_{0.7}O_3$ has an orthorhombic structure (*Pnma*), which is centrosymmetric and does not present any ferroelectric properties. A pellet of this composition was sintered by a conventional sintering method. After confirming the pure phase the calcinated powders were mixed with an APV (80%)/PEG (20%) binder aqueous solution before they were sieved and pressed again into pellets of 13 mm diameter. The green pellet was placed in an Al_2O_3 crucible and it was sintered in air at 1600 °C for 2 hours. Figure XX shows the temperature dependence of the dielectric properties for this sample. We can observe that the dielectric constant does not change significantly with temperature and values are very low. The dielectric losses were stable (lower than 8%) and at high temperatures (>100°C), they continuously increase with temperature due to the electrical conductivity thermally activated. In addition, it was not observed any face transitions depending on temperature (-80 to 130 °C) and this confirms that the compound does not have any ferroelectric properties for the range of temperatures studied.

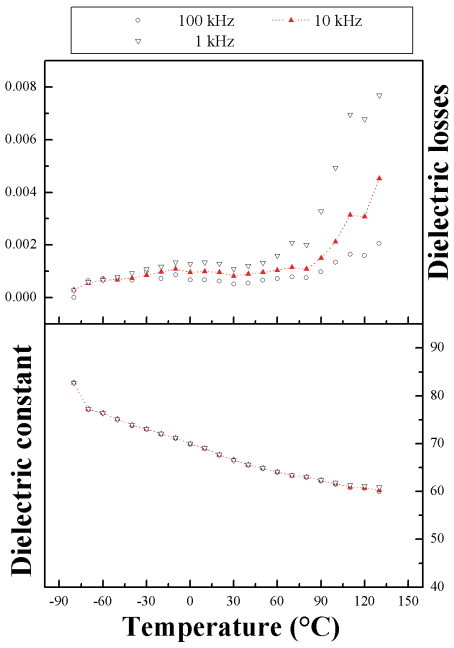

Figure 1. Temperature dependence of the dielectric constant and dielectric losses of $SrTi_{0.3}Zr_{0.7}O_3$ ceramic sintered by a conventional method in air.

APPENDIX B. PRESSURE-DEPENDENT RAMAN SCATTERING OF POLYCRYSTALLINE $KNb_{1-x}Ta_xO_3$ SOLID SOLUTIONS

The theoretical Raman spectra were calculated by using the Density Functional Theory (DFT) (at 0 K). The theoretical data were obtained with the periodic CRYSTAL14 code [1, 2]. The used exchange – correlation functional is the hybrid PBE0 functional [3] which was shown to be the most adequate for the accurate description of the structural, electronic, vibrational and dielectric properties in agreement with experimental data for this family of materials [4]. Regarding the basis sets, an all – electron Gaussian type basis set was used for O; K, Nb and Ta were described with Gaussian type basis sets combined with pseudopotentials. A full description of these basis sets is given in reference [5]. As regards the computational conditions for the evaluation of the Coulomb and exchange series, the adopted thresholds on the overlap as defined in the CRYSTAL manual [31] are 10^{-8}, 10^{-8}, 10^{-8}, 10^{-8} and 10^{-16} a.u.. Calculations were performed with a 8 x 8 x 8 Monkhorst – Pack *k*-point mesh [6]. The Γ-point harmonic frequencies were calculated in the frozen phonons approximation.

The computed spectra were calculated considering ideal powders, with no preferred orientation, and assuming an incident light with a wavelength of 488 nm. They were convoluted with a Gaussian equation.

Theoretical and experimental spectra

The experimental spectra compared with the computed ones at different pressures and at different structures for $KNb_{1-x}Ta_xO_3$ (x=0.6, 0.5, 0.4) are shown in the following figures.

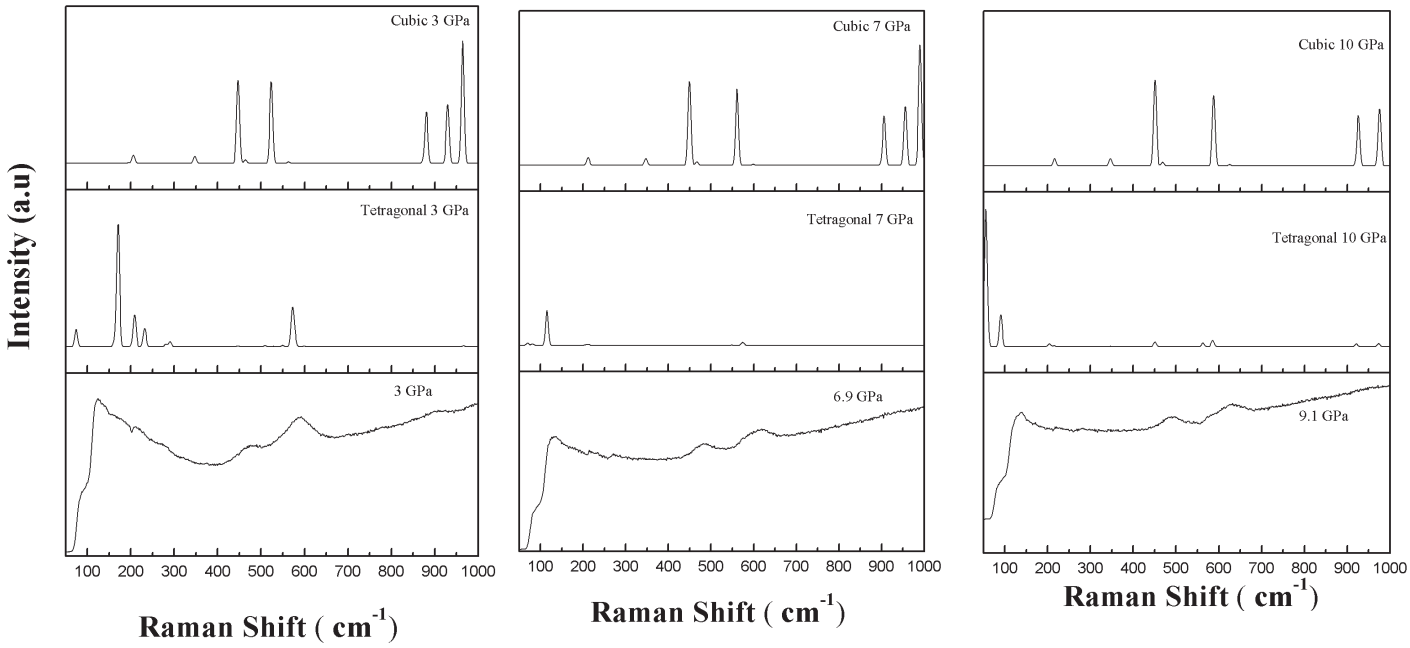

Figure 2. Calculated and experimental Raman spectra for $KNb_{0.4}Ta_{0.6}O_3$.The starting structure at room temperature and at room pressure is tetragonal.

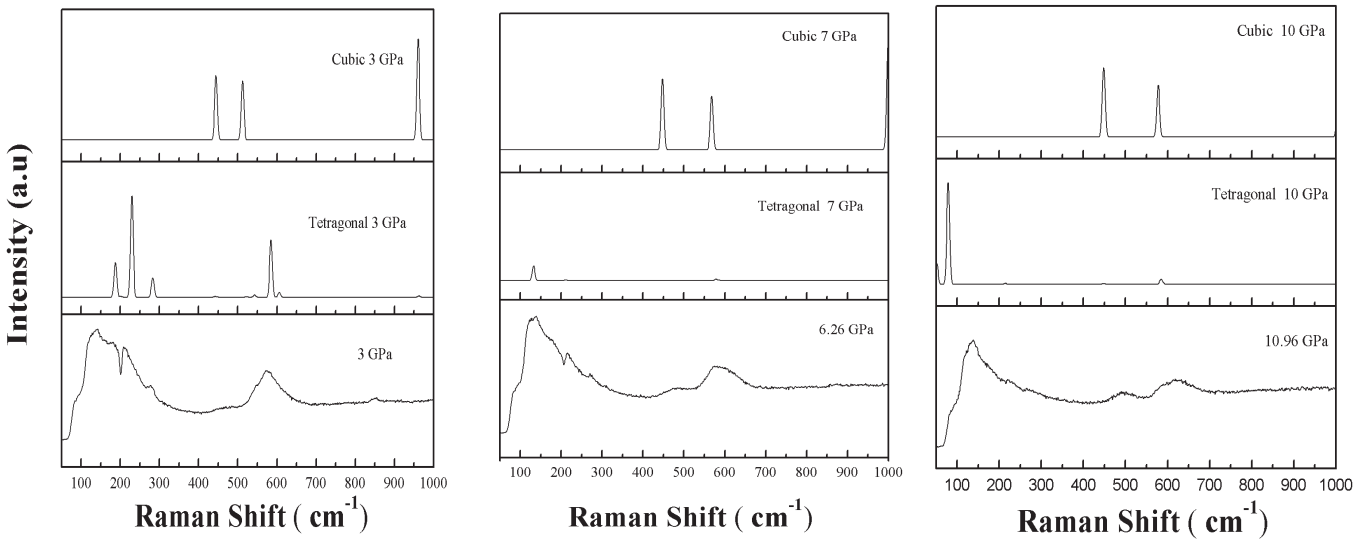

Figure 3. Calculated and experimental Raman spectra for $KNb_{0.5}Ta_{0.5}O_3$. Starting structure is orthorhombic at room temperature and room pressure.

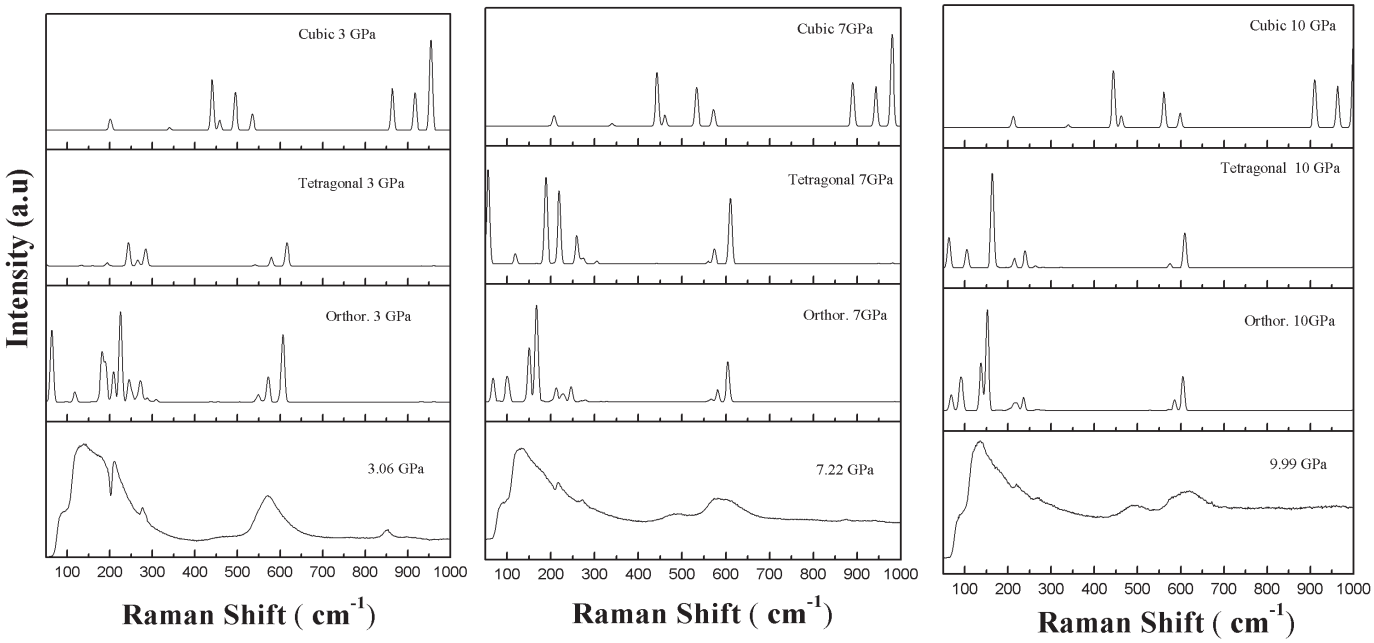

Figure 4. Calculated and experimental Raman spectra for $KNb_{0.6}Ta_{0.4}O_3$. Starting structure is orthorhombic at room temperature and room pressure.

The calculations were performed in a harmonic approximation while the KTN system is highly anharmonic then a discrepancy between the experimental and theoretical calculations will arise. However, it can be observed that there are some common characteristics around the modes at 400 and 600 cm^{-1}. Specifically, when the transition from the tetragonal to the cubic phase takes place and there is a mode that emerges.

Figure 5 shows the experimental and theoretical calculated Raman Spectra for $KNb_{1-x}Ta_xO_3$ (x=0.4. 0.5, 0.6) at the pressures where a phase transition might occur.

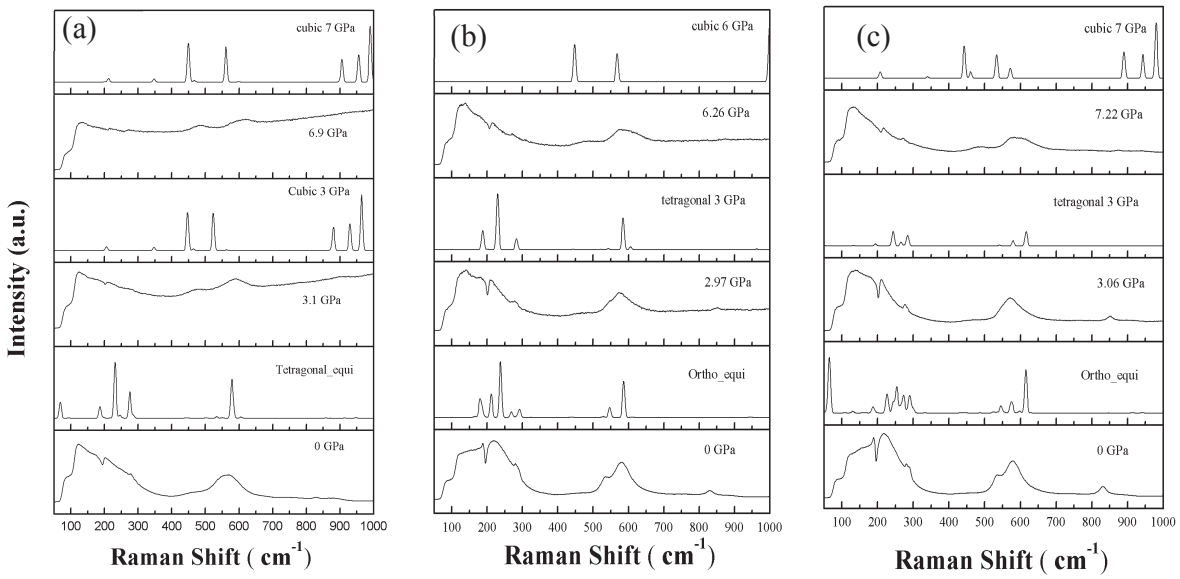

Figure 5. Calculated and experimental Raman spectra for $KNb_{1-x}Ta_xO_3$: a) x=0.4, b) x=0.5 and c) x=0.6. The different experimental Rama Spectra presented in where it is assumed that a phase transition might take please.

Bibliography

[1] R. Dovesi, R. Orlando, A. Erba, C. M. Zicovich-Wilson, B. Civalleri, S. Casassa, L. Maschio, M. Ferrabone, M. De La Pierre, P. D'Arco, Y. Noel, M. Causa, M. Rerat, B. Kirtman, Int. J. Quantum Chem. 114 (2014) 1287.

[2] R. Dovesi, V. R. Saunders, C. Roetti, R. Orlando, C. M. Zicovich-Wilson, F. Pascale, B. Civalleri, K. Doll, N. M. Harrison, I. J. Bush, P. D'Arco, M. Llunell, M. Causà and Y. Noël, CRYSTAL14 User's Manual (University of Torino, Torino, 2014).

[3] C. Adamo, V. Barone, J. Chem. Phys. 110 (1999) 6158.

[4] G. Sophia, Ph. Baranek, C. Sarrazin, M. Rérat, R. Dovesi, Phase Transitions 86 (2013) 1068.

[5] Web site: http://www.crystal.unito.it/basis-sets.php

[6] H. Monkhorst, J. Park, Phys. Rev. B. 13 (1976) 5188.